Envelope inflation in massive stars near the Eddington limit

Dissertation
zur
Erlangung des Doktorgrades (Dr. rer. nat.)
der
Mathematisch-Naturwissenschaftlichen Fakultät
der
Rheinischen Friedrich-Wilhelms-Universität Bonn

von
Debashis Sanyal
aus
Kalkutta, Indien

Bonn, August 2016

Dieser Forschungsbericht wurde als Dissertation von der Mathematisch-Naturwissenschaftlichen Fakultät der Universität Bonn angenommen und ist auf dem Hochschulschriftenserver der ULB Bonn `http://hss.ulb.uni-bonn.de/diss_online` elektronisch publiziert.

1. Gutachter:	Prof. Dr. Norbert Langer
2. Gutachter:	Prof. Dr. Thomas Tauris
Tag der Promotion:	28.11.2016
Erscheinungsjahr:	2016

Abstract

Massive stars, i.e. those stars with masses more than about 10 times that of the Sun, are important agents for the chemical and dynamical evolution of galaxies. Because of the steep mass-luminosity relation, massive stars are extremely luminous objects. Therefore, increasingly massive stars approach their so-called *Eddington luminosity*, i.e., the maximum luminosity they can radiate at. It is usually believed that when the Eddington limit is reached, strong outflows are initiated.

We present state-of-the-art stellar evolutionary models of massive stars and the detailed analyses of their interior structures. After investigating model grids with five different initial chemical compositions, we find that stars reach the Eddington limit in their envelope already at masses of $\sim$ 30 Solar masses and above. Furthermore, instead of showing any violent behaviour upon reaching the Eddington limit, the models develop inflated envelopes, which are extended low-density regions beneath the surface. This phenomenon is mediated by the opacity and convective energy transport in the models.

Luminous Blue Variables (LBVs) like S Doradus which show strong variability on a timescale of decades have been previously suggested to be connected to the Eddington limit, although little was known about their evolutionary stage or interior structure. We find that the hot edge of the S Doradus variability strip coincides with a line beyond which our models show strong envelope inflation, indicating a possible connection between the two. Furthermore, the inflated envelope mass in our coolest models reaches several Solar masses. They provide the first physical model which could explain the large mass ejected by LBVs during the so-called Giant Eruptions, like the one observed for η Carinae in the 19th century.

To further explore the observational consequences of envelope inflation, we follow the evolution of massive hydrogen-free models through the post main-sequence phase and predict that when these inflated stars explode as supernovae, it will lead to extended rise times of the shock breakout signal. Our model closely matches the properties of SN 2008D, the only observation of a shock breakout from a supernova so far.

We conclude that envelope inflation affects the evolution of massive stars from the zero-age main-sequence up to the point of explosion, and may invoke observational instabilities in the envelope that might manifest themselves as pulsations and atmospheric macroturbulence.

Contents

CHAPTER 1

Introduction

> "The Universe is not only queerer than we suppose,
> but queerer than we can suppose."
> - J. B. S. Haldane, in *Possible Worlds and Other Papers (1927).*

Man's fascination with stars began many centuries ago. From ancient times, people across multiple cultures, from the Aztecs in America to the Hindus in modern day India, have worshipped the Sun, the nearest star and the source of life on earth. Apart from having deep-rooted cultural significance, astronomy is also one of the oldest scientific disciplines. Sailors, for example the Polynesians, used the motion of the stars to navigate the mighty seas. Rare astronomical phenomena were also documented, for example an unusual brightening event in the night sky was recorded by Chinese astronomers as early as 1054, which we today know as the supernova SN 1054. The remnants of this explosion formed the spectacular Crab nebula, which is located in the constellation of Taurus and can be observed with the help of a binocular on a clear day. However, it was not until the advent of the telescope in the 17th century that astronomy became a modern scientific discipline. Although a rich catalogue of stars was already available in the 19th century, the questions of how and why stars evolve, remained a mystery.

Unfortunately, the journey of a single star from its birth until its death can not be observed in isolation, as they hardly change appreciably over a human lifetime of $\sim 70-90$ years. Therefore, astronomers observe several stars at various stages of their lives. These observations are then compared with numerical models of stars with an aim to understand the physical phenomena associated with their evolution. In the early 20th century, Ejnar Hertzsprung and Henry Norris Russell invented a powerful way to represent the stellar life cycle, that is known today as the *Hertzsprung-Russell diagram* (H-R diagram), where stars of different evolutionary stages occupy distinct regions. The H-R diagram shows the relationship between the brightness of observed stars which is a measure of the stellar luminosity, and their spectral classifications which is a measure of the surface temperatures of stars. A representative H-R diagram of the Solar neighbourhood showing stars in different stages of their evolution is illustrated in Fig. 1.1. The ordinary hydrogen-burning stars like the Sun are found in a band running from top-left to bottom-right, called the main-sequence. The majority of the stars are located along the main-sequence. Giant stars, that are bigger in size compared to the main-sequence ones, form

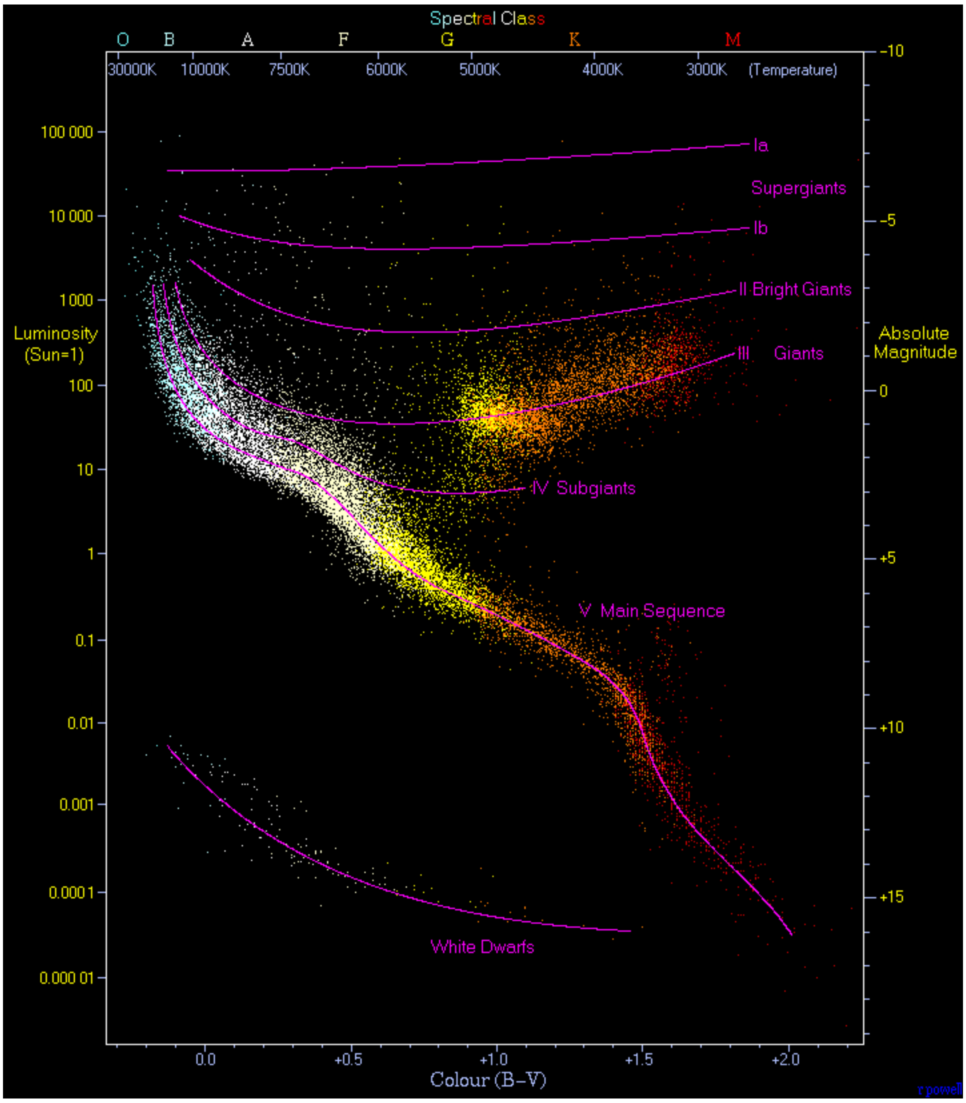

Figure 1.1: A Hertzsprung-Russell diagram showing 22 000 stars in the Solar neighbourhood from the Hipparcos Catalogue along with 1000 low-luminosity stars from the Gliese Catalogue of Nearby Stars. The luminosity is shown in units of the Solar luminosity. The stars are coloured according to their surface temperatures, shown at the top X-axis. *Figure credit:* `https://commons.wikimedia.org/wiki/File:HRDiagram.png`

their own clump on the upper-right side of the diagram. Above them lie the bright giants and supergiants which are much rarer. Near the lower-left corner is the band of white dwarfs – these are the dead cores of old stars which are very faint, and over billions of years slowly cool down towards the bottom-right of the diagram.

The theory of modern stellar evolution and nucleosynthesis is relatively new. Until the late 19th century it was believed that the energy released from gravitational contraction makes the Sun shine, an idea proposed independently by Lord Kelvin and Hermann von Helmholtz. It was only in the 1920's that the pioneering work of A. S. Eddington (and later Hans Bethe) showed that the brightness of the Sun is actually powered by thermonuclear reactions in its core. Gradually astronomers realised that the elements heavier than helium, be it the calcium in our bones, or the iron in our blood, or the fluorine in our toothpaste, were all produced by some star at some point in the cosmic evolution. Furthermore, most of these elements were produced by massive stars, which are stars heavier than roughly ten times the mass of the Sun. Recent progress, mainly from observational campaigns, have shown that there are gaping holes in our understanding of how stars evolve, especially those that are considerably more massive than the Sun. The internal structure and evolution of stars more massive than about 50 Solar masses is particularly not well-understood because the physics in those regimes is uncertain and furthermore, there are few observational constraints. A comprehensive investigation of the structure and evolution of very massive, luminous stars with the help of state-of-the-art numerical models is the focus of this thesis.

Evolution of single stars

Stars are self-gravitating balls of hot plasma that are burning hydrogen in their cores for most ($\sim 90\%$) of their lifetime, also called the main-sequence phase. The time required by a star to burn its nuclear fuel at a given luminosity is called the *nuclear timescale*. The nuclear timescale for burning hydrogen is a good estimate of the lifetime of a star, and it ranges from $\sim 10^6$ years to $> 10^{10}$ years depending upon the mass of the star – higher the mass, shorter is its lifetime. The life cycle of a star is an eternal battle between gravity, directed inwards, and internal pressure gradient, directed outwards. These opposing forces balance each other, a condition known as hydrostatic equilibrium. The timescale over which a star readjusts itself when its hydrostatic equilibrium is disturbed is called the *dynamical timescale*. This readjustment of the star manifests itself as observable transient phenomena, for example during the collapse of a star leading to a supernova, or during pulsations. The third relevant timescale for stellar evolution is the *thermal timescale* or the Kelvin-Helmholtz timescale, which is the time it takes for a star to radiate away its gravitational binding energy at a given luminosity. The Kelvin-Helmholtz timescale is usually a few orders of magnitude shorter than the nuclear timescale but much longer compared to the dynamical timescale. For example, the nuclear timescale of the Sun is $\sim 10^{10}$ years whereas its thermal and dynamical timescales are $\sim 10^7$ years and ~ 30 minutes respectively. Most stars, over most of their lifetime, remain in hydrostatic and thermal equilibrium while changes in their structure and chemical composition occur on their nuclear timescale.

The primary quantity determining the evolution of a star is its mass. If the initial mass is known, one might predict the structure of a star in its different evolutionary stages, and even its final fate (Heger et al. 2003; Langer 2012). Stars with initial masses lower than about $0.8\,M_\odot$, even if they formed very early in the Universe, are still burning hydrogen in their cores because their nuclear timescale is longer than the age of the Universe. After a star runs out of hydrogen fuel in its core, further evolution in the so-called *post main-sequence* phase proceeds differently depending on the mass (Kippenhahn et al. 1990). Stars with initial masses between $\sim 0.8 - 9\,M_\odot$ ignite helium (and also carbon near the higher mass end, but in a degenerate manner) in their cores in the post main-sequence phase, and ultimately develop degenerate cores to leave behind white dwarfs as remnants.

In this thesis, we will concentrate on the structure and evolution of massive stars, i.e., those which ignite carbon in a non-degenerate manner after core helium exhaustion. For stars of Solar chemical composition, the minimum initial mass of massive stars correspond to $\sim 9\,\mathrm{M}_{\odot}$ (Poelarends et al. 2008). In the course of their evolution, massive stars appear as blue/red supergiants, Luminous Blue Variables (Sec. 1.2.2) and Wolf-Rayet stars (Sec. 1.2.3), depending on their mass and mass-loss rates (Sec. 1.1.1). Stars with initial masses in a narrow range around $9\,\mathrm{M}_{\odot}$ collapse before core neon ignition, ultimately leading to an electron-capture supernova (Nomoto 1984; Poelarends et al. 2008). Stars in the mass range $\sim 10 - 100\,\mathrm{M}_{\odot}$ ignite heavier elements, i.e., neon, oxygen and silicon, in a hydrostatic manner until an iron core is formed. Since iron has the highest binding energy per nucleon among all the elements, further burning does not release energy, instead it requires an energy input. Therefore nuclear burning in the core stops at this stage. Just before the iron core collapses dynamically, the chemical structure of the star resembles that of an onion. At the centre is the iron core, surrounded by concentric shells composed of silicon, neon, oxygen, carbon, helium and hydrogen, respectively. The iron core collapse is accompanied with a spectacular, luminous explosion called a supernova if the initial stellar mass is roughly between $10 - 40\,\mathrm{M}_{\odot}$ (Heger et al. 2003; Ugliano et al. 2012). At the end of the core-collapse a compact object, either a neutron star or a black hole is left behind as a remnant.

Very massive stars roughly between $100 - 250\,\mathrm{M}_{\odot}$ undergo dynamical instability in their oxygen cores caused by the production of electron-positron pairs from highly energetic photons. In other words, a substantial fraction of the photon energy is spent in creating pairs instead of raising the core temperature. Because of this, the adiabatic index (γ) of the gas ($P \propto \rho^{\gamma}$; where P is the pressure and ρ is the density) drops below the dynamical stability limit of $4/3$ and the core starts to collapse, resulting in explosive burning of oxygen. For stars in the range $140 - 250\,\mathrm{M}_{\odot}$, the nuclear energy generated in this process is high enough such that it unbinds the whole star without leaving a remnant, and the thermonuclear explosion is termed a pair-instability supernova (PISN; Rakavy et al. 1967; El Eid & Langer 1986; Heger & Woosley 2002). However, if the nuclear energy generated is less than the stellar binding energy (stars in the mass range $\sim 100 - 140\,\mathrm{M}_{\odot}$) for relatively lighter oxygen cores, only a fraction of the envelope might be ejected, which is called pulsational pair-instability (Woosley et al. 2007). Stars with even higher initial masses ($\gtrsim 250\,\mathrm{M}_{\odot}$) are believed to collapse directly to a black hole after the pair-instability phase, according to state-of-the-art single star models (Heger et al. 2003).

How massive can a star be is an open question. Initially it was believed that very massive stars might only form in either metal-free or in very low-metallicity environments (Abel et al. 2002). Although a present-day upper mass limit of $\sim 150\,\mathrm{M}_{\odot}$ has been suggested (Figer 2005) for stars in the local universe based on observations in the Arches cluster, recent studies have challenged this result (Schnurr et al. 2008, 2009; Bestenlehner et al. 2014; Schneider et al. 2014). In the well-studied R136 star cluster (see Fig. 1.2) at the centre of the Tarantula Nebula in the Large Magellanic Cloud, the existence of a very massive star ($\sim 260\,\mathrm{M}_{\odot}$) has been claimed by Crowther et al. (2010). Furthermore, the discovery of SN 2007bi (Gal-Yam et al. 2009) as a strong PISN candidate also provides evidence for the existence of very massive stars in the local universe (Langer et al. 2007). These observations, coupled with recent transient searches discovering new signatures of massive stars have triggered a renewed interest in their evolution.

Figure 1.2: A composite image in ultraviolet, visible, and red light taken by Hubble Space Telescope's Wide Field Camera 3, of the R136 star cluster near the center of the Tarantula Nebula in the Large Magellanic Cloud. This cluster hosts some of the most massive stars discovered in the Local Group.

1.1 Massive stars

Massive stars are relatively rare; this is partly because they are short-lived ($10^6 - 10^7$ years), and partly because the initial mass function (IMF), i.e., the distribution of initial masses for a stellar population in a given volume, predicts that the number of stars that are born within a given mass range decrease rapidly with increasing mass. For example, for every ~ 800 stars born with masses between $1\,M_\odot$ and $2\,M_\odot$, only one star is born with a mass between $10 - 11\,M_\odot$ within the same volume of space, according to the IMF proposed by Kroupa (2001).

Although rare, massive stars are important for various areas of astrophysics. Since massive stars stay hot and luminous for most of their lifetime, they are dominant ionising sources for the interstellar medium (ISM). In fact, the first massive stars are believed to have played a pivotal role in the reionization of the Universe (Bromm & Larson 2004). They are also sometimes referred to as the *cosmic engines* as they are rich sites of nucleosynthesis, enriching the ISM with nuclearly processed material, either via strong stellar winds or by exploding as supernovae. Every massive star that blows up in a supernova injects $\sim 10^{51}$ erg of kinetic energy and $1 - 100\,M_\odot$ of ejecta into the surrounding medium, and this stellar feedback is important for driving both the chemical and dynamical evolution of galaxies. They are also responsible for some of the most energetic events in the night-sky which are not completely understood, like superluminous supernovae and long-duration gamma-ray bursts (GRBs). Furthermore, mergers of the compact remnants of massive stars produce gravitational waves, and therefore studying their evolution is essential for gravitational wave astronomy. Indeed, the first detection of a gravitational wave signal, GW150914, which was made recently by the Laser Interferometer

Gravitational-Wave Observatory (LIGO), was produced by the merger of two stellar-mass black holes (Abbott et al. 2016).

In spite of their importance, modelling the evolution of massive stars is quite challenging and suffers from various uncertainties. There are several physical processes that one must take into account in the theoretical models to facilitate meaningful comparisons with observations. Some of these are mass-loss, rotation, internal mixing processes, magnetic fields and the effect of a binary companion. As it turns out, the treatment of mass-loss and energy transport critically alter the evolution of massive stars right from the beginning, i.e., even in the main-sequence phase (Langer 2012). Therefore, massive main-sequence stars offer ideal laboratories to test stellar models. Efforts in this direction has already been made, for example, the recently concluded VLT-FLAMES Tarantula Survey (VFTS, Evans et al. 2011) has obtained multi-epoch spectra of about 1000 massive stars in the 30 Doradus region of the Large Magellanic Cloud and has derived stellar parameters for many of them. We briefly discuss below the role of mass-loss, metallicity, opacity and energy transport in the context of massive star evolution.

1.1.1 Mass loss

The evolution of a massive single star is greatly shaped by the mass loss it experiences throughout its lifetime (Chiosi & Maeder 1986; Smith 2014), either by strong stellar winds or by eruptive outbursts. Mass-loss has a deterministic influence on the life of a massive star as it affects the luminosity, lifetime, temperature and angular momentum content of the star. It might also influence the final fates of massive stars as supernovae, GRBs or pair-instability supernovae, and the formation of either a neutron star or a black hole.

Higher the mass of a star, stronger is the effect of mass-loss. While the mass-loss rate of the Sun is only $\sim 10^{-14}\,\mathrm{M_\odot\,yr^{-1}}$, for a $50\,\mathrm{M_\odot}$ Solar metallicity star, it is $\sim 10^{-6}\,\mathrm{M_\odot\,yr^{-1}}$. Therefore, for example, a $100\,\mathrm{M_\odot}$ zero-age main-sequence star (ZAMS) with Solar metallicity could end its life as a $\sim 10\,\mathrm{M_\odot}$ star, losing 90% of its initial mass during its lifetime (Woosley et al. 2002). Massive stars primarily lose mass via winds that are driven by radiation pressure acting on metal lines. Momentum is transferred from the radiation field to the metal ion by line absorption, which then transfers momentum to its neighbouring ions, thereby driving an outflow in the form of a wind. Therefore, how strong the stellar wind is depends on the metallicity (cf. Sec. 1.1.2) of the star – primarily its iron content. Stellar winds become more powerful as the luminosity of a star increases, and a theoretical prescription for computing mass-loss rates (by line-driving) of hot, massive stars as a function of the stellar parameters has been developed by Vink et al. (2000, 2001). This prescription is commonly used in stellar evolution codes (Brott et al. 2011; Ekström et al. 2012) and has been confirmed by observations (Mokiem et al. 2007). For hydrogen-deficient Wolf-Rayet stars (Sec. 1.2.3), stellar evolution models rely on empirical mass loss-rates prescribed by various authors, for e.g., Hamann et al. (1995) and Nugis & Lamers (2000).

Some massive stars also shed mass in short mass-loss episodes, like some Luminous Blue Variables (Sec. 1.2.2) for which mass-loss rates of up to $\sim 1\,\mathrm{M_\odot\,yr^{-1}}$ has been inferred. The physical origin of these events is one of the biggest unsolved problems in stellar evolution as line-driven wind theory can not account for such high mass-loss rates. Furthermore, from observations of a certain type of supernova known as Type IIn supernova (Schlegel 1990), it has been inferred that their progenitors suffer from brief outbursts a few years to decades before core-collapse (Smith 2015). While the exact mechanism that causes such mass-loss is still unknown, some possibilities have been suggested, including wave-driven mass-loss (Quataert & Shiode 2012) and pulsational pair instability (Woosley et al. 2007). Furthermore, pulsations can enhance the mass-loss rate of a star, for example in the classical Cepheid variables.

Mass-loss in massive stars not only manifests itself in the form of stellar winds and outbursts, but also in the form of mass transfer via Roche-lobe overflow in close binary systems. The amount of mass ‘lost’, or transferred in this process might be significantly higher than that via stellar winds.

1.1.2 Metallicity

In astronomy, all elements heavier than helium are referred to as *metals*, and the fraction of metals present in a star determines its metallicity (Z). If the collapsing gas cloud contains less metals, it is easier to form stars with higher masses (Zinnecker & Yorke 2007) as fragmentation is reduced. Furthermore, the metallicity of a star can have a dominant influence on the evolution and the final fate of a star (Heger et al. 2003). Firstly, as already hinted in Sec. 1.1.1, stellar wind mass loss scales as Z^{α} ($\alpha \approx 0.7$), implying that low-Z stars have weaker winds, and hence, lower angular momentum loss, compared to their high-Z counterparts. As a result, a star of a given initial mass will have a higher mass and angular momentum at the time of explosion, if it was born in a lower metallicity environment.

Secondly, the CNO-cycle via which hydrogen burns to helium in the stellar core, is less efficient if the abundance of CNO, or the metallicity, is lower. Therefore the core needs to contract and reach higher temperatures to attain thermal equilibrium. This leads to a lower metallicity star being hotter, compact, and more luminous at the ZAMS, compared to a higher metallicity star of the same mass.

1.1.3 Opacity

The opacity of stellar matter is crucial in determining the mode of energy transport (Sec. 1.1.4) and consequently the structure of a star. For massive hot stars the opacity in the inner layers is dominated by Compton scattering, i.e., the inelastic scattering of high energy photons by a free electrons. However, in the 1990’s the OPAL opacity project (Iglesias et al. 1992; Iglesias & Rogers 1996) at the Lawrence Livermore National Laboratory discovered an opacity bump, popularly known as the *iron opacity bump* at a temperature around 180 000 K. This arose from improved atomic physics computations that discovered bound-bound transitions of iron-group elements. The value at the peak of this opacity bump is typically around $1\,\mathrm{cm}^2\,\mathrm{g}^{-1}$, i.e., approximately three times the electron scattering opacity value. This discovery drastically changed the structure of the outer layers of massive star models (Stothers & Chin 1993, cf. Sec. 1.2.1). Stability studies of massive hot stars, for example, were greatly affected by this discovery (Kiriakidis et al. 1992, 1993) and led to the prediction of new instability domains (Pamyatnykh 1999). As we will elaborate in Chaps. 2 and 3, some of the key results of this thesis rely on the existence of the iron opacity peak.

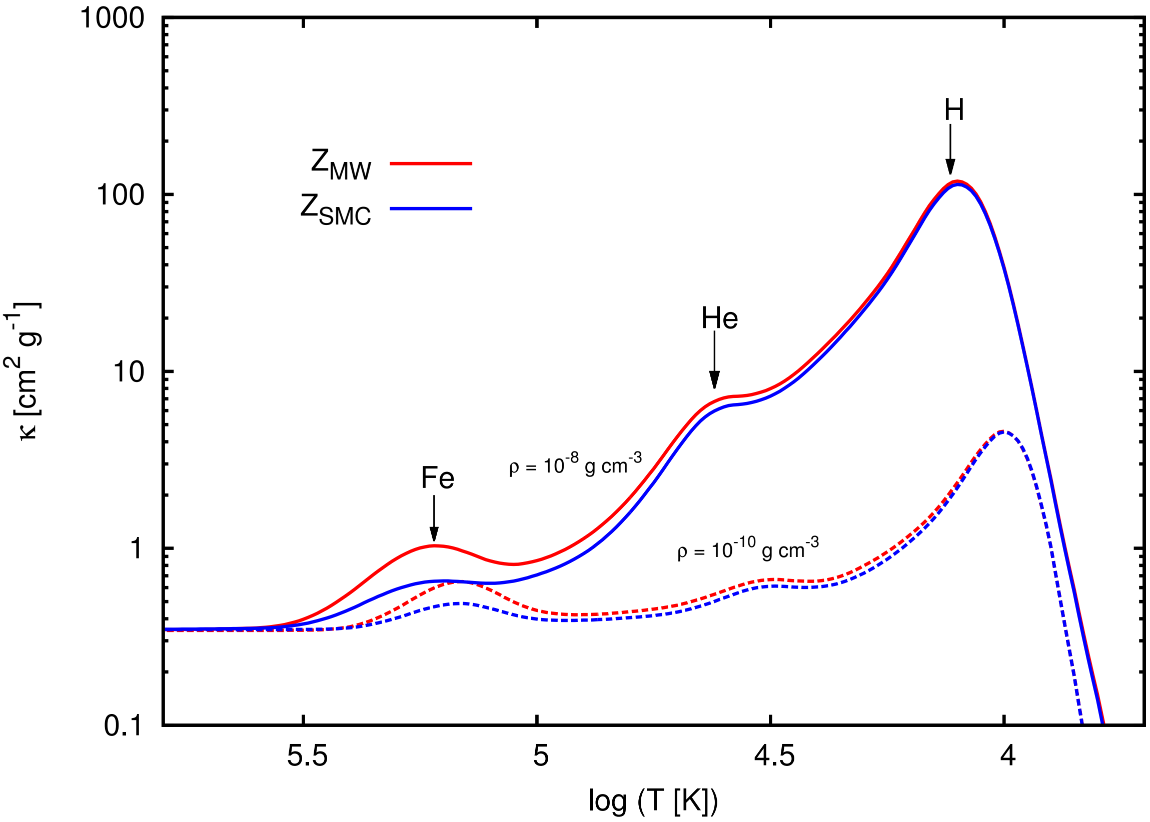

Figure 1.3: Interpolated opacities from the OPAL tables (Iglesias & Rogers 1996) for $T > 8000\,\mathrm{K}$ and low temperature opacities from Alexander & Ferguson (1994) for $T > 8000\,\mathrm{K}$. The solid lines correspond to a density of $10^{-8}\,\mathrm{cm}^2\,\mathrm{g}^{-1}$ whereas the dashed lines correspond to a density of $10^{-10}\,\mathrm{cm}^2\,\mathrm{g}^{-1}$. The red and the green lines refer to the chemical composition of the Milky Way and the Small Magellanic Cloud respectively. The three opacity peaks caused by iron, helium and hydrogen ionisation are indicated.

The radiative opacities of stellar matter for two different values of densities typically encountered in the outer layers of massive stars are shown in Fig. 1.3. The three different opacity peaks around the partial ionisation zones of iron, helium and hydrogen are visible at their characteristic temperatures. The overall trend is that opacity decreases with a decrease in density and metallicity, but increases with a decrease in temperature.

1.1.4 Energy transport

The energy generated inside a star via nuclear fusion must be transported through the stellar interior up to the surface to stay in thermal equilibrium. Inside stars, energy is transported primarily via two modes: radiation and convection. Radiative transport is usually treated simply as a diffusive process as the mean free path of photons is many orders of magnitude shorter than the size of the star. The major uncertainty lies with modelling convective energy transport. Convection is a mode of heat transfer that involves the bulk motion of the fluid, for example, in a pot of boiling water on a stove. It is inherently a 3-D phenomenon, and should ideally be modelled with 3-D hydrodynamical simulations. But, unfortunately the current computing capabilities of even the most powerful supercomputers are not enough to simulate these processes over a star's lifetime because of the wide range of length scales and time scales involved. The nuclear time scale, over which a star evolves, is much longer ($\sim 6 - 16$ orders of magnitude) compared to the dynamical time scale over which the hydrodynamic instabilities are believed to be at work.

Convection and Mixing Length Theory

Convective instability sets in when the temperature gradient in a stellar layer becomes so high such that radiation can not transport the flux any more. In stars, convection is triggered either in regions with a large energy flux, like in the core of massive stars, or, in regions where the opacity is high, typically in the cooler layers of the star. Therefore, in the outer layers, the iron bump opacity as well as the opacity bumps in the partial ionisation zones of helium and hydrogen, makes those layers convectively unstable (cf. Chap. 2), giving rise to sub-surface convection zones (Cantiello et al. 2009). The presence of the sub-surface convection zones in massive stars have been predicted to induce observable phenomena at the surface, such as *microturbulence* (Cantiello et al. 2009) and *macroturbulence* (Grassitelli et al. 2015b), and might also trigger wind clumping (Sundqvist & Owocki 2013).

A simplified model of convective energy transport is considered in most 1-D stellar evolution codes which is known as the Mixing Length Theory (MLT), first proposed by Prandtl in 1926 and later developed by Böhm-Vitense (1958). In this picture, buoyant blobs of gas are assumed to move up a certain distance called the mixing length, before losing their identity and depositing their energy to the surrounding medium. The radiative losses encountered by the blobs along this path is a measure of the efficiency of convection. In the deep interior of a star convection is very efficient, meaning that it transports bulk of the energy, and the resulting temperature stratification is very close to the adiabatic one. However, in the outer layers the densities are several orders of magnitude lower, and the thermal time scale might be comparable to the dynamical time scale. In such situations that are typical of the outer envelopes of massive stars, convection becomes inefficient because of high radiative losses encountered by the blobs along their path. The mixing length is often assumed to be proportional to the pressure scale height and the proportionality constant α_{MLT} is the only free parameter in the model. The value of α_{MLT} is usually set by calibrating it to the observed properties of the Sun. However, α_{MLT} is particularly unconstrained for massive stars, and even the validity of MLT has been questioned in certain regimes (Arnett et al. 2015; Jiang et al. 2015). In spite of its many simplifying assumptions, MLT has been remarkably successful in modelling stellar interiors and explaining different kinds of stellar populations.

Having introduced massive stars and the relevant physical processes, in the next section we will take a closer look at the physics of very luminous stars when they are near the so-called *Eddington limit*.

1.2 The Eddington limit

The Eddington limit is usually referred to as the condition when the radiative acceleration (g_{rad}) directed outwards from the star equals the gravitational acceleration (g) acting inwards. The Eddington factor (Γ) is simply defined as the ratio of these two accelerations, i.e.,

$$\Gamma := \frac{g_{\mathrm{rad}}}{g} = \frac{\kappa L}{4\pi c G M}, \tag{1.1}$$

where κ is the opacity coefficient, M and L are the stellar mass and luminosity respectively, and the constants have their usual meaning. The Eddington limit is then the condition $\Gamma = 1$, and the luminosity for which this equality is satisfied is called the Eddington luminosity L_{Edd} . When electron scattering is considered to be the only opacity source, i.e. $\kappa = \kappa_{\mathrm{e}}$, it is known as the classical Eddington limit ($\Gamma_{\mathrm{e}} = 1$). Arthur Stanley Eddington noted in his book (Eddington 1926) that stars must have a luminosity lower than their Eddington luminosity, otherwise the radiation emitted will blow up the star. Indeed, when a star blows up in a supernova, the radiation observed is many orders of magnitude greater than its Eddington luminosity. One might therefore ask the question whether (and how) the Eddington limit is reached for normal main-sequence massive stars.

If the equation of state of stellar matter is dominated by ideal gas, then one can show that the luminosity scales as $L \sim M^3$. If this holds true for all M, then $\Gamma_{\mathrm{e}} = 1$ is reached at a mass of roughly 200 $\mathrm{M}_{\odot}$, and this defines an upper mass limit for stars. But, for massive stars, the role of radiation pressure in the equation of state becomes increasingly important. Therefore, in general, the mass-luminosity relation is given as $L \sim M^{\alpha}$ where $\alpha > 1$. This scaling relation becomes flatter for massive stars because $\alpha \to 1$ as $M \to \infty$ (Kippenhahn et al. 1990). For the Sun, it is $\Gamma_{\mathrm{e}} \approx 10^{-5}$, i.e., far away from the classical Eddington limit. In a 10 $\mathrm{M}_{\odot}$ ZAMS star of Solar composition, Γ_{e} increases by three orders of magnitude to 0.01. But for a 100 $\mathrm{M}_{\odot}$ star, $\Gamma \simeq 0.3$, which is still fairly away from the Eddington limit. Detailed numerical models show that the classical Eddington limit is indeed reached by stars, but only at extremely high masses, $M \gtrsim 10^5\,\mathrm{M}_{\odot}$ (Kato 1985, 1986).

In the $\log L - \log M$ plane, the Eddington luminosity L_{Edd} for fixed values of κ correspond to straight lines with the same slope, but with different intercepts. This has been illustrated in Fig. 1.4. The ZAMS models for LMC do not encounter the electron-scattering Eddington limit in the mass range considered here ($1 - 500\,\mathrm{M}_{\odot}$). The slope of the ZAMS however tends to unity at the highest masses, as discussed above.

One might also compute the Eddington factor locally in the interior of the stellar model (Langer 1997). In that case when the Rosseland mean opacities are used, the Eddington luminosity is expressed as,

$$L_{\mathrm{Edd}} = \frac{4\pi c G M(r)}{\kappa(r)}, \tag{1.2}$$

where r and $M(r)$ are the radial and the mass co-ordinates respectively and $\kappa(r)$ is the local Rosseland mean opacity. When the Eddington luminosity is computed considering a typical iron bump opacity coefficient of $1\,\mathrm{cm}^2\,\mathrm{g}^{-1}$ (cf. Sec. 1.1.3), the ZAMS models reach the Eddington limit at $\sim 100\,\mathrm{M}_{\odot}$. Since the TAMS models are more luminous than their ZAMS counterparts,

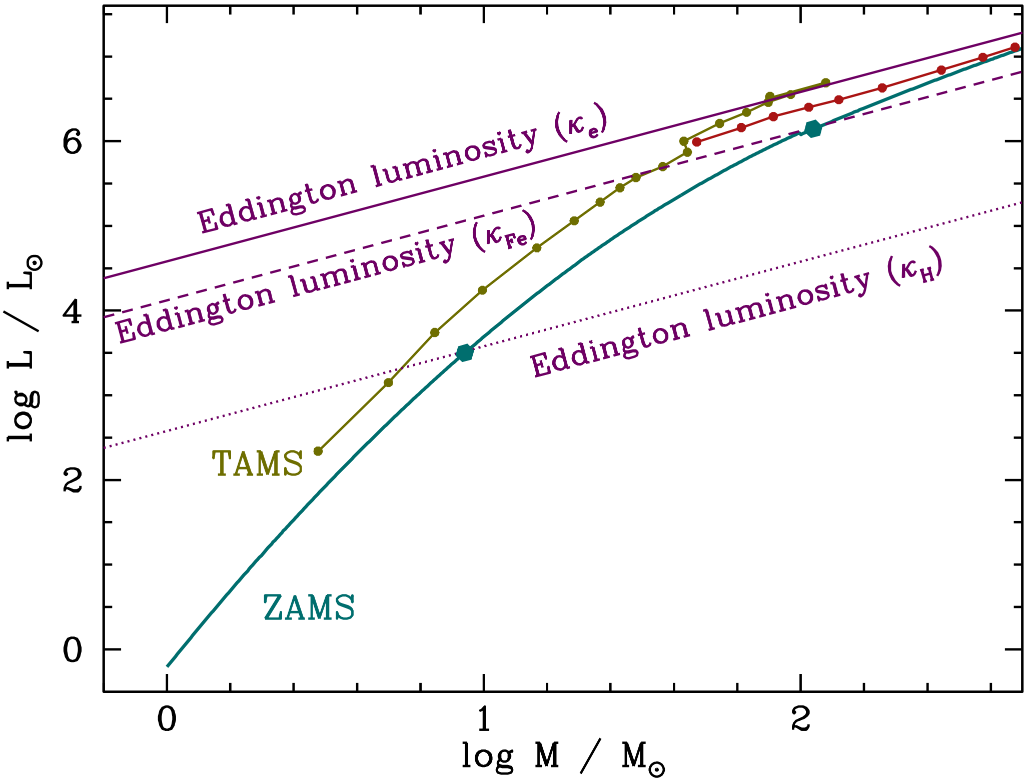

Figure 1.4: Mass-luminosity plot showing the zero-age main-sequence (ZAMS, blue line) and the terminal-age main-sequence models (TAMS, brown line) computed with LMC metallicity (Brott et al. 2011; Köhler et al. 2015). The red line corresponds to those models that are enriched in helium at the surface. The models were rotating with an initial equatorial rotational velocity of $\sim 100\,\mathrm{km\,s^{-1}}$ at their surface. The three straight lines denote the Eddington luminosities considering three different opacity sources: electron scattering opacity $\kappa_e = 0.34\,\mathrm{cm^2\,g^{-1}}$ considering Solar hydrogen abundance and complete ionisation (solid line), iron-bump opacity $\kappa_{Fe} = 1\,\mathrm{cm^2\,g^{-1}}$ (dashed line), and hydrogen recombination opacity $\kappa_H = 100\,\mathrm{cm^2\,g^{-1}}$ (dotted line). The blue dots mark the intersections of the ZAMS with the Fe- and H-bump Eddington luminosity. Figure taken from Langer et al. (2015).

they are expected to reach the Eddington limit at even lower masses, $M \gtrsim 30\,\mathrm{M}_\odot$. Furthermore, if one considers the extreme case, i.e. the opacities in the hydrogen recombination zone ($\kappa_\mathrm{H} = 100\,\mathrm{cm}^2\,\mathrm{g}^{-1}$), the Eddington limit may be reached down to $5\,\mathrm{M}_\odot$ in the envelopes of cool giants. Note that the opacity values assumed here are only approximate, and in the stellar interior only the luminosity carried by radiation must be considered while computing the Eddington factor. In detailed stellar models (cf. Chap. 2), the assumed model for convective energy transport might mediate this process.

The critical mass for reaching the Eddington limit can be further reduced by rotation (Langer 1997), as the centrifugal force directed outwards can have a destabilising effect. If density inhomogeneities or clumps are present in the stellar envelope, it might also influence the location of the Eddington limit in Fig. 1.4 (Owocki et al. 2004; Gräfener et al. 2012; Muijres et al. 2011). Since the Eddington luminosity is dependant on opacity (Eqn. 1.1), it is naturally a function of metallicity (cf. 1.1.2 and Sec. 1.1.3) and it is therefore expected that higher metallicity stars will reach the Eddington limit at lower masses. This trend was predicted by Ulmer & Fitzpatrick (1998) from their stellar atmosphere models. In Chap. 3 we will investigate in detail the metallicity dependence of the Eddington limit in stellar interiors.

Before the discovery of the iron opacity peak in the OPAL project, it was believed that very luminous stars might reach the Eddington limit close to their surface. Therefore this problem was approached from stellar atmosphere calculations. Lamers & Fitzpatrick (1988) introduced the concept of a "modified Eddington limit", where apart from the electron-scattering opacity the effects of metal line opacities were also considered in the model atmospheres. In contrast to the classical Eddington limit, the modified Eddington limit for a given stellar mass is no longer a horizontal line in the H-R diagram, because the opacity becomes temperature dependent. Later, Ulmer & Fitzpatrick (1998) investigated the location of the modified Eddington limit in the H-R diagram using updated atmosphere models (Fig. 1.5) and they found that the loci of constant Eddington factors in the H-R diagram show the so-called "Eddington trough" (Lamers & Noordhoek 1993), i.e., a decrease in the effective temperature range 60 000 − 15 000 K. This shape has a striking resemblance to the empirical Humphreys-Davidson (H-D) limit (Humphreys & Davidson 1979, 1994), a line in the upper H-R diagram beyond which no stars are observed. Furthermore, in Fig. 1.5 the observed upper luminosity limit of stars in the Large Magellanic Cloud roughly coincides with atmosphere models that have a maximum Eddington factor of ~0.9. However, note that in these model atmosphere calculations neither the iron opacity bump nor the physics of convective energy transport was included. It is therefore desirable to approach the problem from up-to-date stellar interior models to have a better understanding. In the next section, we will discuss the consequences of sub-surface layers approaching the Eddington limit in the stellar interior.

1.2.1 Envelope inflation

The radiation-pressure dominated regions in massive stars lead to extended, low-density envelopes, also called *inflated* envelopes (Stothers & Chin 1993; Ishii et al. 1999; Petrovic et al. 2006; Sanyal et al. 2015). This radial extension can increase the radii of stars by up to a factor of 100 (Sanyal et al. 2015), and is a key to understanding the evolution of very massive stars and their sub-surface instabilities. Envelope inflation, as we will investigate in Chap. 2, occurs when

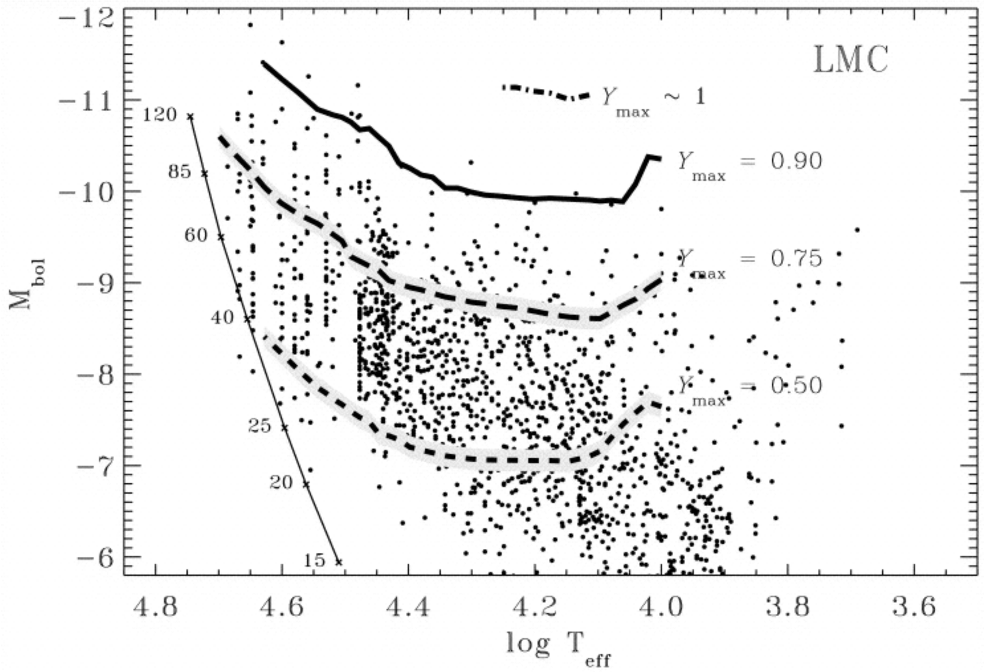

Figure 1.5: The LMC stars located in the upper H-R diagram (Fitzpatrick & Garmany 1990) with additional O stars from Walborn & Blades (1997). The loci of stellar atmosphere models for representative values of the maximum Eddington factor (referred to as $Y_{\rm max}$) are shown in thick solid and dashed lines. The location of the ZAMS (thin solid line) is drawn using a grid of stellar models interpolated between the Schaerer et al. (1993) and the Charbonnel et al. (1993) grids, and is labelled with the stellar masses (in units of $M_\odot$). The luminosity at $Y_{\rm max} = 1$ was estimated for effective temperatures between 13 000 − 18 000 K, for which stable models could be computed up to $Y_{\rm max} \simeq 0.98$. Figure from Ulmer & Fitzpatrick (1998).

the local radiative luminosity in the stellar envelope approaches the Eddington luminosity. It is therefore influenced by the opacity and convective efficiency in the stellar interior (cf. Sec. 1.1.3). Stothers & Chin (1993) first pointed out that the newly discovered iron opacity bump was responsible for the development of such envelope structures, and suggested that it might lead to dynamical instability in the envelopes. The density profiles of a relatively low-mass star and a very massive star on the ZAMS is shown in Fig. 1.6. While in the $3\,M_\odot$ model the density drops steeply in the outer layers, the $100\,M_\odot$ model exhibits a pronounced core-halo structure with an inflated, dilute envelope that occupies $\sim 30\%$ of the stellar radius, but only has a mass of $\sim 6 \times 10^{-5}\,M_\odot$. Close to the surface the $100\,M_\odot$ model also develops a density inversion (Langer 1997; Sanyal et al. 2015, cf. Chap. 2). In Chap. 3.3 we will show from stellar structure equations why envelope inflation occurs near the Eddington limit.

The envelope inflation effect has been previously found for hot stars: massive zero-age main-sequence stars (Ishii et al. 1999) and chemically homogenous, hydrogen-free Wolf-Rayet stars (Petrovic et al. 2006; Gräfener et al. 2012). The region in the H-R diagram populated by yellow and red supergiants have not been explored in the context of envelope inflation. Although Asplund (1998) studied atmospheres of cool stars and found super-Eddington layers and density inversions, he did not find envelope inflation in his model atmospheres, probably because the

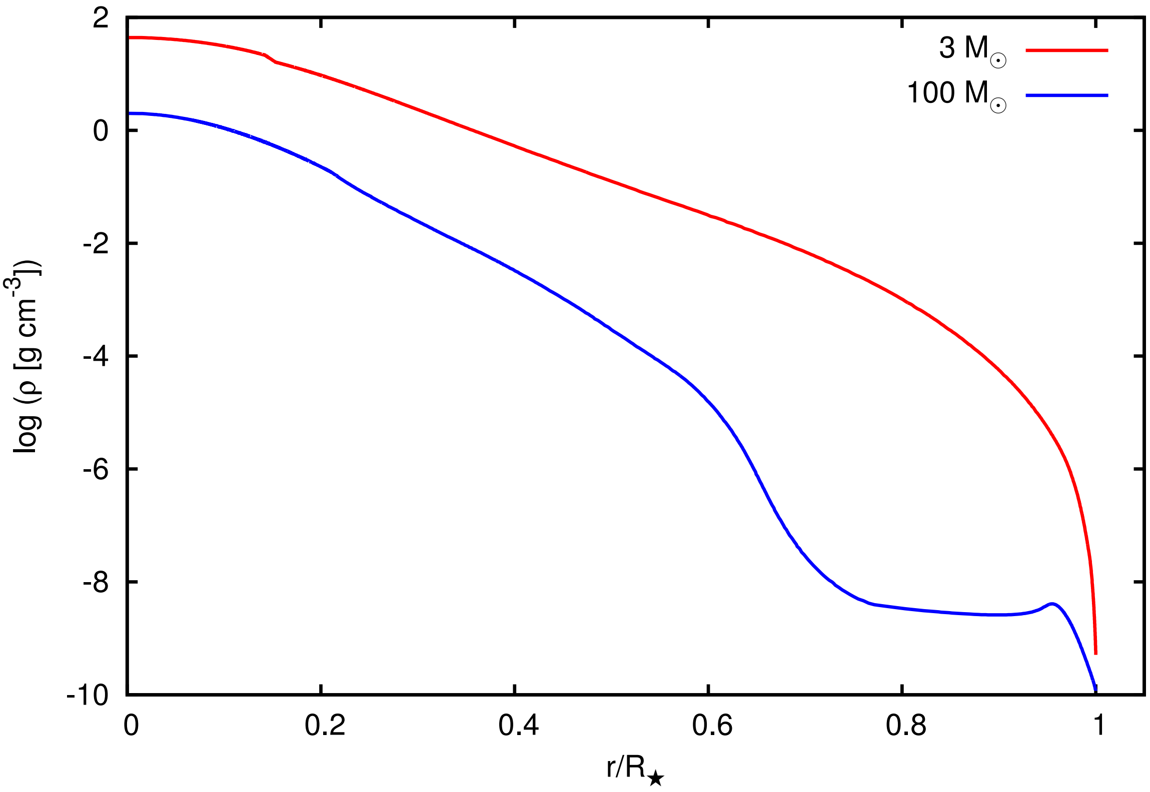

Figure 1.6: Density profile of a $3\,M_\odot$ and a $100\,M_\odot$ ZAMS model computed with a Solar chemical composition. The radial co-ordinate r is normalised to the stellar radius $R_\star$.

iron opacity peak was not included.

The question of stability naturally arises for these loosely-bound inflated envelopes that are on the verge of being unstable. Linear stability analyses predict these envelopes suffer from strange-mode instability with growth times comparable to the dynamical timescale (Gautschy & Glatzel 1990; Glatzel & Kiriakidis 1993a,b; Glatzel 1994; Saio et al. 1998). Recent efforts have been made by Jiang et al. (2015) to investigate their stability with three-dimensional (3-D) hydrodynamic simulations. The key result from this study is that the inflated structure persists in sophisticated 3-D models, and therefore this effect is not just an artefact of one-dimensional models.

Having introduced the concept of Eddington limit and envelope inflation, we will discuss briefly in the next couple of sections two special types of stars: Luminous Blue Variables and Wolf-Rayet stars, that are directly related to these concepts.

1.2.2 Luminous Blue Variables

Luminous Blue Variables (LBVs; Conti 1984), as the name suggests, are hot, luminous stars which show irregular variability although the definition is not very clear in the literature (See Humphreys & Davidson 1994, for a review). A very massive O-type star ($\approx 100\,M_\odot$) is thought to evolve through a transitionary LBV phase ($10^4 - 10^5$ years) before losing its hydrogen-rich envelope and becoming a Wolf-Rayet star (Langer et al. 1994, cf. Sec. 1.2.3). Although their evolutionary state is a matter of debate, LBVs are generally believed to be post main-sequence stars based on the chemical composition of the ejected material around them, and have even been suggested to be supernova progenitors (Kotak & Vink 2006; Pastorello et al. 2007; Groh et al. 2013).

Because of their high luminosity and unstable nature, one might expect that LBVs are related to the Eddington limit, and indeed this connection was shown from stellar atmosphere calculations (Lamers 1997; Ulmer & Fitzpatrick 1998). It is generally believed that a massive star with a hydrogen-rich envelope evolves towards cooler surface temperatures at a roughly constant luminosity, but undergoes heavy mass-loss such that its L/M ratio increases. This brings its atmosphere closer to the modified Eddington limit (see Fig. 1.5), and the star appears as an LBV. At this stage, the atmosphere becomes loosely bound such that stronger mass-loss sets in and the evolution proceeds bluewards thereafter. More massive stars will have a higher L/M and hence will reach the modified Eddington limit in their atmospheres at higher surface temperatures. This is believed to be the reason for the absence of Galactic red supergiants above $L \simeq 6 \times 10^5\,\mathrm{L}_\odot$, which defines the the H-D limit.

Furthermore, the fact that normal OB supergiants are located in the same region of the H-R diagram as LBVs but do not show the same kind of variability is also attributed to the fact that LBVs are closer to the modified Eddington limit (Lamers 1997). However, the effect of envelope inflation could not have been found from the stellar atmosphere computations because inflation is triggered in the deeper hydrostatic layers which are outside the computational domain of stellar atmosphere codes.

Luminous Blue Variables can be broadly divided into two categories – the S Doradus type variables that are relatively common, and the rare ones that undergo giant eruptions, like η Carinae. We briefly describe them below.

S Doradus variables

These LBVs, with S Dor being the prototypical example, undergo horizontal excursions in the H-R diagram, at a roughly constant bolometric luminosity. In the hot state, they are located within a narrow strip in the H-R diagram, also called the “S Dor instability strip” (Fig. 1.7). Their visual brightness varies by roughly $1-2$ mag over a characteristic timescale of a few years to decades. Most of the LBVs discovered are of the S Dor type, and some of the well-known ones are shown in Fig. 1.7. Interestingly, all the S Dor-like LBVs have roughly the same surface temperature at their visual maximum, and appear as supergiants. Apart from the S Dor cycles, some LBVs like HR Car also show what are called microvariations (Lamers et al. 1998), i.e., small photometric variations with amplitudes of $10 - 100$ mmag on typical timescales of a few weeks to months.

Initially it was speculated that the temperature changes during a S Dor cycle were actually caused by an increase in the mass-loss rate of the star, that makes the wind optically thick and forms a “pseudo-photosphere” (Davidson 1987). Later, it was shown from stellar atmosphere models (Leitherer et al. 1989; de Koter et al. 1996) that the mass-loss rates were not strong enough to form the pseudo-photospheres, and indeed the variability corresponds to physical

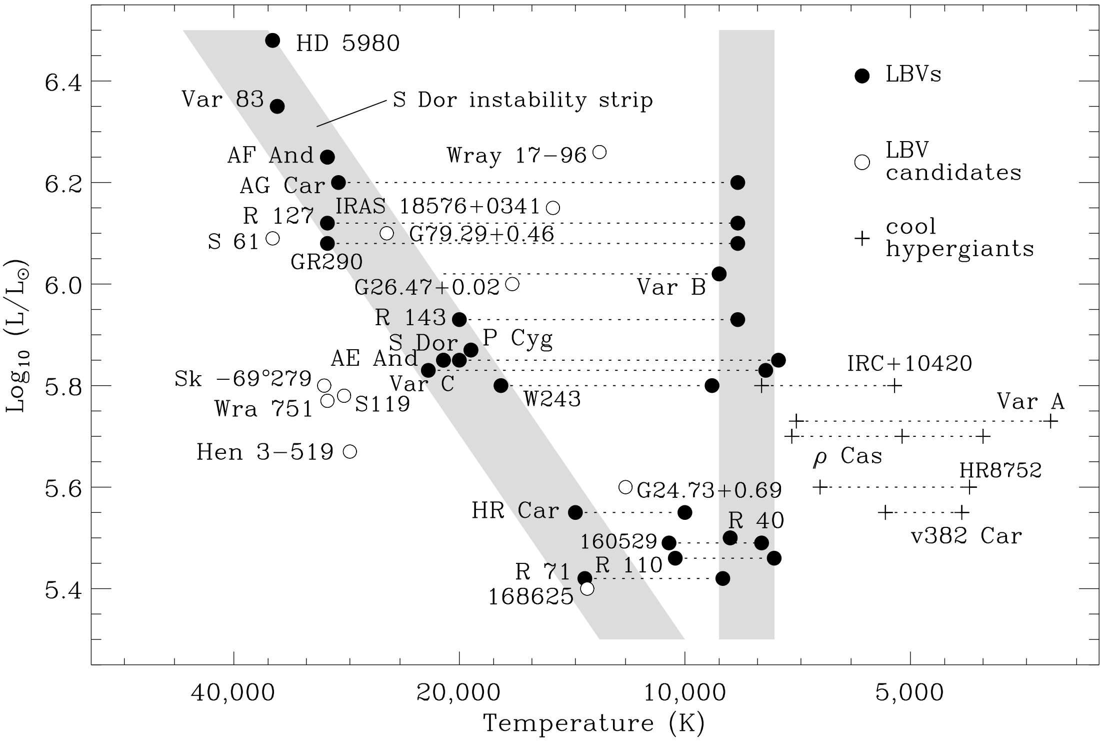

Figure 1.7: Hertzsprung-Russell diagram showing some of the known LBVs and LBV candidates. The grey bands show the hot and the cool ends of the instability strip. The dotted lines represent the range in temperatures over which the stars are known to vary. The LBV candidates are those for which no photometric variability has been confirmed, but show spectroscopic similarity to the bonafide LBVs. Figure taken from Smith et al. (2004).

changes in the radius of the star. Recently, Smith & Tombleson (2015) have suggested that the S Dor variables might also be products of binary evolution. Although no convincing theoretical model for the instability exists, envelope inflation in the outer layers of a massive star have been speculated to be related to the S Dor variability (Gräfener et al. 2012).

Giant Eruptions

A second class of LBVs undergo eruptive episodes, where several solar masses may be lost in a short span of a few years to decades. The prototypical example in this class is the spectacular η Carinae (Fig. 1.8), which lost $10 - 20\,M_\odot$ of material in the 'Great eruption' in the 19th century, spanning $\sim$ 20 years. Such high mass-loss rates can not be achieved by line-driven winds (Owocki et al. 2004). They are located very close to the H-D limit (Humphreys & Davidson 1979) on the H-R diagram. However, in the act of an outburst they radiate at many times their Eddington luminosity and reside beyond the H-D limit. These LBVs are the most unstable stars known, except perhaps the supernova progenitors. In fact, the energy released in the Giant Eruption was $\sim 10^{50}$ erg, which rivals the energy output of a supernova. Hence, these LBVs are also sometimes called supernova imposters. Although such eruptive events are much rarer compared to the S Dor analogues, Massey et al. (2007) has pointed out that this might be an observational bias. It is not clear whether LBVs go through multiple eruptive episodes, and if so, how frequently they recur. However, recent transient searches have been discovering many extragalactic supernova imposters and many of them are believed to be LBV-like Giant Eruptions (Smith 2015; Khan et al. 2015).

As far as theoretical models are concerned, not much is known about the structure and the evolutionary stage of LBVs that undergo Giant Eruption-like episodes. It is beyond doubt that they are close to the Eddington limit, but what triggers the violent instability and causes the phenomenon is unclear, and relatively unexplored. A few possibilities have been suggested in the literature, including ionisation-induced dynamical instability (Stothers & Chin 1993), super-Eddington winds (Owocki et al. 2004), and mergers of two massive stars (Justham et al. 2014; Portegies Zwart & van den Heuvel 2016), but none of them are conclusive. A firm understanding of the LBV phenomenon will be a major step towards understanding the evolution of massive stars. The relationship between massive main-sequence stars and LBVs has been discussed in Chapter 2.

1.2.3 Wolf-Rayet stars

Wolf-Rayet (WR) stars, first discovered at the Paris Observatory by astronomers Charles Wolf and Georges Rayet in the Cygnus constellation, are defined spectroscopically as stars which show broad emission lines in their spectra, unlike O stars that predominantly show narrow absorption lines. Based on which emission lines are present in the spectra, they are further subdivided into WN type, showing strong helium and nitrogen lines, WC type, showing carbon lines, and WO type, showing oxygen lines. The stellar wind is fast, with terminal velocities up to $\approx 6000\,\mathrm{km\,s^{-1}}$ (Drew et al. 2004), and dense. It is in this dense, opaque wind where the emission lines are formed. The wind mass loss rates of WR stars can be as high as $\sim 10^{-4}\,\mathrm{M_\odot\,yr^{-1}}$. Figure 1.9 shows a Hubble Space Telescope (HST) image of a typical WR star (WR 124) in our galaxy, along with the surrounding nebula created by the dense out-flowing matter from the central star. Since they are highly luminous ($10^3 - 10^6\,\mathrm{L_\odot}$) and very hot ($30\,000 - 200\,000\,\mathrm{K}$), WR stars have high photoionisation fluxes, and can account for $> 20\%$ of the total ionising photons emitted by young starburst galaxies like NGC 3603 (Drissen et al. 1995; Crowther 2007).

In the framework of single stars, the widely accepted pathway to form WR stars is the so-called *Conti scenario* (Conti 1975), first proposed by Peter Conti in 1975, where a massive star loses its hydrogen-rich envelope via strong stellar winds, thus exposing the ashes of its nuclear burning. These stars have large convective cores, because of which the nuclear burning products are mixed throughout this region, and appear at the surface once the hydrogen-rich layers are lost. In the Milky Way, classical WR stars, i.e., the hydrogen-free ones, are believed to be the descendants of massive O stars above $\sim 20 - 25\,\mathrm{M_\odot}$.

In sufficiently low metallicity environments where stellar winds are not as strong, the Conti scenario is not efficient. But WR features have been detected in low-metallicity stars as well, for e.g., in the dwarf galaxy I Zw 18(Kehrig et al. 2015), and are difficult to explain with typical single star models. Models of low metallicity, rapidly rotating massive stars are also predicted to form WR stars (Maeder 1987; Szécsi et al. 2015; Yoon & Langer 2005). These stars are

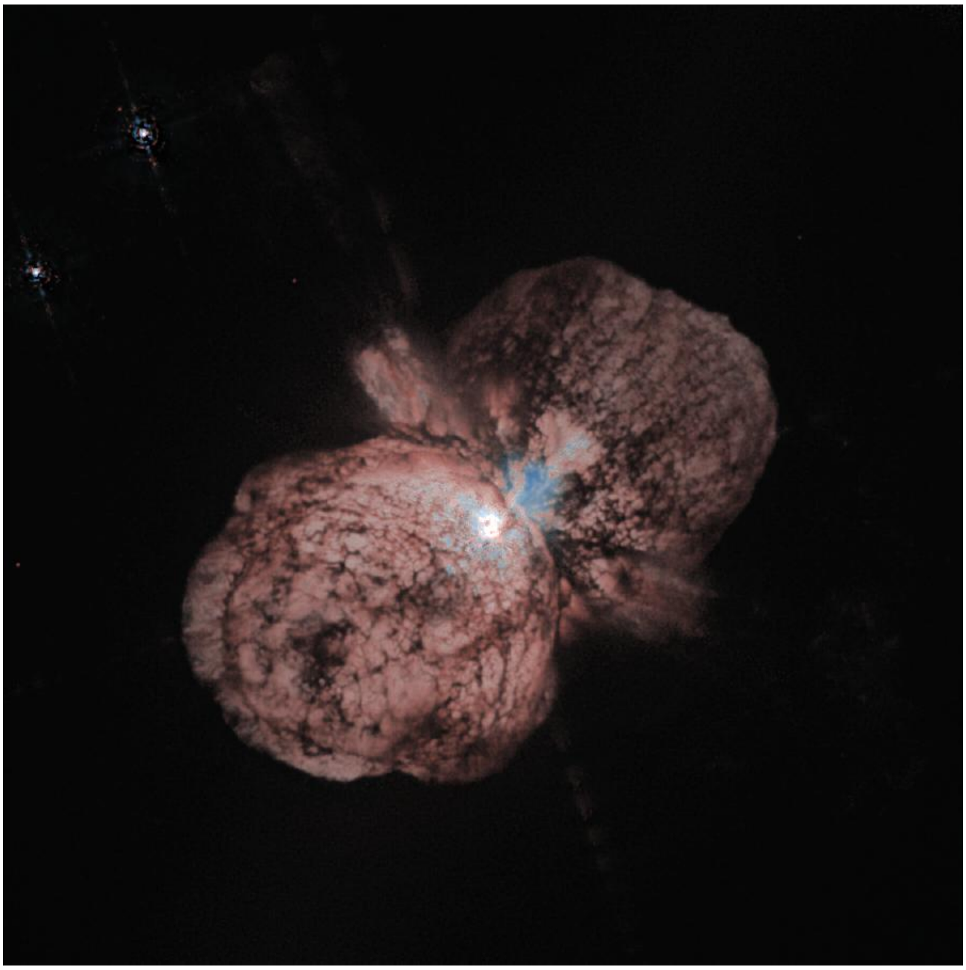

Figure 1.8: Hubble Space Telescope image of the massive binary Eta Carinae, located at a distance of 2300 kpc in the Carina constellation. *Photo credit:* Jon Morse (University of Colorado), and NASA.

rotating so fast that their interior is homogeneously mixed, and they evolve blue-wards in the H-R diagram, appearing as WR stars even in the core-hydrogen burning phase. Yet another pathway to forming WR stars is in close binaries, wherein the primary loses its hydrogen-rich envelope to the accreting secondary via Roche lobe overflow. In such cases, WR stars of much lower masses and metallicities can be formed, which would otherwise not be possible in the single star scenario (Woosley et al. 2010).

The classical Eddington factor has also been identified as they key parameter controlling the mass-loss rate and the evolution of very massive hydrogen-rich Wolf-Rayet stars (Vink et al. 2011; Gräfener et al. 2011). For $\Gamma_\mathrm{e} \gtrsim 0.7$ the dependence of $\dot{M}$ on Γ_e is very steep, $\dot{M} \propto \Gamma_\mathrm{e}^5$. Gräfener et al. (2011) suggested that it is not the hydrogen deficiency but the proximity to the classical Eddington limit that marks the start of the WR phase. A high value of Γ_e leads to the development of a strong stellar wind that consequently removes the hydrogen-rich envelope.

Theoretical models of WR stars also reach the Eddington limit in their interior aided by the iron bump opacity, and develop inflated envelopes that are characteristic of stars with a high luminosity-to-mass ratio (Petrovic et al. 2006; Gräfener et al. 2012; Grassitelli et al. 2016a). The

Figure 1.9: Hubble Space Telescope image of Wolf-Rayet star WR 124 surrounded by the nebula M1-67. The nebula is formed from the matter ejected by the star. *Photo credits:* Hubble Legacy Archive, NASA, ESA.

onset of envelope inflation makes the Galactic helium-ZAMS models bend redwards towards cooler effective temperatures above log $L/\mathrm{L}_\odot \sim 5.5$ (Köhler et al. 2015). Some of these inflated envelope models are also predicted to be pulsationally unstable (Glatzel et al. 1993; Grassitelli et al. 2016a), although no such candidate has been clearly identified yet.

WR stars are thought to explode as hydrogen-deficient Type Ib/c supernovae, sometimes associated with a gamma ray burst. In fact, in the *collapsar model* for long-duration gamma ray bursts (Woosley 1993), a rapidly rotating, compact WR star is needed as the progenitor. The physics of the evolution of WR stars up to their point of explosion (cf. Tramper et al. 2015), remains an active area of research, and forms the theme for Chapter 4 of this thesis.

1.3 Overview of the thesis

As we have elucidated in this introductory chapter, massive stars play an important role in the Universe and their evolution is very diverse and complex. In this thesis, we aim to – a) understand the behaviour of massive stars as they approach the Eddington limit, b) investigate their observational consequences, c) confront our state-of-the-art models with recent observations, and d) identify the limitations of our models. For this purpose we have extensively investigated evolutionary models of both non-rotating and rotating massive stars computed with a one-dimensional hydrodynamic stellar evolution code called the Binary Evolution Code (BEC). The details of the code can be found in Heger et al. (2000); Petrovic et al. (2005); Woosley et al. (2010); Brott et al. (2011); Yoon et al. (2012a); Sanyal et al. (2015).

The Eddington limit and envelope inflation in main-sequence stars

In Chap. 2, we explore the consequences of stellar models reaching the Eddington limit in their outer layers. For this study we present a grid of LMC metallicity models with initial masses up to $500\,\mathrm{M}_\odot$. Some of the evolutionary tracks from this model grid are shown in the H-R diagram in Fig. 1.10. We find that models with $M > 40\,\mathrm{M}_\odot$ reach the Eddington limit in their outer layers, and furthermore, many of our models exceed the Eddington limit by factors of up to seven. Instead of developing a super-Eddington outflow, they develop inflated envelopes such that the effective temperatures of these models gets lowered by a factor of a few. When the Eddington limit is exceeded in hydrostatic layers, the gas-pressure gradient is directed *inwards*, which leads to an ubiquitous density inversion.

We compare our models with the massive OB stars observed in the VLT-FLAMES Tarantula Survey, and find a general agreement. We find that some of our inflated models have particular relevance to the LBVs, as the hot edge of the S Dor variability strip in the H-R diagram (Smith et al. 2004) coincides with the boundary beyond which our models show strong inflation, and hence are prone to envelope instabilities. On the other hand, the coolest models in our grid, i.e. those with initial masses between $60 - 80\,\mathrm{M}_\odot$ (Fig. 1.10) contain several Solar masses in their inflated envelope and are located beyond the H-D limit. These massive envelopes are loosely bound to the star and are natural candidates for LBVs that undergo Giant Eruptions.

Although we investigated only massive stars, we predict that the Eddington limit is relevant to other types of stars and astrophysical phenomena, for example, in luminous post-AGB stars,

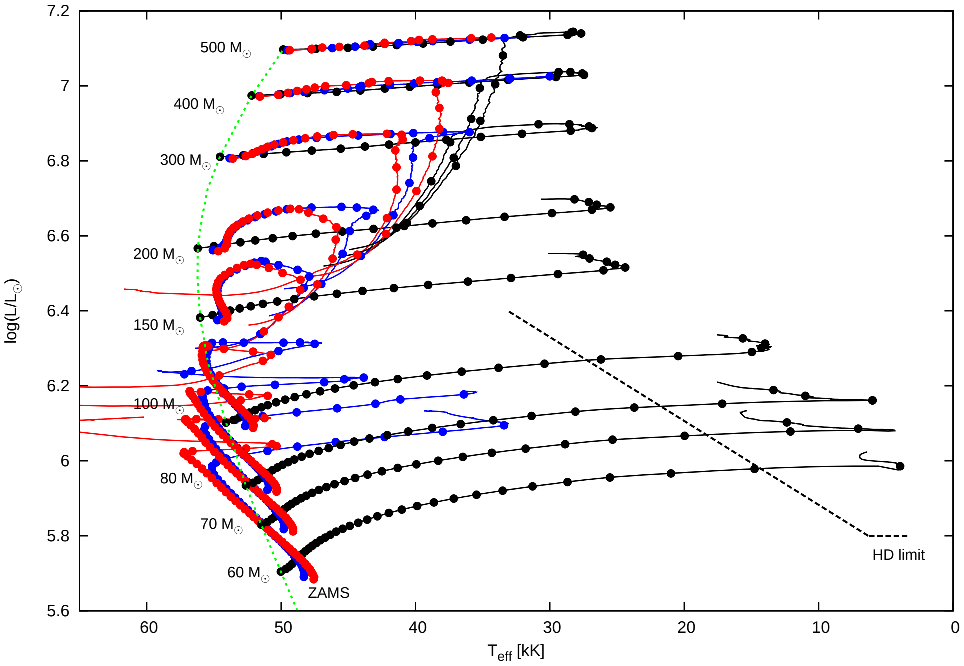

Figure 1.10: Evolutionary tracks of massive stars during their core hydrogen burning evolution in the Hertzsprung-Russell diagram (Köhler et al. 2015). For each selected initial mass (as labelled), tracks are shown for three different initial surface rotational velocities, $\upsilon_{\rm ZAMS} = 0, 400, 500\,{\rm km\,s^{-1}}$, in black, blue, and red, respectively. The time difference between two successive dots on each track is 10^5 yrs. The ZAMS is drawn as a green dashed line. The end of the tracks corresponds to the terminal age main sequence. The approximate location of the Humphreys-Davidson limit is indicated by the black dashed line (Humphreys & Davidson 1994).

X-ray bursts, R Corona Borealis stars and accreting compact objects. In rapidly rotating massive stars, the latitude dependence of envelope inflation might give rise to the ill-understood B[e] supergiants, which show a slow and dense equatorial wind and a fast polar wind at the same time (Zickgraf et al. 1985).

Metallicity dependence of envelope inflation

As mentioned in Sec. 1.1.2, the metallicity, especially the iron content, determines the strength of the iron bump opacity in the OPAL data (Iglesias & Rogers 1996). Therefore, low-metallicity massive stars stay more compact and are subject to weaker inflation (Brott et al. 2011; Szécsi et al. 2015; Sanyal et al. 2016).

Equipped with the results from Chap. 2, we explore the metallicity dependence of the Eddington limit and envelope inflation in Chap. 3. We investigate dense grids of stellar models computed with five metallicities, from Galactic to metal-free, and map the regions in the H-R diagram where we predict the existence of inflated envelopes for each metallicity. The ZAMS, and especially the TAMS bend towards cooler temperatures in the upper H-R diagram as a consequence of envelope inflation, and the critical mass above which we see this effect is a function of metallicity. We find that at lower metallicity inflation starts at higher luminosities. Furthermore, the loci of the maximum Eddington factor lines in the H-R diagram have the Eddington trough feature that was also found by Ulmer & Fitzpatrick (1998) from stellar atmosphere models. We also find that while the inflated envelopes in general contain very little mass ($< 10^{-2}\,\mathrm{M}_\odot$), in the extreme cases it can contain up to $\sim 100\,\mathrm{M}_\odot$ of material which might again be related to the LBV phenomena.

Shock breakout signals from inflated supernova progenitors

In 2008, using NASA's Swift X-ray telescope (Soderberg et al. 2008) serendipitously discovered for the first time, a supernova in the act of explosion. While they were doing follow-up observations of the supernova SN 2007uy in the galaxy NGC 2770, they spotted an extremely bright X-ray outburst (see Fig. 1.11), which we now know as SN 2008D. They detected X-ray photons from the shock front of the collapsing star, when the shock is sufficiently close to the surface such that photons can leak out and reach the detectors. However, the duration of the X-ray signal was about 300 s with a rise time of about ~ 60 s. SN 2008D was of Type Ib with no hydrogen or silicon features in its spectrum, and thus its progenitor is believed to be a compact WR star for which the rise time of the shock breakout is expected to be ~ 0.5 s, 100 times shorter than what was observed. There have been models proposed for explaining the long shock breakout signal of SN 2008D, but they usually invoke exotic scenarios like the optically thick wind model by Svirski & Nakar (2014a) that assumes a high mass-loss rate of $10^{-4}\,\mathrm{M}_\odot\,\mathrm{yr}^{-1}$ a few years prior to the explosion.

Until now we have explored envelope inflation in main-sequence stars. In Chap. 4, we explore the observational consequence of a hydrogen-free supernova progenitor possessing an inflated envelope. We show for the first time that the rise times of shock breakout signals from supernovae can be extended significantly if the progenitor has an inflated envelope. Our Wolf-Rayet star models with $R \sim \mathrm{R}_\odot$ can lead to shock breakout signals that are longer than ~ 100 sec. Our model explains not only the enigmatic long shock breakout signal observed in Type Ib SN 2008D, but also the estimated mass and the mass-loss rate of the progenitor. Further observations of events like SN 2008D might serve as a test for the existence of inflated envelopes in general.

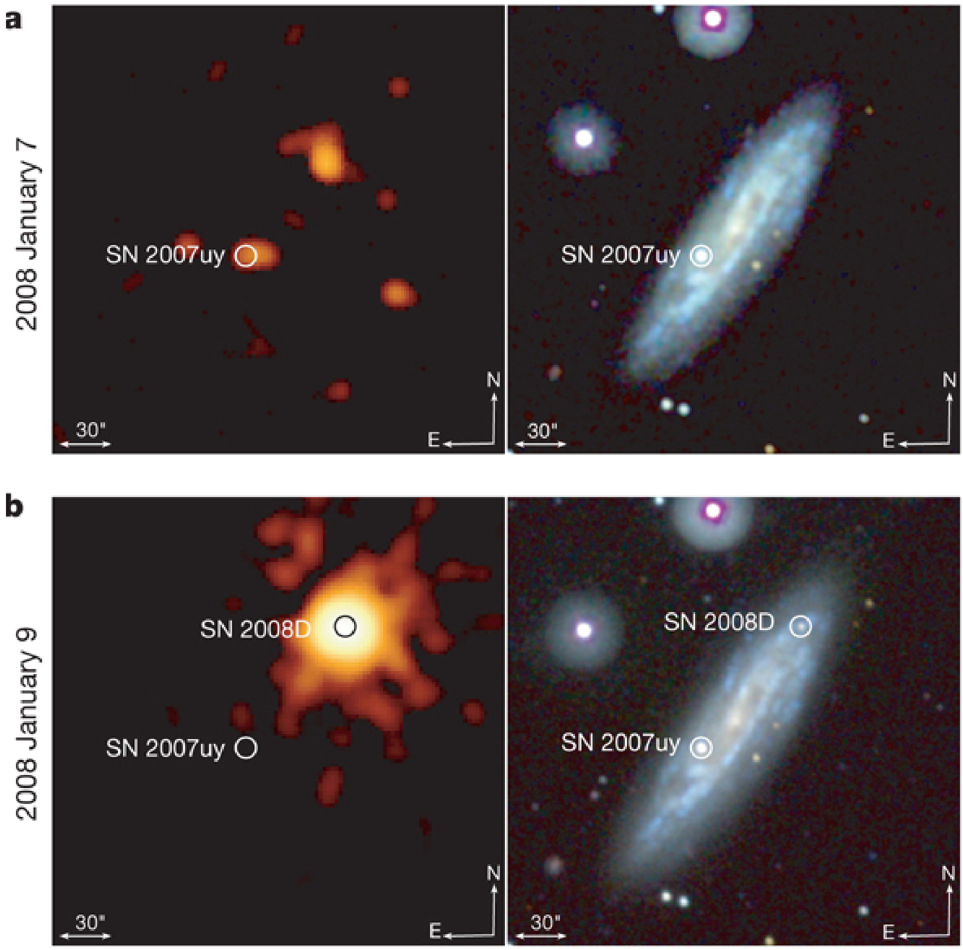

Figure 1.11: Location of SN 2007uy and SN 2008D in visual and UV light (right) and in X-rays (left) before (top panel) and after (bottom panel) the explosion of SN 2008D. *Image credit:* NASA Swift team.

CHAPTER 2

Massive main-sequence stars evolving at the Eddington limit

D. Sanyal, L. Grassitelli, N. Langer and J. M. Bestenlehner

Astronomy & Astrophysics, 2015, 580, A20

2.1 Introduction

Massive stars are powerful engines and strongly affect the evolution of star-forming galaxies throughout cosmic time (Bresolin et al. 2008). In particular the most massive stars produce copious amounts of ionising photons (Doran et al. 2013), emit powerful stellar winds (e.g. Kudritzki & Puls 2000; Smith 2014) and, in their final explosions, are suspected to produce the most energetic and spectacular stellar explosions, as pair-instability supernovae (Kozyreva et al. 2014), superluminous supernovae (Gal-Yam et al. 2009), and long-duration gamma-ray bursts (Larsson et al. 2007; Raskin et al. 2008).

Massive main-sequence stars, which we understand here as those that undergo core hydrogen burning, have a much higher luminosity than the Sun, as they are known to obey a simple mass-luminosity relation, $L \sim M^{\alpha}$, with $\alpha > 1$. However, whereas this relation is very steep near the solar mass ($\alpha \simeq 5$), it is shown in Kippenhahn et al. (1990) that $\alpha \to 1$ for $M \to \infty$. Indeed, Köhler et al. (2015) find $\alpha \simeq 1.1$ for $M = 500\,\mathrm{M}_{\odot}$.

Since the Eddington factor is proportional to L/M, it is debated in the literature whether main-sequence stars of higher and higher initial mass eventually reach the Eddington limit (Langer 1997; Crowther et al. 2010; Maeder et al. 2012). The answer is clearly: yes, they do. Even when only electron scattering is considered as a source of radiative opacity, the Eddington limit corresponds to a luminosity-to-mass ratio of $\mathcal{R} := \log\left(\frac{L}{\mathrm{L}_{\odot}} / \frac{M}{\mathrm{M}_{\odot}}\right) \simeq 4.6$ (Langer & Kudritzki 2014) for hot stars with a solar helium abundance. This is extremely close to the $\mathcal{R}$-values obtained for models of supermassive stars, where this ratio is nearly mass independent (Fuller et al. 1986; Kato 1986). In fact, Kato (1986) showed that zero-age main-sequence models computed only with electron scattering opacity reach the Eddington limit at a mass of about $\sim 10^{5}\,\mathrm{M}_{\odot}$.

Whether supermassive stars exist is an open question. Also the mass limit of ordinary stars is presently uncertain (Schneider et al. 2014), however, there is ample evidence for stars with initial masses well above $100\,\mathrm{M}_\odot$ in the local Universe. A number of close binary stars have been found with component initial masses above $100\,\mathrm{M}_\odot$ (Schnurr et al. 2008, 2009; Taylor et al. 2011; Sana et al. 2013). Crowther et al. (2010) proposed initial masses of up to $300\,\mathrm{M}_\odot$ for several stars in the LMC, based on their luminosities. Bestenlehner et al. (2014) identified more than a dozen stars more massive than $100\,\mathrm{M}_\odot$ from the sample of $\sim$ 1000 OB stars near 30 Doradus, which are analysed in the frame of VLT-Flames Tarantula Survey (Evans et al. 2011). The hydrogen-rich stars among them have measured $\mathcal{R}$-values of up to 4.3. In hot stars with finite metallicity, the ion opacities can easily exceed the electron scattering opacity (Iglesias & Rogers 1996). It is thus to be expected that the true Eddington limit, which accounts for all opacity sources, is located at $\mathcal{R}$-values of 4.3 or below. This implies that these stars should in fact also have reached, or exceeded their Eddington limit.

In this paper, we explore the question of massive main-sequence stars reaching, or exceeding the Eddington limit from the theoretical side. We show by means of detailed stellar models, as described in Section 2.2, that even all stars more massive than $\sim 40\,\mathrm{M}_\odot$ are found to reach the Eddington limit. In Section 2.3, we demonstrate the need to properly define a local Eddington factor in the stellar interior, which we then use in Section 2.4 to show that when it exceeds the critical value of one, the stellar envelope becomes inflated. We show further in Section 2.5 and 2.6 that super-Eddington conditions can lead to density inversions and induce convection. We compare our results to previous studies in Section 2.7, and relate them to observations in Section 2.8, before summarising our conclusions in Section 2.9.

2.2 Stellar models

The grids of the stellar models we used have been published in Brott et al. (2011) and Köhler et al. (2015). We consider only the core hydrogen burning models computed with LMC metallicity. Each stellar evolution sequence computed by Brott et al. (2011) and Köhler et al. (2015) consists of typically 2000 individual stellar models. However, the full amount of data defining a stellar model is only stored for a few dozen time points per sequence, in non-regular intervals. We analyse those stored models. This scheme has the disadvantage that the density of models in the investigated parameter space is not always as high as it should be ideally. Still, as shown below, it allows for a thorough sampling of the considered parameter space, and it is fully consistent with the results already published.

The stellar models were computed with a state-of-the-art, one-dimensional hydrodynamic implicit Lagrangian code (BEC), which incorporates latest input physics (for details, see Braun 1997; Yoon et al. 2006; Brott et al. 2011; Köhler et al. 2015, and references therein). Convection was treated as in the standard non-adiabatic mixing length approach (Böhm-Vitense 1958; Kippenhahn et al. 1990) and a mixing length parameter of $\alpha = l/H_\mathrm{p} = 1.5$ (Langer 1991) was adopted, with l and H_p being the mixing length and the pressure scale height, respectively. This value of the mixing length parameter leads to a good representation of the Sun (Suijs et al. 2008), whereas its calibration to multi-dimensional hydrodynamic models shows that it tends to decrease towards lower gravities (Trampedach et al. 2014; Magic et al. 2015). The convective

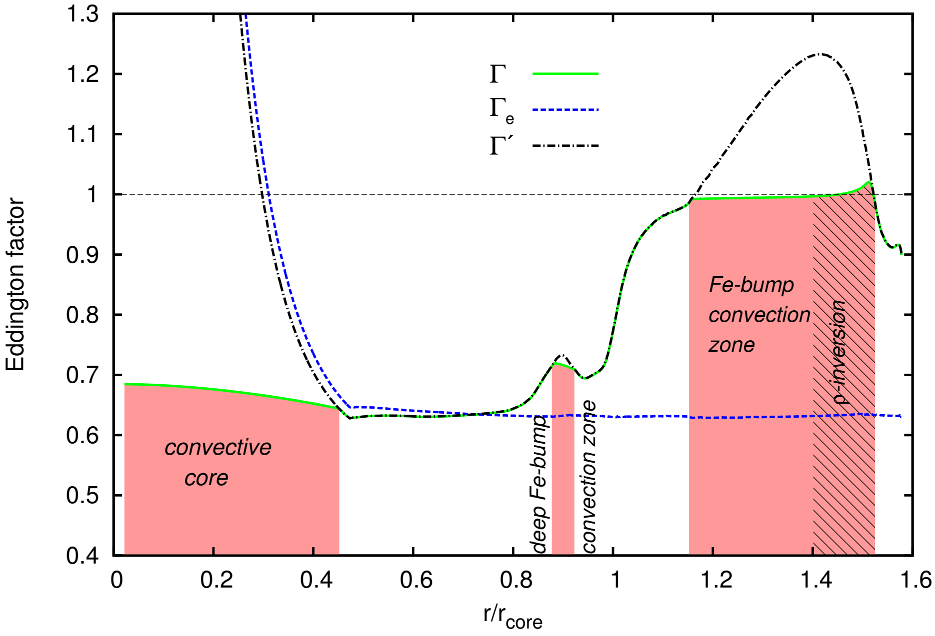

Figure 2.1: The different Eddington factors inside a 285 $M_\odot$, non-rotating, main-sequence model with $\log L/L_\odot$ = 6.8 and $T_{\rm eff}$ = 46600 K (cf. Fig. 2.9 and Sec. 2.10.1). The shaded areas mark the different convection zones and the hatched area marks the region with a density inversion. The radius of the un-inflated core is denoted as $r_{\rm core}$ (defined in Sect. 2.4). The black dashed horizontal line is drawn at $\Gamma = 1$ for convenience.

velocities were limited to the local value of the adiabatic sound speed. The contribution of turbulent pressure (de Jager 1984) was neglected, since it is not expected to be important in determining the stellar hydrostatic structure (Stothers 2003). Indeed, our recent study which includes turbulent pressure (Grassitelli et al. in preparation) shows that e.g. for an 80 $M_\odot$ evolutionary sequence, the stellar radius is increased over that of models without turbulent pressure by at most a few per cent at any time during its main-sequence evolution. Rotational mixing of chemical elements, following Heger et al. (2000), and transport of angular momentum by magnetic fields due to the Spruit-Taylor dynamo were also included (Spruit 2002). The efficiency parameters f_c and f_μ for rotational mixing were set to 0.0228 and 0.1, respectively (Brott et al. 2011). Radiative opacities were interpolated from the OPAL tables (Iglesias & Rogers 1996). The opacity enhancement due to Fe-group elements at $T \sim 200$ kK plays a vital role in determining the envelope structure in our stellar models. Even though flux-mean opacities are appropriate to study the momentum balance near the stellar photosphere, in the following we only consider the Rosseland mean opacities, which are thought to behave very similarly to the flux-mean opacities especially at an optical depth larger than one.

The outer boundary condition of the stellar models corresponds to a plane-parallel grey atmosphere model on top of the photosphere. In other words, the effective temperature was used as a boundary condition at a Rosseland optical depth of 2/3. The adopted stellar wind mass-loss recipe leads to small, but finite outflow velocities in the outermost layers, which induces a slight

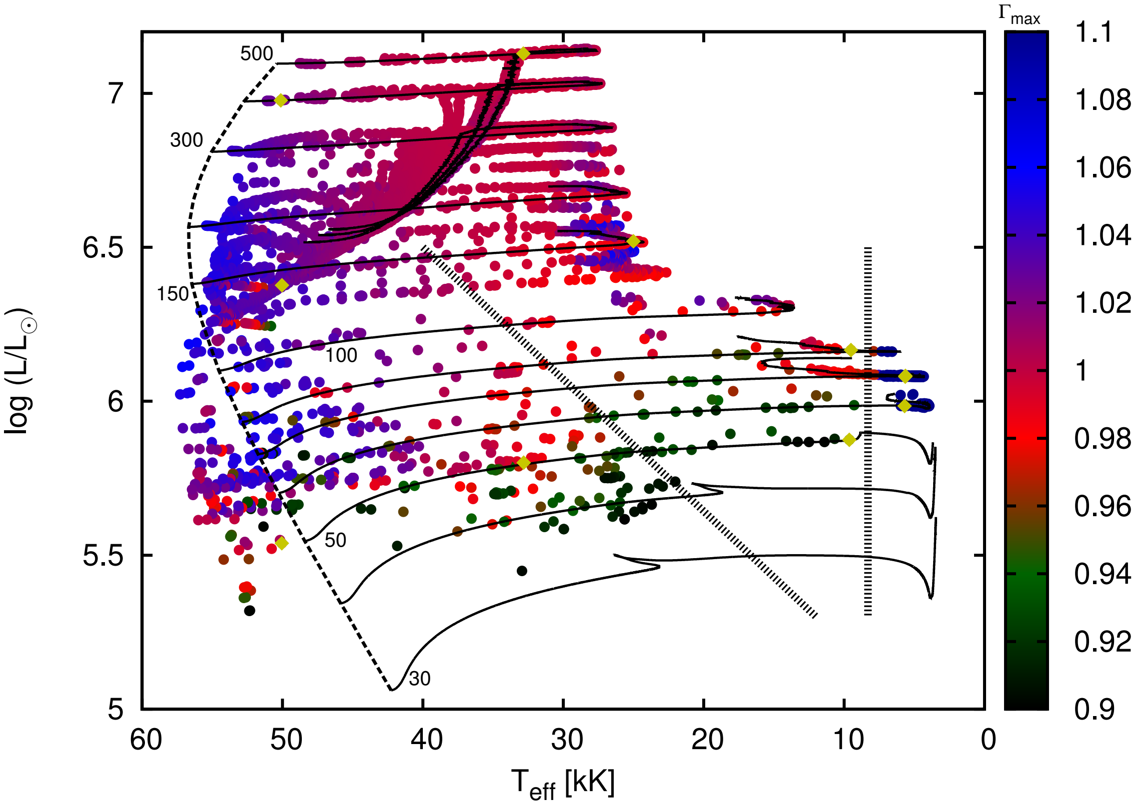

Figure 2.2: Positions of the analysed stellar models with $\Gamma_{\max} > 0.9$ in the Hertzsprung-Russell diagram (coloured dots). Models with $\Gamma_{\max} > 1.1$ are coloured dark blue. The solid lines show the evolutionary tracks of non-rotating stellar models (Köhler et al. 2015). The initial masses are marked in units of solar mass. The dashed line corresponds to the zero-age main-sequence of the non-rotating models. The hot and the cool edges of the S Dor instability strip from (Smith et al. 2004) are indicated with thick dotted lines. The interior structures of the models marked with yellow diamonds are shown in Sec. 2.10.4.

deviation from hydrostatic equilibrium.

The mass-loss prescription from Vink et al. (2000, 2001) was employed to account for the winds of O- and B-type stars. Moreover, parameterized mass-loss rates from Nieuwenhuijzen & de Jager (1990) were used on the cooler side of the bi-stability jump, i.e. at effective temperatures less than 22000 K, if the Nieuwenhuijzen & de Jager (1990) mass-loss rate exceeded that of Vink et al. (2000, 2001). Wolf-Rayet (WR) type mass-loss was accounted for using the empirical prescription from Hamann et al. (1995) divided by a factor of 10 (Yoon et al. 2006), when the surface helium mass fraction became greater than 70%.

Evolutionary sequences of massive stars, with and without rotation, were computed up to an initial mass of $500\,\mathrm{M}_\odot$, starting with LMC composition. The initial mass fractions of hydrogen, helium and metals were taken to be 0.7391, 0.2562, and 0.0047 respectively, in accordance with the observations of young massive stars in the LMC (Brott et al. 2011).

2.3 The Eddington Limit

The Eddington limit refers to the condition in which the outwards radiative acceleration in a star balances the inwards gravity, in hydrostatic equilibrium. It is a concept that is thought to apply at the stellar surface, in the sense that if the Eddington limit is exceeded, a mass outflow should arise (Eddington 1926; Owocki et al. 2004). If we denote the gravity as $g = GM/r^2$ and the radiative acceleration mediated through the electron scattering opacity as $g_{\mathrm{rad}} = \kappa_{\mathrm{e}} L/4\pi r^2$, then the classical Eddington factor Γ_{e} is defined as

$$\Gamma_{\mathrm{e}} := \frac{L}{L_{\mathrm{Edd}}} = \frac{g_{\mathrm{rad}}}{g} = \frac{\kappa_e L}{4\pi c G M}, \tag{2.1}$$

where L, M, and κ_{e} are the luminosity, mass, and electron-scattering opacity, respectively, with the physical constants having their usual meaning. The classical Eddington parameter Γ_{e} therefore does not depend on the radius r as the inverse r^2 scaling in both g_{rad} and g cancel out. Whereas Γ_{e} is often convenient to consider, it provides a sufficient instability criterion to stars, but not a necessary one because usually the true opacity exceeds the the electron scattering opacity significantly and also contributes to the radiative force.

As it turns out below, even when the Rosseland mean opacities are used, the models we analyse practically never reach the Eddington limit at their surface. Therefore, we instead consider the Eddington factor in the stellar interior as

$$\Gamma'(r) := \frac{L(r)}{L_{\mathrm{Edd}}(r)} = \frac{\kappa(r) L(r)}{4\pi c G M(r)}, \tag{2.2}$$

where $M(r)$ is the Lagrangian mass coordinate, $\kappa(r)$ is the Rosseland mean opacity, and $L(r)$ is the local luminosity (Langer 1997). However, $\Gamma'(r) > 1$ also does not provide a stability limit in the stellar interior because the stellar layers turn convectively unstable following Schwarzschild's criterion when $\Gamma'(r) \rightarrow 1$ (Joss et al. 1973; Langer 1997). As the luminosity transported by convection does not contribute to the radiative force, we subtract the convective luminosity in the above expression and redefine the Eddington factor as

$$\Gamma(r) := \frac{L_{\rm rad}(r)}{L_{\rm Edd}(r)} = \frac{\kappa(r)(L(r) - L_{\rm conv}(r))}{4\pi c G M(r)}. \tag{2.3}$$

For example, near the stellar core where convective energy transport is highly efficient, $\Gamma(r)$ stays well below unity in spite of $\Gamma'(r) \gg 1$ and no instability, i.e. departure from hydrostatic equilibrium, occurs (see Fig. 2.1). In the rest of the paper we refer to $\Gamma(r)$ as the Eddington factor unless explicitly specified otherwise.

Even with this definition, a super-Eddington layer inside a star does not necessarily lead to a departure from hydrostatic equilibrium or a sustained mass outflow. In the outer envelopes of massive stars, non-adiabatic conditions prevail and convective energy transport is highly inefficient, which pushes $\Gamma(r)$ close to (or above) one. We find that the stellar models counteract this kind of a super-Eddington luminosity by developing a positive gas pressure gradient, thus restoring hydrostatic equilibrium (Langer 1997; Asplund 1998). In these situations, the canonical definition of $L_{\rm edd}$ being the maximum sustainable radiative luminosity locally in the stellar interior (in hydrostatic equilibrium) breaks down and loses its significance. As we see below, the radiative luminosity beneath the photosphere can be up to a few times the Eddington luminosity.

In Fig. 2.1, the behaviour of Γ and Γ' is shown along with the electron-scattering Eddington factor $\Gamma_{\rm e}$ in a $285\,{\rm M}_\odot$ non-rotating stellar model, which provides an educative example (see Sec. 2.10.4 for further examples). As explained above, Γ' and $\Gamma_{\rm e}$ are significantly greater than one in the convective core of the star. The indicated sub-surface convection zones are caused by the opacity peaks at $T \sim 1.5 \times 10^6$ K (deep iron bump) and at $T \sim 2 \times 10^5$ K (iron bump). Near the bottom of the inflated envelope ($r/r_{\rm core} \gtrsim 1$; see Sect. 2.4 for the definition of $r_{\rm core}$), Γ approaches one and the Fe opacity bump drives convection. An extended region with $\Gamma \approx 1$ follows. A thin shell very close to the photosphere contains the layers with a positive density gradient and with $\Gamma > 1$.

The stellar models have been computed with a hydrodynamic stellar evolution code, however, because of the large time steps required for stellar evolution calculations, non-hydrostatic solutions are suppressed by our numerical scheme. The resulting hydrostatic structures are still valid solutions of the hydrodynamic equations (see Heger et al. 2000; Kozyreva et al. 2014, for the equations to be solved). Models computed with time steps small enough to resolve the hydrodynamic timescale reveal that some, and potentially many of our models are pulsationally unstable, as will be shown in a forthcoming paper. However, in the cases analysed so far, the pulsations saturate and do not lead to a destruction or ejection of the inflated envelopes. In this respect, we consider our analysis of the hydrostatic equilibrium structures as useful.

2.3.1 Effect of rotation on the Eddington limit

The effect of the centrifugal force on the structure of rotating stellar models has been studied by a number of groups in the past, including Heger et al. (2000) and Maeder & Meynet (2000). This is done by describing the models in a 1-D approximation where all variables are taken as averages over isobaric surfaces (Kippenhahn & Thomas 1970). The stellar structure equations

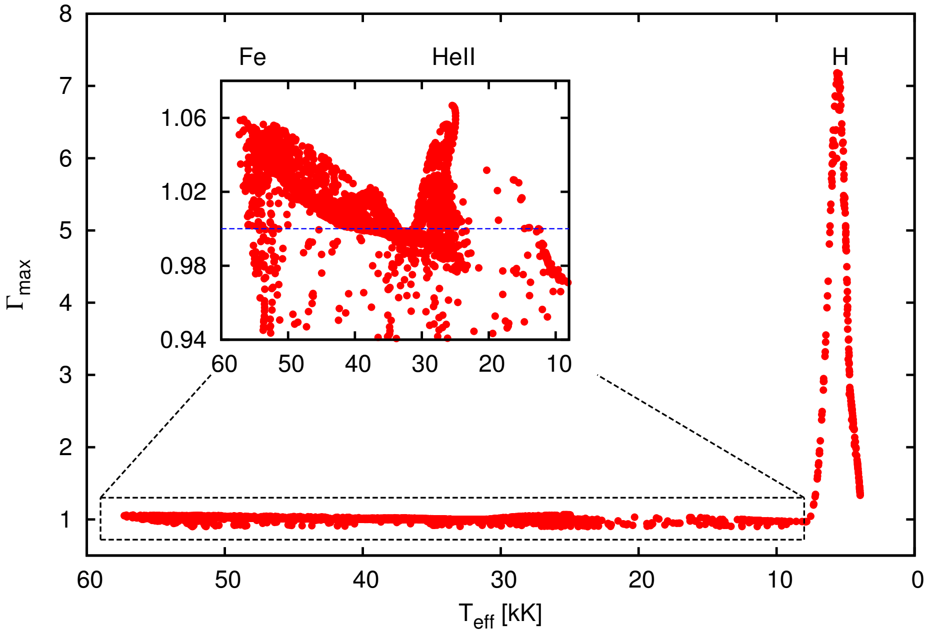

Figure 2.3: Maximum Eddington factor in the analysed stellar models as a function of $T_{\rm eff}$ for all stellar models shown in Fig. 2.2, i.e. with $\Gamma_{\rm max} > 0.9$. The three peaks in $\Gamma_{\rm max}$ at $T_{\rm eff}$/kK of ~ 55, 25, and 5.5 correspond to the three opacity bumps associated with the ionisation zones of Fe, HeII and H respectively. *Inset*: Models with $\Gamma_{\rm max} > 0.94$ and $T_{\rm eff}/\mathrm{kK} \gtrsim 10\,\mathrm{kK}$. The blue horizontal line at $\Gamma_{\rm max} = 1$ is drawn for reference.

are modified to include the effect of the centrifugal force (Endal & Sofia 1976). The equation of hydrostatic equilibrium becomes

$$\frac{dP}{dm}4\pi r^2 + f_P \frac{GM(r)}{r^2} = 0, \tag{2.4}$$

and the radiative temperature gradient in the energy transport equation (in the absence of convection) takes the form

$$\nabla_{\rm rad} = \frac{3}{16\pi acG}\frac{\kappa PL}{MT^4}\frac{f_T}{f_P}, \tag{2.5}$$

where the quantities f_P and f_T have the same definition as in Heger et al. (2000). Consequently, the Eddington luminosity gets modified as:

$$L_{\rm Edd} = \frac{4\pi cGM}{\kappa}\frac{f_P}{f_T} \tag{2.6}$$

However, the Eddington factor,

$$\Gamma = \frac{L_{\rm rad}}{L_{\rm Edd}} = \frac{\nabla}{\nabla_{\rm rad}}\frac{L}{L_{\rm Edd}} = \frac{4a}{3}\frac{T^4\nabla}{P} \tag{2.7}$$

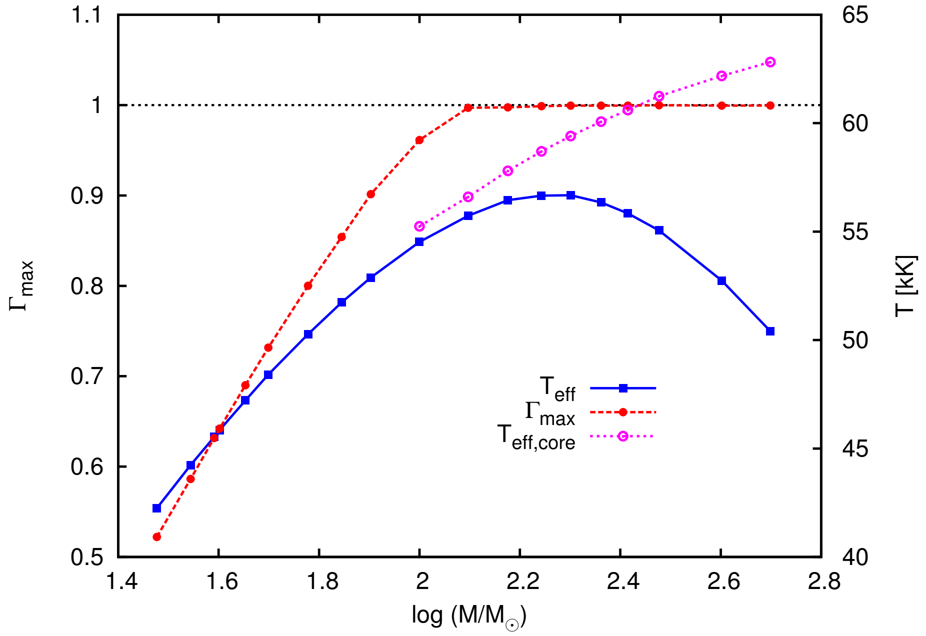

Figure 2.4: Maximum Eddington factor ($\Gamma_{\rm max}$, red line), effective temperature ($T_{\rm eff}$, blue line) and effective temperature at the non-inflated core ($T_{\rm eff,core}$, pink line, see Sect. 2.4, eqn. 2.10) as a function of initial mass for the non-rotating ZAMS models. The black dotted line at $\Gamma_{\rm max} = 1$ is drawn for reference.

does not have any explicit dependence on f_P and f_T because the factor f_P/f_T cancels out. Therefore formally, the Eddington factor remains unaffected by rotation. Of course, if the internal evolution of a rotating model is changed, for example, by rotational mixing, its Eddington factor is still different from that of the corresponding non-rotating model.

Of course, real stars are three-dimensional and the centrifugal force must affect the hydrostatic stability limit. However, this is expected to be a function of the latitude at the stellar surface, and in a 2-D view, the effect is largest at the equator (Langer 1997). To first order, the critical luminosity $L_{\rm c}$ to unbind matter at the stellar equatorial surface becomes

$$L_{\rm c} = L_{\rm Edd}\left(1 - \left(\frac{\upsilon_{\rm rot}}{\upsilon_{\rm Kep}}\right)^2\right), \tag{2.8}$$

where $\upsilon_{\rm rot}$ and $\upsilon_{\rm Kep}$ are the stellar equatorial rotation velocity and the corresponding Keplerian value, respectively. However, to compute the effect reliably, the stellar deformation due to rotation as well as the effect of gravity darkening need to be accounted for (Maeder & Meynet 2000; Maeder 2009). To do this realistically for stars near the Eddington limit requires 2-D calculations at least.

The implication is that the effect of rotation on the critical stellar luminosity cannot be properly described through the models analysed here. Those models see the same critical luminosity as if rotation was absent. Since mixing of helium in these models is very weak for rotation rates below those required for chemically homogeneous evolution, most of the rotating models evolve very similar to the non-rotating models (Brott et al. 2011; Köhler et al. 2015), and thus merely

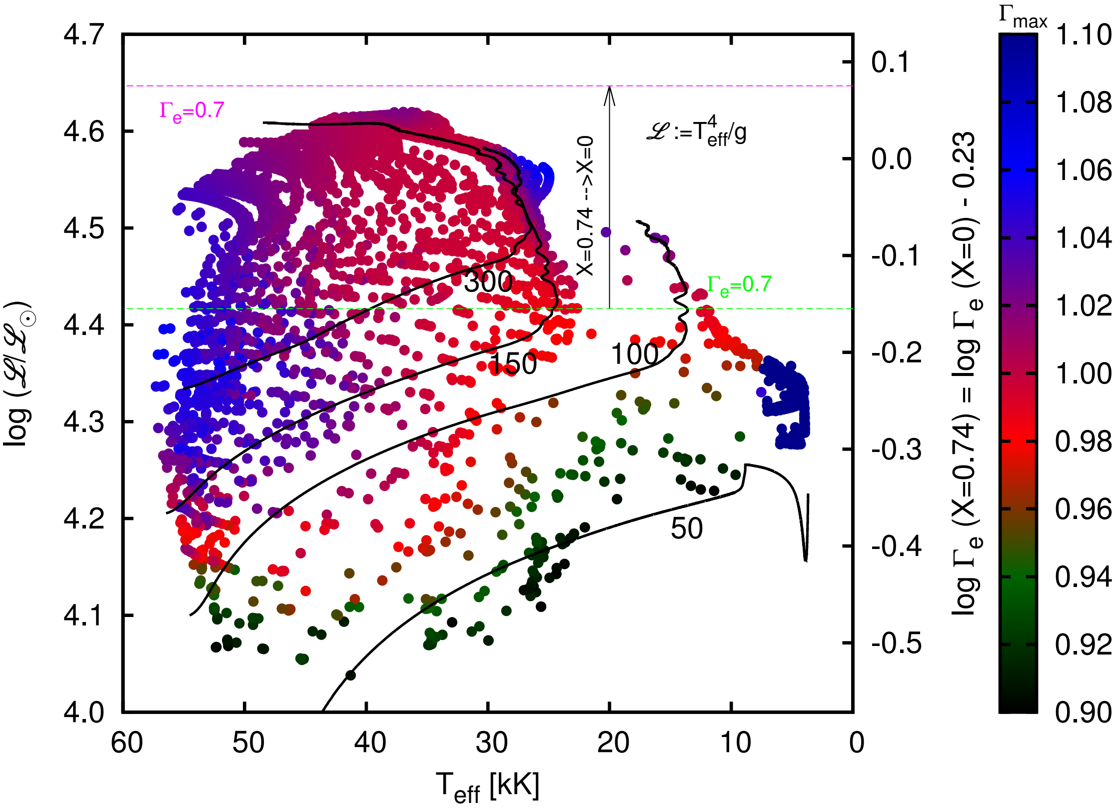

Figure 2.5: Analysed models shown as coloured dots on the spectroscopic HR diagram (sHRD) with the colour representing the value of Γ_{max} in each model. The Eddington factor Γ_e (assuming electron scattering opacity only) is directly proportional to the quantity $\mathscr{L}$ and is indicated on the right Y-axis for a hydrogen mass fraction of $X = 0.74$. Some representative evolutionary tracks of non-rotating models, for different initial masses (indicated along the tracks in units of solar mass), are also shown with solid black lines. The green and blue dotted horizontal lines correspond to $\Gamma_e = 0.7$ for $X = 0.7$ and $X = 0$, respectively. The colour palette and the models marked with yellow diamonds correspond to those in Fig. 2.2. The black dashed line roughly divides the sHRD into distinct regions with $\Gamma_{max} > 1$ and $\Gamma_{max} < 1$.

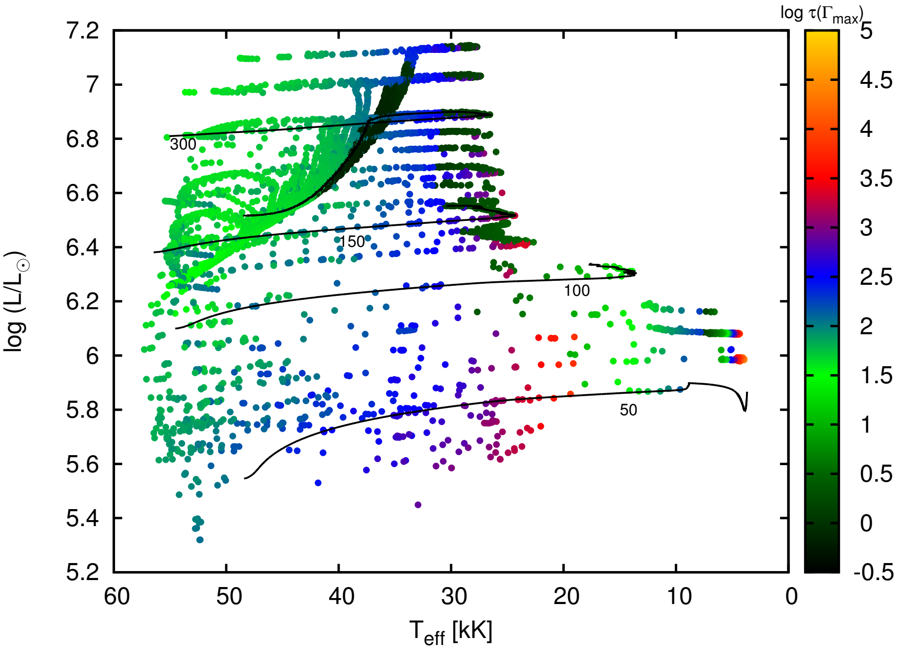

Figure 2.6: Hertzsprung-Russell diagram showing the logarithm of the optical depth τ at the position of $\Gamma_{\max}$ in colour, for all analysed models that have $\Gamma_{\max} > 0.9$. Some representative evolutionary tracks of non-rotating models, for different initial masses (indicated along the tracks in units of solar mass), are also shown with solid black lines.

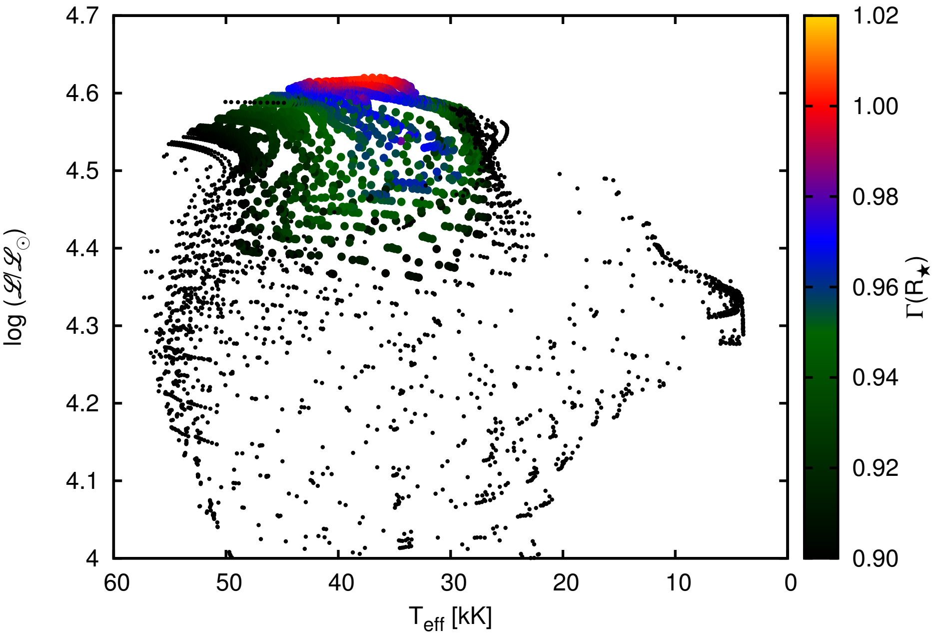

Figure 2.7: The Eddington factors at the stellar surface, $\Gamma(R_\star)$, are shown on the sHRD for our analysed set of models. The models with $\Gamma(R_\star) < 0.9$ are indicated with smaller black circles and those with $\Gamma(R_\star) > 0.9$ are shown as coloured dots.

serve to augment our database.

2.3.2 The maximum Eddington factor

In our stellar models, we have determined the maximum Eddington factor $\Gamma_{\rm max}$ over the whole star, i.e $\Gamma_{\rm max} := \max\,[\Gamma(r)]$. The maximum Eddington factor $\Gamma_{\rm max}$ generally occurs in the outer envelopes of our models, where convective energy transport is much less efficient than in the deep interior. The variation of $\Gamma_{\rm max}$ across the upper HR diagram is shown in Fig. 2.2 for all analysed core hydrogen burning models that have $\Gamma_{\rm max} > 0.9$.

Three distinct regions with $\Gamma_{\rm max} > 1$ can be identified in Fig. 2.2, which can be connected to the opacity peaks of iron, helium, and hydrogen. When one of these opacity peaks is situated sufficiently close to the stellar photosphere, the densities in these layers are so small that convective energy transport becomes inefficient. As a consequence, super-Eddington layers develop that are stabilised by a positive (i.e. inwards directed) gradient in density and gas pressure (see Sect. 2.5 below). The envelope inflation, which occurs when $\Gamma_{\rm max}$ approaches one, is discussed in Sect. 2.4.

Figure 2.3 shows $\Gamma_{\rm max}$ as a function of the effective temperature for all our models with $\Gamma_{\rm max} > 0.9$. The models that have the hydrogen opacity bump close to their photosphere can obtain values of $\Gamma_{\rm max}$ as high as ~ 7. This manifests itself as a prominent peak around $\mathrm{T_{eff}} \approx 5.5\,\mathrm{kK}$. The inset panel shows the much weaker peaks in $\Gamma_{\rm max}$ due to partial ionisation zones of Fe and HeII, at $\mathrm{T/kK} \sim 200$ and 50, respectively. The peak caused by the Fe opacity bump may extend to hotter effective temperatures and apply to hot, hydrogen-free Wolf-Rayet stars, which are not part of our model grid.

For stars above about $125\,\mathrm{M}_\odot$, $\Gamma_{\rm max}$ reaches one, even on the zero-age main-sequence. This is demonstrated in Fig. 2.4 which shows both $\Gamma_{\rm max}$ and effective temperature as a function of mass for the non-rotating stellar models. As these models evolve away from the ZAMS to cooler temperatures, super-Eddington layers develop in their interior. The blue curve shows a maximum effective temperature of 57 000 K at about $200\,\mathrm{M}_\odot$, beyond which it starts decreasing with further increase in mass. This behaviour is related to the phenomenon of inflation, which is discussed in detail in Sect. 2.4. However, the 'effective temperature' at the base of the extended, inflated envelope, $T_{\rm eff,core}$ (see Sect. 2.4), still increases with mass in the whole considered mass range.

2.3.3 The spectroscopic HR diagram

Figure 2.5 shows the location of our analysed models in the spectroscopic HR diagram (sHRD) (Langer & Kudritzki 2014; Köhler et al. 2015) where instead of the luminosity, $\mathscr{L} := T_{\rm eff}^4/g$ is plotted as a function of the effective temperature. The quantity $\mathscr{L}$ can be measured for stars without knowing their distance. Moreover, we have $\log(\mathscr{L}/\mathscr{L}_\odot) = \mathcal{R}$ (cf. Sect. 1), such that $\mathscr{L}$ is directly proportional to the Eddington factor $\Gamma_{\rm e}$ as

$$\Gamma_{\rm e} = \frac{\kappa_{\rm e} L}{4\pi c G M} = \frac{\kappa_{\rm e}\sigma T_{\rm eff}^4}{c g} = \frac{\kappa_{\rm e}\sigma}{c}\mathscr{L}, \tag{2.9}$$

where g is the surface gravity and the constants have their usual meaning. Therefore one can directly read off Γ_e (right Y-axis in Fig. 2.5) from the sHRD. Massive stellar models often evolve with a slowly increasing luminosity over their main-sequence lifetimes. Therefore, where in a conventional HR diagram models with very different $\Gamma_{\max}$ might cluster together (see Fig. 2.2), they separate out nicely in the sHRD since $\mathscr{L} \propto L/M$. The effect of the opacity peaks on the maximum Eddington factor ($\Gamma_{\max}$) at temperatures corresponding to the three partial ionisation zones (Fe, HeII and H) is seen more clearly in the sHRD in Fig. 2.5 compared to the ordinary HR diagram (Fig. 2.2).

We find that for our ZAMS models the electron scattering opacity is $\kappa_e \approx 0.34$, while the true photospheric opacity κ_{ph} is around 0.5. Therefore it is expected that the true Eddington limit ($\Gamma = 1$) is achieved at about $\Gamma_e = 0.7$ for stellar models that retain the initial hydrogen abundance at the photosphere. Therefore in Fig. 2.5 we have drawn two horizontal lines corresponding to $\Gamma_e = 0.7$, one assuming the initial hydrogen mass fraction $X = 0.74$ (green line) and the other assuming $X = 0$ (red line). While models with helium-enriched photospheres exceed the green line comfortably, even the most helium-enriched models (rotating or otherwise) stay below the red line.

From Köhler et al. (2015), we know that models with $\log \mathscr{L}/\mathscr{L}_\odot > 4.4$ are all hydrogen-deficient, either due to mass-loss or rotationally induced mixing, as both processes lead to an increasing L/M-ratio (cf. their fig. 18). Figure 2.5 thus demonstrates that the models that contain super-Eddington layers due to the partial ionisation of helium all have hydrogen deficient envelopes, i.e. they are correspondingly helium-enriched.

Figure 2.5 reveals that the electron scattering Eddington factor Γ_e is not a good proxy for the maximum true Eddington factor ($\Gamma_{\max}$) obtained inside the star. For example, along the horizontal line $\log \mathscr{L}/\mathscr{L}_\odot = 4.3$, corresponding to $\Gamma_e \simeq 0.5$, $\Gamma_{\max}$ varies from well below one to values near seven at the cool end. However, we note that below 30 000 K helium and hydrogen recombine, the gas is not fully ionised any more. The line opacities of helium and hydrogen become important, which causes the increase in $\Gamma_{\max}$ (see Figs. 2.3 and 2.14).

2.3.4 Surface Eddington factors and the location of $\Gamma_{\max}$

The optical depth where $\Gamma_{\max}$f is reached gives an idea of how deep in the stellar interior the layer with the highest Eddington factor is located. We investigate this in Fig. 2.6, which shows that $\Gamma_{\max}$ is located at largely different optical depths in different types of models. While the maximum Eddington factors occur generally at optical depths below $\sim$ 10 000, we see that in the three effective temperature regimes identified by the super-Eddington peaks in Figs. 2.2 and 2.3, $\Gamma_{\max}$ can even be located at an optical depth of $\sim$ 10 or below.

For example, when the tracks above $\log L/L_\odot = 6.2$ approach effective temperatures of $\sim$ 30 kK, $\Gamma_{\max}$ is located at the Fe-peak, which is deep inside the envelope ($\tau \simeq 1400$). The models at this stage become helium-rich ($Y_s \gtrsim 70\%$) and the Wolf-Rayet mass-loss prescription is applied. Once these tracks turn bluewards in the HR diagram, the position of $\Gamma_{\max}$ jumps to the helium opacity peak, which is located much closer to the stellar surface. Consequently, we find three orders of magnitude of difference between these two types of models with similar effective temperature and luminosity.

When considering the surface Eddington factors in the spectroscopic Hertzsprung-Russell

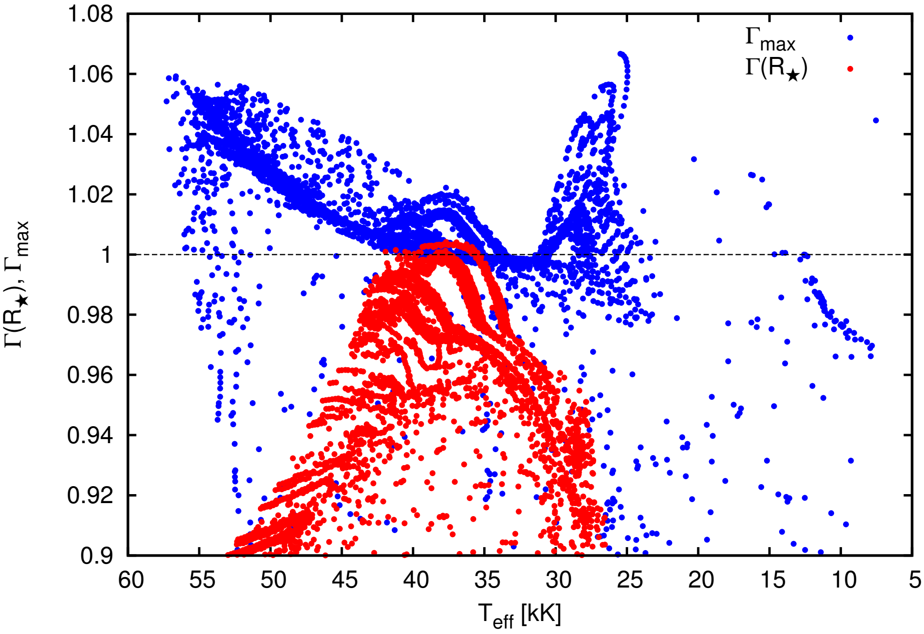

Figure 2.8: Maximum Eddington factor ($\Gamma_{max} > 0.9$) and surface Eddington factor ($\Gamma(R_\star) > 0.9$) as a function of the effective temperature T_{eff} of our analysed models. The black dotted line at $\Gamma = 1$ is drawn for convenience.

diagram (Fig. 2.7), we see that only the models with $\Gamma(R_\star) > 0.98$ have $\log \mathscr{L}/\mathscr{L}_\odot$ values of more than 4.6. As discussed above, these models, which started on the main-sequence with initial masses above 300 $M_\odot$ are extremely helium-rich and may correspond to the most extreme late-type WN stars (Sander et al. 2014). As shown in Fig. 2.8, they exceed the Eddington limit by just a few per mille, which is possible because of the high assumed mass-loss rates that imply a slight deviation from hydrostatic equilibrium near the stellar surface (cf. Sect. 2.3 above). However, these models are those in which our assumption of an optically thin wind might break down (see Fig. 7 in Köhler et al. 2015). Since the inclusion of an optically thick outflow may lead to changes of the temperature and density structure near the surface, the surface Eddington-factors for these particular models are not reliable.

In summary, we find, on the one hand, that many of our models contain layers at optical depths between a few and a few thousand in which the Eddington factor exceeds the critical value of one. On the other hand, for none of our models we can conclude that the Eddington limit is reached very near to, or at the surface, where for the vast majority we can even exclude that this happens. This finding leads to a shift in the expectation of the response of stars that reach the Eddington limit during their evolution. We might not expect direct outflows driven by super-Eddington luminosities, but instead internal structural changes, in particular envelope inflation.

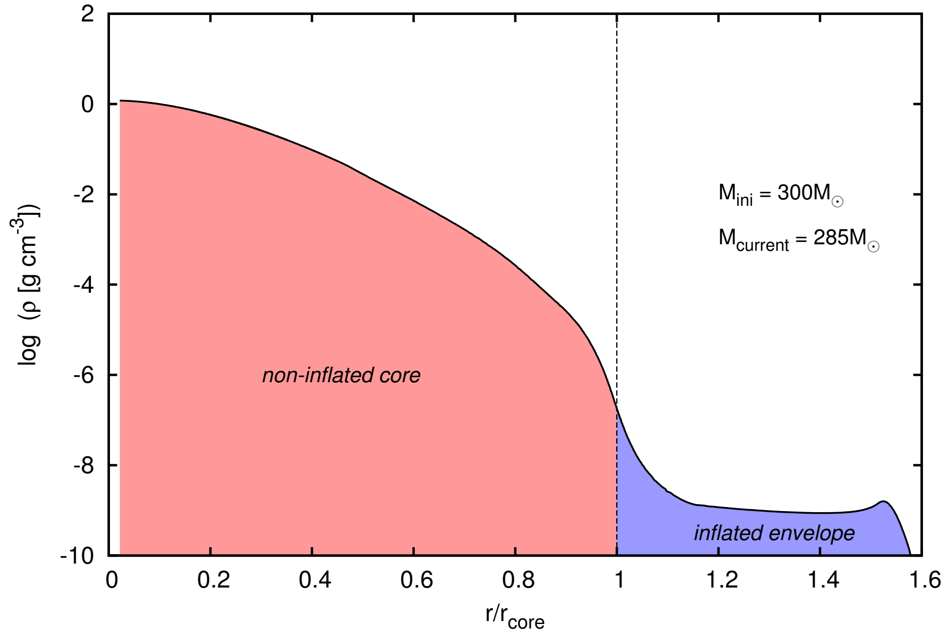

Figure 2.9: Density profile of a non-rotating 285 $M_\odot$ star with $T_{\rm eff}$ = 46600 K and $\log(L/L_\odot)$ = 6.8 (cf. Fig. 2.1 and Sec. 2.10.1) showing an inflated envelope and a density inversion. The X-axis has been scaled with the core radius $r_{\rm core}$ of 25.3 $R_\odot$, as defined in Sect. 2.4.

2.4 Envelope inflation

Inflation of massive, luminous stars refers to the formation of extended, extremely dilute stellar envelopes. An example of an inflated model is shown in Fig. 2.9. The red shaded region is the non-inflated core and the blue shaded region is what we refer to as the inflated envelope. In the example, the model is inflated by 60% of its core radius (defined below). In the presented model, the inflated envelope only contain a small fraction of a solar mass, i.e. $\approx 10^{-5}$ $M_\odot$.

Envelope inflation is inherently different from classical red supergiant formation. The latter occurs after core hydrogen exhaustion, as a consequence of vigorous hydrogen shell burning. This process expands all layers above the shell source, which usually comprise several solar masses in massive stars, and it also operates in low-mass stars, such that no proximity to the Eddington limit is required. The mechanism of envelope inflation that we discuss already works during core hydrogen burning, i.e. even on the zero-age main-sequence for sufficiently luminous stars (cf. Fig. 2.4). Previous investigations have suggested that inflation is related to the proximity of the stellar luminosity to the Eddington luminosity (Ishii et al. 1999; Petrovic et al. 2006; Gräfener et al. 2012) in the envelopes of massive stars with a high luminosity-to-mass ratio ($\gtrsim 10^4$ $L_\odot/M_\odot$). The amount of mass contained in an inflated envelope is usually very small. As we shall see below, inflation, in extreme cases, can also produce core hydrogen burning red supergiants.

We define inflation in our models through $\Delta r/r_{\rm core} := (R_\star - r_{\rm core})/r_{\rm core}$, with $r_{\rm core}$ being the radius at which inflation starts and $R_\star$, the photospheric radius. Since the densities in inflated

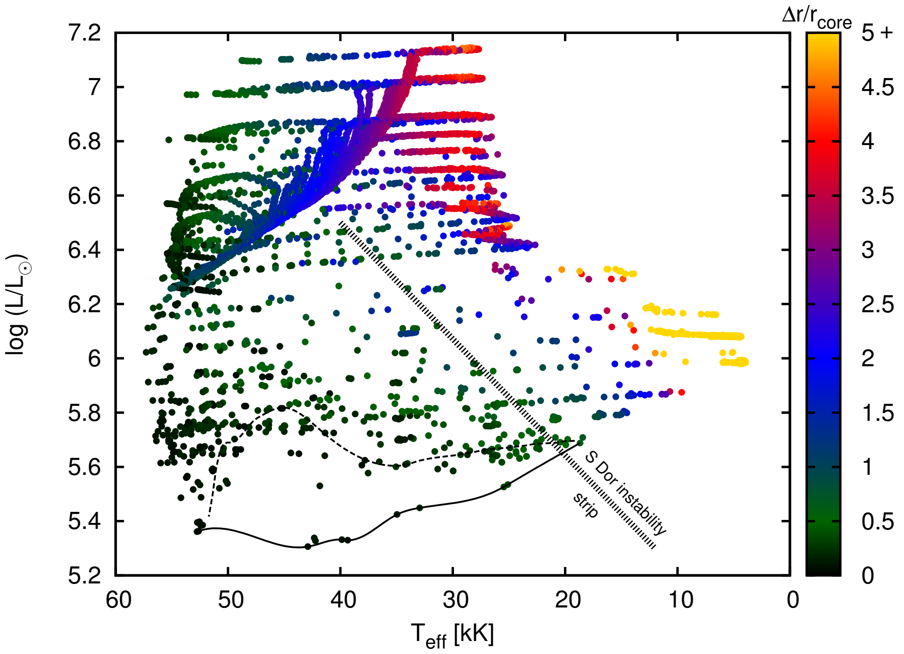

Figure 2.10: Hertzprung-Russell diagram showing all the core-hydrogen burning inflated models, i.e with $\Delta r/r_{\rm core} > 0$. Models with $\Delta r/r_{\rm core} > 5$ are coloured yellow. Below the solid black line we do not find any inflated models and above the dotted black line we do not find any non-inflated models in our grid. The hot part of the S Dor instability strip is also marked (Smith et al. 2004).

envelopes are small, the dominance of radiation pressure in these envelopes is much larger than it is in the main stellar body. We define a model to be inflated if $\beta(r)$, which is the ratio of gas pressure to total pressure, reaches a value below 0.15 in the interior of a model. The radius at which β goes below 0.15 for the first time from the centre outwards is denoted as $r_{\rm core}$, i.e. the start of the inflated region. The remaining extent of the star until the photosphere ($R_\star - r_{\rm core}$) is considered the inflated envelope.

We emphasize that our choice of the threshold value for β is arbitrary and not derivable from first principles. However, we have verified that this prescription identifies inflated stars in different parts of the HR diagram very well (cf. Sec. 2.10.4). As $\beta \to 0$ for $M \to \infty$, our criterion may fail for extreme masses, however, the mass averaged value of β for the most massive zero-age main-sequence model that we analysed (500 M$_\odot$) is 0.3. A threshold value of 0.15 thus appears adequate for the present study. As an example, let us consider a typical inflated model, shown in Sec. 2.10.1. The value of β in Fig. 2.28 decreases sharply at the base of the inflated envelope, to around 0.01. Even if the β threshold is varied by 30%, i.e. 0.15 ± 0.045, the non-inflated core radius $r_{\rm core}$ changes by only 4%. This goes to show that for clearly inflated models, the value of $r_{\rm core}$ is insensitive to the threshold value of β.

We furthermore performed a numerical experiment which is suited to show that the core radii identified as described above are indeed robust. We chose an inflated 300 M$_\odot$ model, and then increased the mixing length parameter α such that convection becomes more and more efficient. As shown in Fig. 2.30, as a result the extent of the inflated envelope decreased without

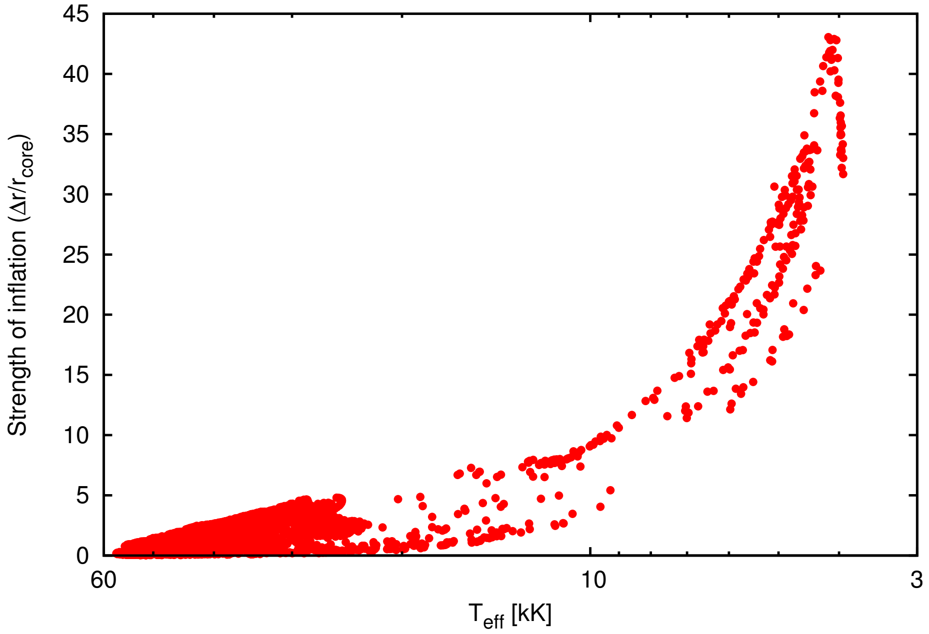

Figure 2.11: Inflation as a function of the effective temperature for all analysed models that fulfill our inflation criterion.

affecting the model structure inside the core radius, which thus remained independent of α. For $\alpha = 40$ convection became nearly adiabatic, inflation almost disappeared, and the fact that the photospheric radius in this case became very close to the core radius validates our method of identifying $r_{\rm core}$.

Figure 2.10 shows the amount of inflation as defined above, for all our models that fulfil the inflation criterion, in the HR diagram. It reveals that overall, inflation is larger for cooler temperatures. This is not surprising since inflation does not appear to change the stellar luminosity and must therefore induce smaller surface temperatures. We also see that inflation is larger for more luminous stars, which is expected because the Eddington limit is supposed to play a role (see below). We also find inflation increases along the evolutionary tracks of the most massive stars that turn back from the blue supergiant stage, which in this case is due to the shrinking of their core radii. A distinction between the inflated and the non-inflated models is made by drawing the black lines in Fig. 2.10. They are drawn such that no model is inflated below the solid line and all the models are inflated above the dotted line. In between these two lines we find a mixture of both inflated and non-inflated models. We find that essentially all models above $\log(L/{\rm L}_\odot) \simeq 5.6$ are inflated. Consequently, stars above $\sim 40\,{\rm M}_\odot$ inflate during their main-sequence evolution.

Figure 2.11 shows the inflation factor as function of the stellar effective temperature for our inflated models. Whereas inflation increases the radius of our hot stars by up to a factor of 5, the cool supergiant models can be inflated by a factor of up to 40. We refer to Sec. 2.10.1 for the detailed structures of several inflated models.

In Fig. 2.12, we take a look at inflation as a function of the core effective temperature $T_{\rm eff,core}$

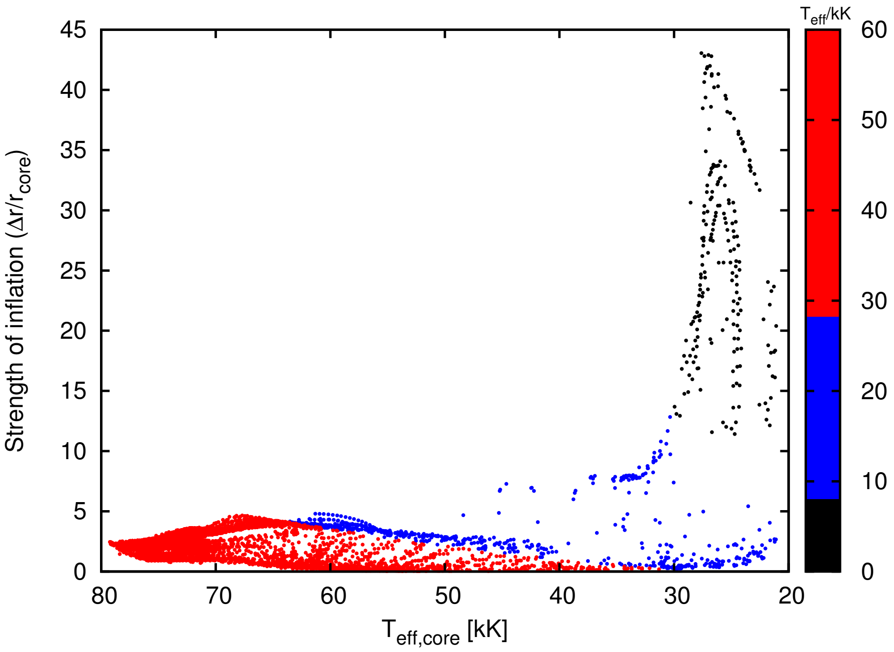

Figure 2.12: Inflation as a function of the effective temperature at the core-envelope boundary for all analysed models with $\Delta r/r_{\mathrm{core}} > 0$. Colour coding indicates the T_{eff} at the photosphere.

defined as

$$T_{\mathrm{eff,core}} = \left(\frac{L}{4\pi\sigma r_{\mathrm{core}}^2}\right)^{\frac{1}{4}}, \tag{2.10}$$

where L refers to the surface luminosity and the constants have their usual meaning. We can see that even our coolest models have high core effective temperatures in the sense that if their inflated envelopes were absent their stellar effective temperatures would have been higher than 20 000 K. Those stars with stellar effective temperatures below ~50 000 K contain the He II ionisation zone within their envelopes, and stars with stellar effective temperatures below ~10 000 K also contain the H/He I ionisation zone. However, as revealed by the density and temperature structure of these models (cf. Sec. 2.10.4), the temperature at the bottom of the inflated envelope is always about 170 000 K, and thus corresponds to the temperature of the iron opacity peak. We conclude that the iron opacity is at least in part driving the inflation of all the stars. For those with cool enough envelopes, helium and hydrogen are likely relevant in addition.

2.4.1 Why do stellar envelopes inflate?

As suggested earlier, the physical cause of inflation in a given star may be its proximity to the Eddington limit. Figure 2.13 shows the correlation between inflation and Γ_{max} for our models. As expected, we find that our stellar models are not inflated when Γ_{max} is significantly below 1, and they are all inflated for $\Gamma_{\mathrm{max}} > 1$. Indeed, the top panel of Fig. 2.13 gives the clear message that the Eddington limit, in the way it is defined in Sect. 2.3, is likely connected with envelope

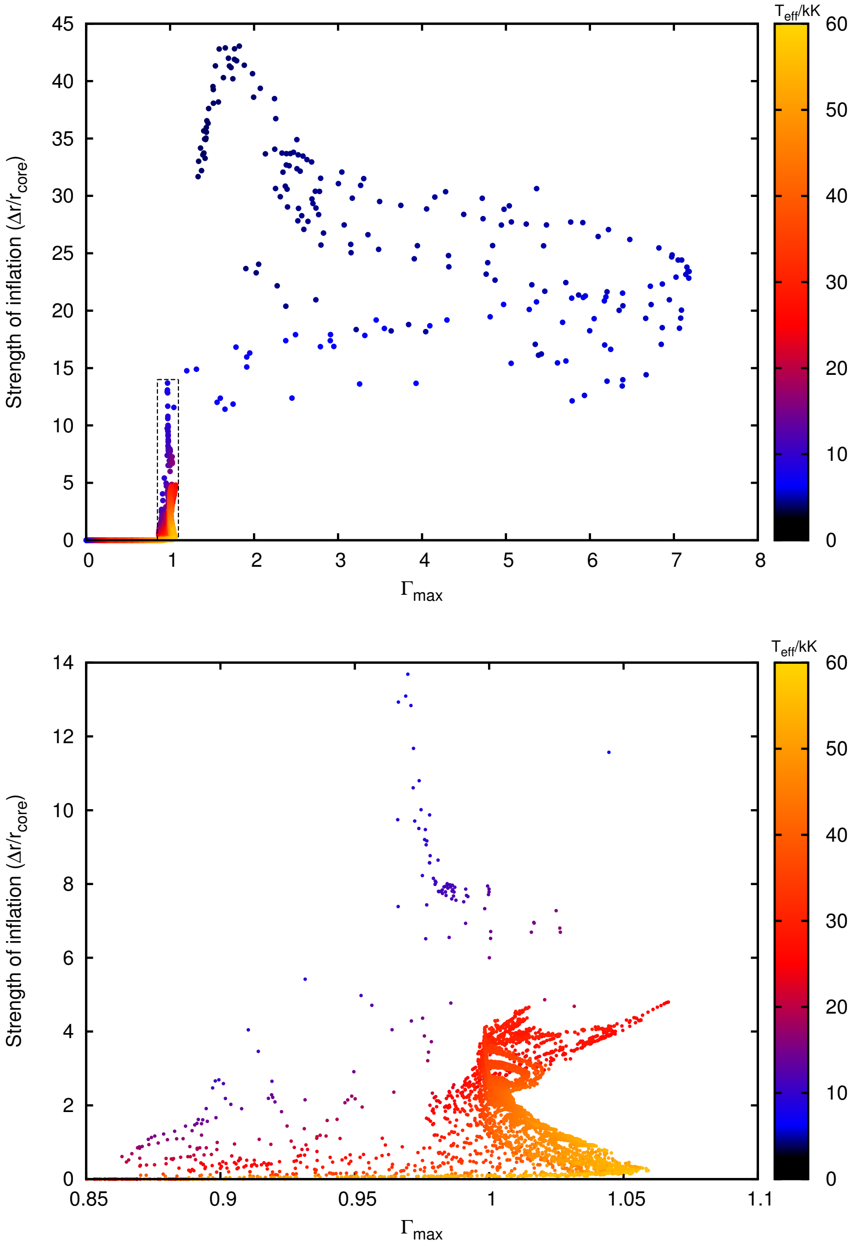

Figure 2.13: *Top:* inflation ($\Delta r/r_{\rm core}$) as a function of $\Gamma_{\rm max}$ for the analysed models. The effective temperature of every model is colour-coded. The area within the black dotted lines is magnified below. *Bottom:* zoomed-in view of the dotted region in the top panel around $\Gamma_{\rm max} = 1$.

inflation.

Comparing Fig. 2.13 (top panel) to Fig. 2.11 shows that inflation increases up to $T_{\rm eff} \approx 5\,500$ K. Thereafter, $T_{\rm eff}$ and $\Gamma_{\rm max}$ decrease and the stars keep getting bigger without significant changes in $r_{\rm core}$, and, hence, inflation still increases. However, the drop in inflation for the coolest models shows an opposite trend. This is because the non-inflated core radius $r_{\rm core}$ now moves outwards (increases) such that inflation ($\Delta r/r_{\rm core}$) decreases even though $R_\star$ keeps increasing (cf. definition of $r_{\rm core}$ in Sec. 2.4).

In the zoom-in view shown in the lower panel of Fig. 2.13, we see some models being inflated for $\Gamma_{\rm max}$ in the range $\sim 0.9 \ldots 1$. Partly, this may be because of the arbitrariness in our definition of inflation. The exact value of $\Delta r/r_{\rm core}$ depends somewhat on the choice of the threshold value of β to characterize inflation (cf. Sec. 2.10.4), i.e. the models with $\Delta r/r_{\rm core} \lesssim 2$ and $\Gamma_{\rm max} < 1$ may be at the borderline of inflation. The models with $\Delta r/r_{\rm core} \lesssim 2$ but $\Gamma_{\rm max} > 1$ are all very hot ($T_{\rm eff} \gtrsim 40\,000$ K) and in those models, the inflation is intrinsically small, but generally unambiguous.

Still, we see a significant number of models below the Eddington limit ($\Gamma_{\rm max} < 1$), which show a quite prominent inflation, i.e. which have a radius increase due to inflation of more than a factor of five. We investigated this kind of a model by artificially increasing its mass-loss rate above the critical value $\dot{M}_{\rm crit}$ (Petrovic et al. 2006), such that the inflated envelope was removed (cf. Sect. 2.4.2). We then found that, on turning down the mass-loss rate to its original value, the model regained its initial inflated structure with $\Gamma_{\rm max} < 1$. However, $\Gamma_{\rm max} = 1$ was reached and exceeded in the course of our experiment. We conclude that a stellar envelope may remain inflated even if the condition $\Gamma_{\rm max} = 1$ is not met any more in the course of evolution, but that $\Gamma_{\rm max} \gtrsim 1$ may be required to obtain inflation in the first place.

In contrast to earlier ideas of a hydrodynamic outflow being triggered when the stellar surface reaches the Eddington limit (Eddington 1926; Owocki et al. 2004), in our models this never happens. When the properly defined Eddington limit is reached inside the envelope, its outermost layers expand hydrostatically and produce inflation. Two possibilities arise in this process. When the star approaches the Eddington limit, the ensuing envelope expansion leads to changes in the temperature and the density structure. Consequently, the envelope opacity can either increase or decrease. Fig. 2.14 shows that the effect of expansion generally leads to a reduced opacity such that the expansion is indeed alleviating the problem. The star then expands until the Eddington limit is just not exceeded any more, which is the reason why we find so many inflated models with $\Gamma_{\rm max} \simeq 1$.

Figure 2.14 shows the OPAL opacities for hydrogen-rich composition for various constant values of R as function of temperature, where $R = \rho/(T/10^6)^3$. Kippenhahn et al. (1990) showed that for constant $\beta = P_{\rm gas}/P$ and constant chemical composition, R as a function of spatial co-ordinate inside the star is a constant. Thus, for un-inflated models, the opacity curves in Fig. 2.14 may closely represent the true run of opacity with temperature inside the star. In the inflated models, β is dropping abruptly at the base of the inflated envelope, which means that the opacity is jumping from a curve with a higher R-value to one with a lower R-value at this location. That is, the opacity is smaller everywhere in the inflated envelope compared to the situation where inflation would not have happened.

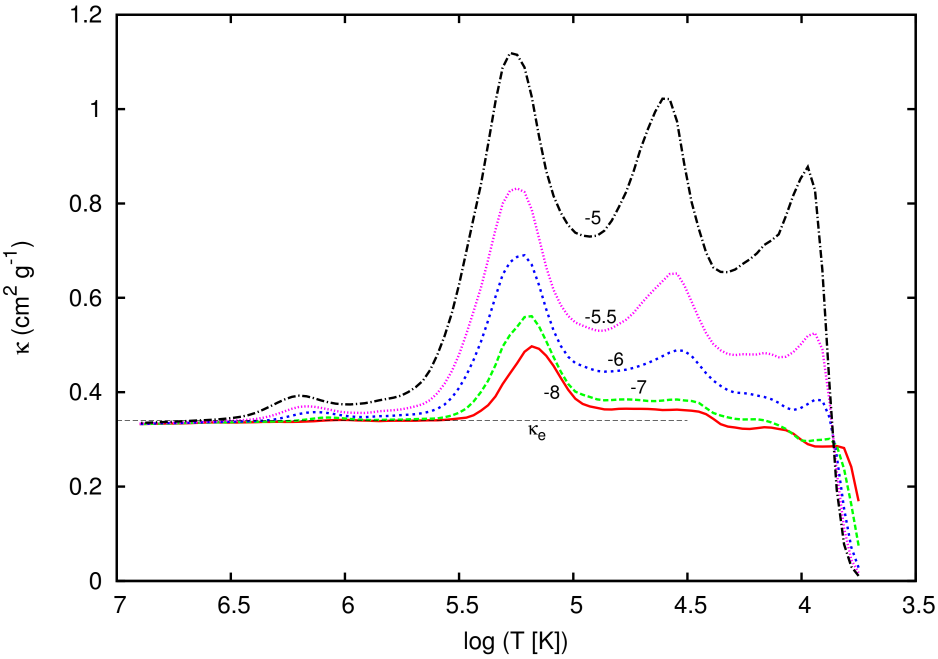

Figure 2.14: Opacity as a function of temperature for fixed values of the opacity parameter R defined as $R = \rho/T_6^3$, where T_6 is the temperature in units of 10^6 Kelvin. The values of $\log R$, which are held constant, are indicated along the curves. The data is taken from the OPAL tables with a composition of X=0.7000, Y=0.2960, Z=0.004 (Iglesias & Rogers 1996). The black horizontal line shows the electron scattering opacity κ_e for a hydrogen mass fraction of $X = 0.7$. At a temperature of 200 000 K, $\log R = -5$ implies a density of $\rho = 8 \times 10^{-8}\,\mathrm{g\,cm^{-3}}$ and $\log R = -8$ implies a density of $\rho = 8 \times 10^{-11}\,\mathrm{g\,cm^{-3}}$.

For the chemical composition given in Fig. 2.14 and assuming $\beta \equiv$ const., we find

$$R \simeq 1.8\,10^{-5}\frac{\beta}{1-\beta}, \tag{2.11}$$

such that if β drops from 0.5 in the bulk of the star to 0.1 in the inflated envelope, R drops by one order of magnitude. The corresponding reduction in opacity can be significant, i.e. up to about a factor of two.

When upon expansion the envelope becomes cool enough for another opacity bump to come into play, the problem of not exceeding the Eddington limit might not be solvable this way. Instead, when a new opacity peak is encountered in the outer part of the envelope, super-Eddington conditions occur, i.e. layers with $\Gamma_{\max} > 1$ (cf. Figs. 2.2 and 2.5), along with a strong positive gas pressure (and density) gradient (cf. Sects. 2.3 and 2.5). This is most extreme when the envelopes become cool enough ($T_{\rm eff} \lesssim 8000\,\mathrm{K}$) such that the hydrogen ionisation zone is present in the outer part of the envelope, where Eddington factors of up to seven are achieved.

2.4.2 Influence of mass-loss on inflation

One might wonder about the sustainability of the inflated layers against mass-loss, which is an important factor in the evolution of metal-rich massive stars. Petrovic et al. (2006) estimated that the inflated envelope cannot be replenished when the mass-loss rate exceeds a critical value of

$$\dot{M}_{\rm crit} = 4\pi r_{\rm core}^2 \rho_{\rm min} \sqrt{\frac{GM}{r_{\rm core}}} \,, \tag{2.12}$$

where M and $r_{\rm core}$ stand for the stellar mass and the un-inflated radius, respectively, and $\rho_{\rm min}$ is the minimum density in the inflated region. Petrovic et al. (2006) found $\dot{M}_{\rm crit} \sim 10^{-5}\,{\rm M}_\odot\,{\rm yr}^{-1}$ for a massive hydrogen-free Wolf-Rayet star of $24\,{\rm M}_\odot$. However, for a typical inflated massive star on the main-sequence (see Fig. 2.25), this critical mass-loss rate is of the order $10^{-3}\ldots 10^{-1}\,{\rm M}_\odot\,{\rm yr}^{-1}$. These high mass-loss rates are only expected in LBV-type giant eruptions. The mass-loss rates applied to our models are several orders of magnitude smaller (cf. Köhler et al. 2015).

The mass-loss history of four evolutionary sequences without rotation are shown in Fig. 2.15. Even the $500\,{\rm M}_\odot$ model never exceeds a mass-loss rate $\sim 5\times 10^{-4}\,{\rm M}_\odot\,{\rm yr}^{-1}$. The critical mass-loss rate for all models shown in Fig. 2.15 is much higher than the actual mass-loss rates applied. Whereas $\dot{M}_{\rm crit}$ typically exceeds $\dot{M}$ by a factor of 1000 for the inflated models in the $50\,{\rm M}_\odot$ sequence, it exceeds that of the $500\,{\rm M}_\odot$ sequence by a factor of $3\ldots 100$. It is thus not expected that mass-loss prevents the formation of the inflated envelopes in massive stars near the Eddington limit. In fact, it may be difficult to identify a source of momentum that might drive such strong mass-loss (Shaviv 2001; Owocki et al. 2004). Gräfener et al. (2011) in the Milky Way and Bestenlehner et al. (2014) in the LMC found a steep dependence of the mass-loss rates on the electron-scattering Eddington factor $\Gamma_{\rm e}$ for very massive stars, but they do not find mass-loss rates that substantially exceed $10^{-4}\,{\rm M}_\odot\,{\rm yr}^{-1}$.

As many of the models analysed here may be pulsationally unstable, the mass-loss rates may be enhanced in this case. Grott et al. (2005) show that hot stars near the Eddington limit may undergo mass-loss due to pulsations, although extreme mass-loss rates are not predicted. For very massive cool stars, on the other hand, Moriya & Langer (2015) find that pulsations may enhance the mass-loss rate to values of the order of $10^{-2}\,{\rm M}_\odot\,{\rm yr}^{-1}$. These extreme values could prevent the corresponding stars to spend a long time on the cool side of the Humphreys-Davidson limit. A detailed consideration of this issue is beyond the scope of the present paper.

2.5 Density inversions

An inflated envelope can be associated with a ‘density inversion’ near the stellar surface, i.e. a region where the density increases outwards. An example is shown in Fig. 2.9. In hydrostatic equilibrium, $\Gamma(r) > 1$ implies $\frac{dP_{\rm gas}}{dr} > 0$, and thus $\frac{d\rho}{dr} > 0$. As a consequence, all the models that have layers in their envelopes exceeding the Eddington limit show density inversions. The criterion for density inversion can be expressed as (Joss et al. 1973; Paxton et al. 2013)

$$\frac{L_{\rm rad}}{L_{\rm Edd}} > \left[1 + \left(\frac{\partial P_{\rm gas}}{\partial P_{\rm rad}}\right)_\rho\right]^{-1} , \tag{2.13}$$

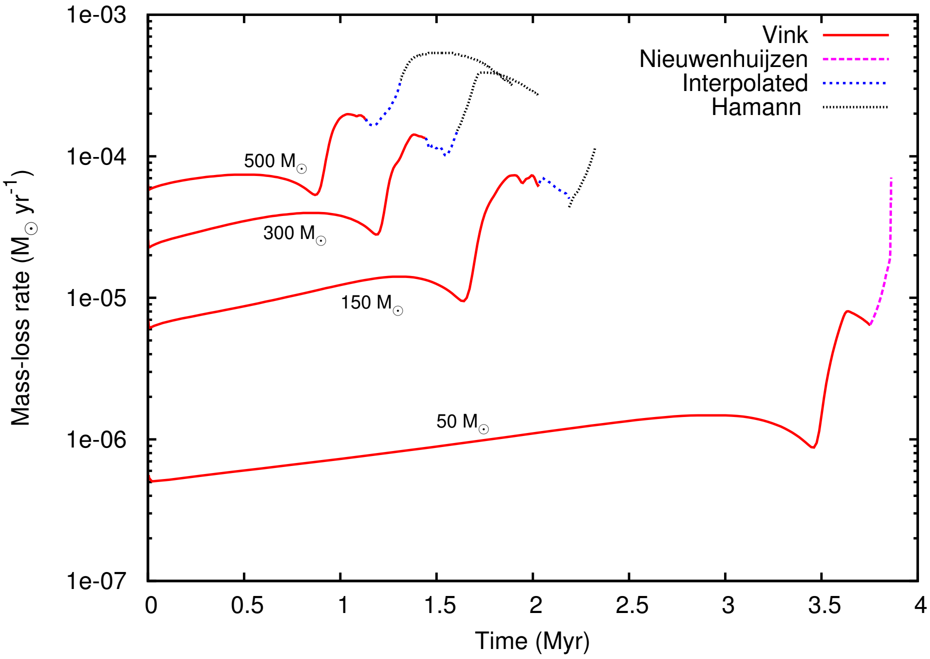

Figure 2.15: Mass-loss history of four non-rotating evolutionary sequences from our grid. The initial masses are given along each evolutionary track. The colours indicate the different mass-loss prescriptions that were used in different phases, as described in Sect. 2.

where P_{gas}, P_{rad} and ρ stand for the gas pressure, radiation pressure, and density, respectively. A density inversion gives an inwards force and acts as a stabilizing agent for the inflated envelopes. In the above inequality, P_{gas} is assumed to be a function of ρ and T only, i.e. the mean molecular weight μ is assumed to be constant. Density inversions might also be present in low-mass stars like the Sun where they are caused by the steep increase of μ around the hydrogen recombination zone (cf. Érgma 1971).

Figure 2.16 identifies our core hydrogen burning models, which contain a density inversion. The quantity $\Delta\rho/\rho$ represents the strength of the density inversion normalized to the minimum density attained in the inflated zone. We can identify three peaks in $\Delta\rho/\rho$ at $T_{\mathrm{eff}}/\mathrm{kK} \sim 55$, 25, and 5.5 (see also Fig. 2.17), which coincides exactly with the three T_{eff}-regimes in which models exceed the Eddington limit (cf. Fig. 2.3). The maximum of the density inversions in the three zones is related to the relative prominence of the three opacity bumps of Fe, HeII, and H respectively, as shown in Fig. 2.17.

However, an inflated model is not necessarily accompanied by a density inversion. This is depicted clearly in Fig. 2.18 where we investigate the correlation between inflation and density inversion (this can also be seen by comparing Fig. 2.10 to Fig. 2.16). Figure 2.18 shows many models that are even substantially inflated but do not develop a density inversion. The three peaks in the distribution of density inversions of Fig. 2.17 also show up distinctly in this plot at the three characteristic effective temperatures (shown in colour). Models that show a density inversion do always show some inflation. This is less obvious from Fig. 2.18 because the hottest models show the smallest amount of inflation (Fig. 2.11).

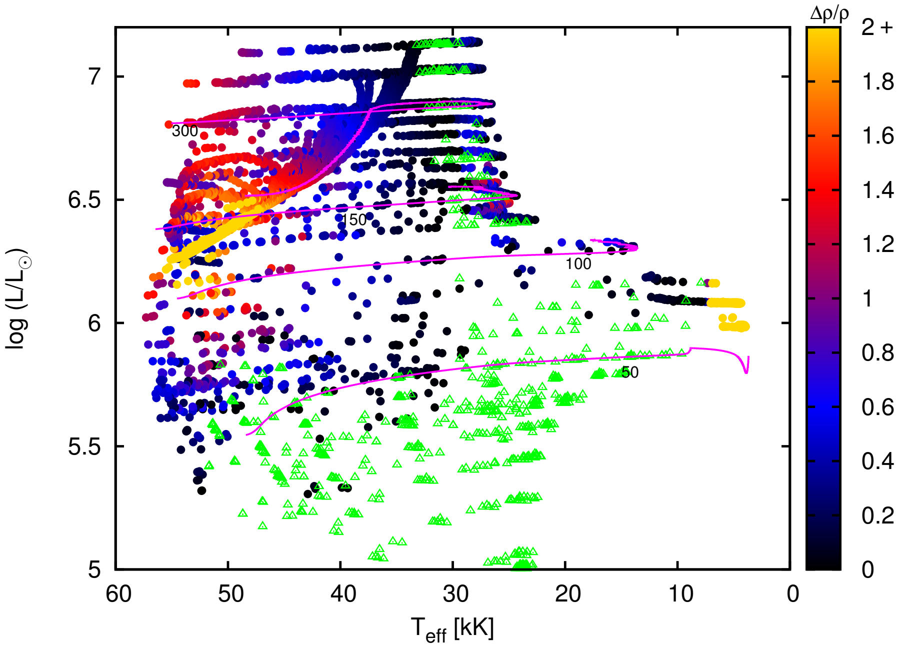

Figure 2.16: Upper HR diagram showing all main-sequence models with density inversions. Models with $\Delta\rho/\rho > 2$ have been coloured yellow. The models without density inversion are indicated with open green triangles. Some representative evolutionary tracks of non-rotating models, for different initial masses (indicated along the tracks in units of solar mass), are also shown with solid coloured lines.

The stability of density inversions in stellar envelopes has been a matter of debate for the last few decades but there has been no consensus on this issue yet (see Maeder 1992). There have been early speculations by Mihalas (1969) while studying red supergiants that a density inversion might lead to Rayleigh-Taylor instabilities (RTI), resulting in "elephant trunk" structures washing out the positive density gradient. However, as rightly pointed out by Schaerer (1996), RTI does not develop since the effective gravity $g_{\rm eff} = g(1 - \Gamma)$ acting on the fluid elements is directed outwards in the super-Eddington layers, which contain the density inversion. Kutter (1970), on the other hand, claimed that a hydrodynamic treatment of the stellar structure equations prevents any density inversion and instead leads to a steady mass outflow. However, this claim is refuted by the present work, since our code solves the 1-D hydrodynamic stellar structure equations, in agreement with previous hydrodynamical models by Glatzel & Kiriakidis (1993a) and Meynet (1992). Stothers & Chin (1973) suggested that density inversions will lead to strong turbulent motions instead of drastic mass-loss episodes. However, these layers are unstable to convection, so turbulence is present in any case.

Additionally, Glatzel & Kiriakidis (1993a) argued in favour of a sustainability of density inversions in the sense that they can be viewed as a natural consequence of strongly non-adiabatic convection, and pointed out that the only plausible way to suppress density inversions is to use a different theory of convection. The only instability expected from simple arguments therefore is convection, which is in line with Wentzel (1970) and Langer (1997).

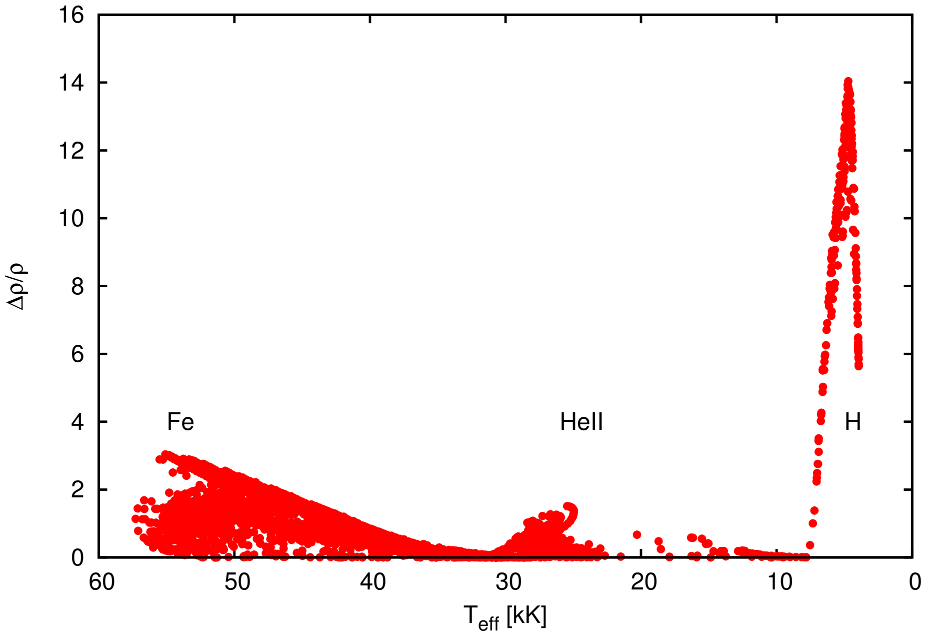

Figure 2.17: The extent of density inversions ($\Delta\rho/\rho$) as a function of $T_{\rm eff}$ for our models. The three peaks correspond to the three opacity bumps of Fe, HeII, and H in the OPAL tables, as indicated.

Still, Ekström et al. (2012) and Yusof et al. (2013) recently considered density inversions as 'unphysical'. Density inversions have been suppressed in their models by replacing the pressure scale height in the Mixing Length Theory with the density scale height (cf. Sect. 2.7). This approach has often been adopted by many investigators in the past to prevent numerical difficulties. As the density scale height tends to infinity when a density inversion starts to develop, this measure tends to enormously increase the convective flux in the relevant layers. It is doubtful whether in reality the convective flux can be increased so much, as the ratio of the local thermal to the local dynamical timescale in the relevant layers is much smaller than one, such that convective eddies lose their thermal energy much faster than they rise, and thus hardly transport any energy at all. Multi-dimensional hydrodynamical simulations would help to settle this issue. We briefly return to this point in Sect. 2.7.

2.6 Sub-surface convection

We also studied the convective velocities in the sub-surface convection zones associated with the opacity peaks in our stellar models (Cantiello et al. 2009). We measure these velocities in units of either the isothermal or the adiabatic sound velocity, i.e. $c_{\rm s,ad}$ and $c_{\rm s,iso}$, respectively, which we compute as

$$c_{\rm s,ad} = \sqrt{\frac{\gamma P}{\rho}} \qquad (2.14)$$

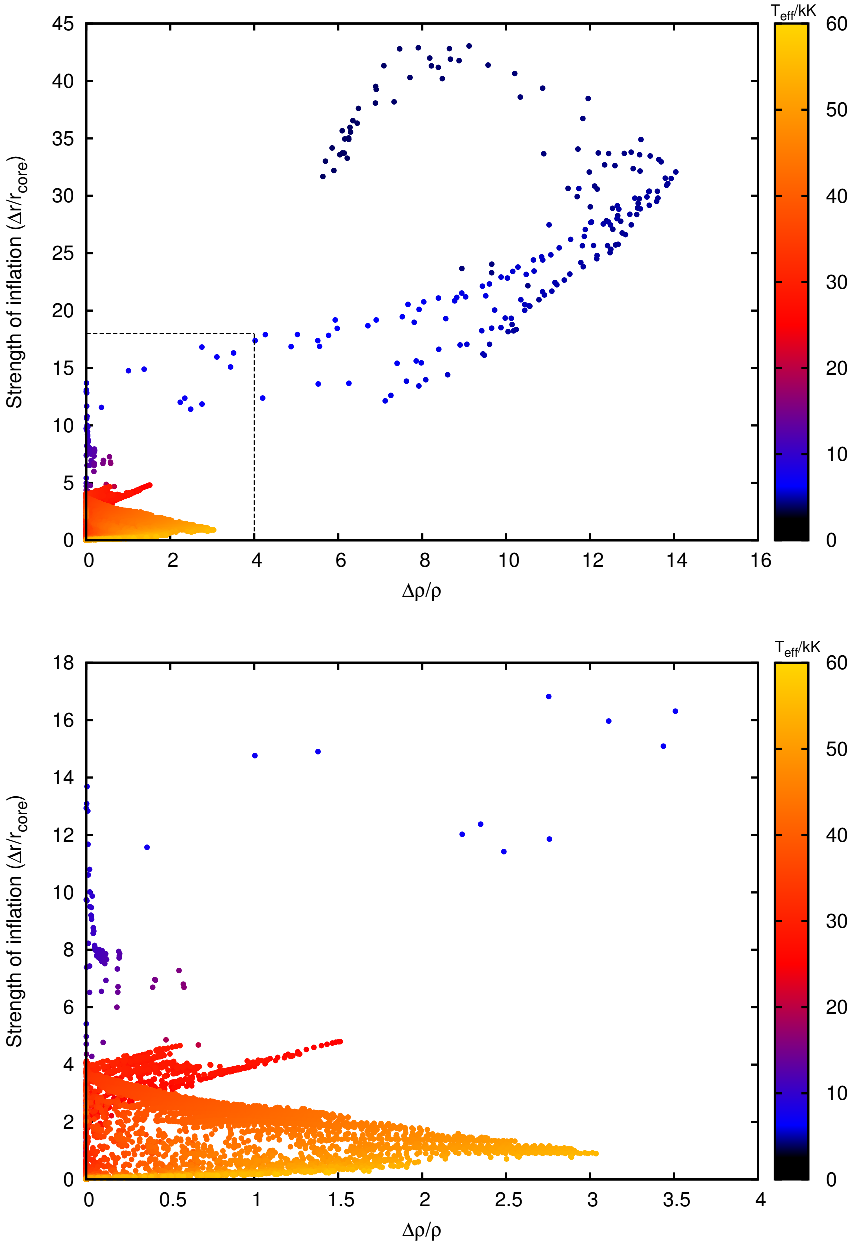

Figure 2.18: *Top:* correlation between inflation and density inversions for our models with $\log L/L_\odot > 5$. *Bottom:* zoomed-in view of the area within the back dotted lines in the top panel.

and

$$c_{\rm s,iso} = \sqrt{\frac{k_B T}{\mu}} = \sqrt{\frac{P_{\rm gas}}{\rho}}, \tag{2.15}$$

where γ is the adiabatic index, P is the total pressure, ρ is the density, μ is the mean molecular weight, T is the temperature, and k_B is the Boltzmann constant. We define $M_{\rm iso}$ as the maximum ratio of the convective velocity over the isothermal sound speed in the stellar envelope, and $M_{\rm ad}$ correspondingly using the adiabatic sound speed.

The true sound speed is in between the adiabatic and isothermal speed, closer to the first one in the inner parts of the star, and closer to the second in the inflated stellar envelope (cf. Sect. 5). In Figs. 2.19 and 2.20, we show the values of $\mathrm{M}_{\rm iso}$ and $M_{\rm ad}$ for our models in the HR diagram. Whereas the convective velocities are always smaller than the adiabatic sound speed, Fig. 2.19 shows that the isothermal sound speed can be exceeded locally in our models by a factor of a few. The convective velocity and sound speed profiles for an extreme model are presented in Sec. 2.10.3.

Supersonic convective velocities (adiabatic or isothermal, depending on the physical conditions in the envelope) may not be realistic and are outside the frame of the standard Mixing Length Theory. Therefore, in some of our models, the convective velocities, and thus the convective energy transport, may have been overestimated. A limitation of the velocities to the adequate sound speed is expected to reduce the convective flux, which might lead to further inflation of the stellar envelope.

The cool models, with the strongest inflation, have relatively smaller values of $M_{\rm iso}$ (compared to the hot WR-type models) but large values of $M_{\rm ad}$ (Fig. 2.20) in the sub-surface convection zones. This is primarily because of the fact that while $c_{\rm s,ad}$ depends on the total pressure, $c_{\rm s,iso}$ only depends on the gas pressure. In the very outer layers of the cool, luminous models, $\beta \rightarrow 1$ and hence $P_{\rm gas} \approx P_{\rm tot}$. In these situations, $c_{\rm s,ad}$ and $c_{\rm s,iso}$ are only a factor $\sqrt{\gamma}$ apart, where γ is the adiabatic index.

We find that the convective energy transport is not always negligible in the inflated models (cf. Sec 2.4.1). We therefore evaluate the amount of flux that is actually carried by convection in the inflated envelopes of our models. We define the quantity $\eta(M_{\rm iso})$ as the fraction of the total flux carried by convection in the stellar envelope, at the location where the isothermal Mach number is the largest. This quantity is plotted as a function of the effective temperature in Fig. 2.21. It is evident from this figure that $\eta(M_{\rm iso})$ need not be small for stellar envelopes to be inflated. However, the hotter a model is the lower its $\eta(M_{\rm iso})$-value at a given luminosity (see Fig. 2.22). For models hotter than $T_{\rm eff} \approx 63$ kK (e.g. the hydrogen-free He stars), $\eta(M_{\rm iso})$ indeed goes towards zero (Grassitelli et al., in preparation). The behaviour of the quantity $\eta(M_{\rm iso})$ in the HR diagram is shown in Fig. 2.22.

2.7 Comparison with previous studies

2.7.1 Stellar atmosphere and wind models

Since the Eddington limit was thought to be reached in massive stars near their surface (cf. Sect. 2.3), several papers have investigated this using stellar atmosphere calculations. Lamers &

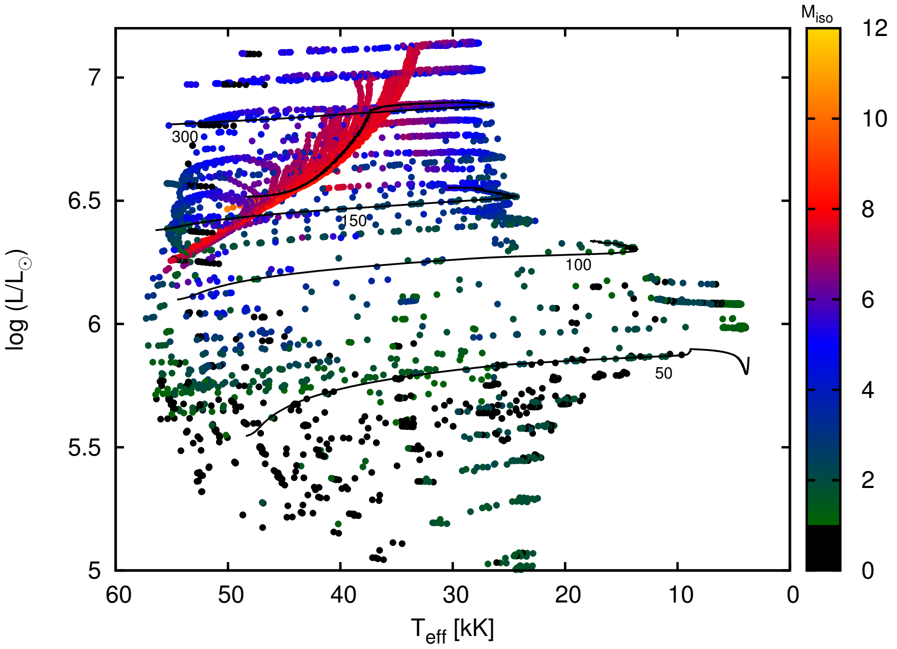

Figure 2.19: Upper HR diagram ($\log L/L_\odot > 5$) showing the maximum of the ratio of the convective velocity to the local isothermal sound speed ($M_{\rm iso}$) of the analysed models as coloured dots. Models with $M_{\rm iso} < 1$ are shown in black. Some representative evolutionary tracks of non-rotating models, for different initial masses (indicated along the tracks in units of solar mass), are also shown with solid black lines.

Fitzpatrick (1988) investigated the Eddington factors in the atmospheres of luminous stars in the temperature-gravity diagram, while Ulmer & Fitzpatrick (1998) did so in the HR diagram. Both studies took the full radiative opacity into account. While their technique did not allow them to reach Eddington factors of one or more, Ulmer and Fitzpatrick found that model atmospheres with a maximum Eddington factor of 0.9 are located near the observed upper luminosity limit of stars in the Large Magellanic Cloud (Humphreys & Davidson 1979; Fitzpatrick & Garmany 1990).

The main feature in the lines of constant Eddington factors in the HR diagram found by Ulmer and Fitzpatrick is a drop from $T_{\rm eff} \simeq 60\,000$ K to 15 000 K. This may correspond to the drop in the maximum Eddington factor seen in our models in the same temperature interval (cf. Figs. 2.2 and 2.5). Note that the peak around $T_{\rm eff} \simeq 30\,000$ K in Fig. 2.3 only corresponds to helium-rich models, which are not considered by Ulmer and Fitzpatrick.

On the other hand, neither inflation nor super-Eddington layers or density inversions are reported by Ulmer and Fitzpatrick, or, to the best of our knowledge, from any hot, main-sequence star model atmosphere calculation so far. One reason might be that many model atmospheres only include a rather limited optical depth range (e.g. up to $\tau = 100$ in Ulmer and Fitzpatrick), such that the iron opacity peak is often not included in the model. Additionally, the computational methods employed might not allow for a non-monotonic density profile.

Given the ubiquity of inflation for models above $\log L/{\rm L}_\odot > 5.5$ or $M > 50\,{\rm M}_\odot$ in the LMC,

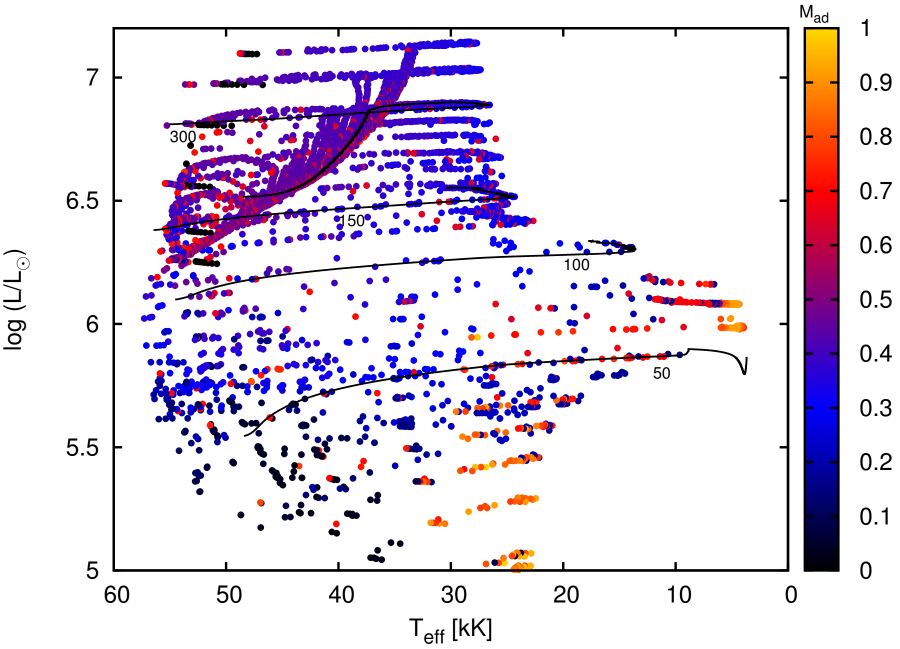

Figure 2.20: Upper HR diagram ($\log L/L_{\odot} > 5$) showing the maximum of the ratio of the convective velocity to the local adiabatic sound speed $M_{\rm ad}$ of the analysed models (computed with an adiabatic index of 5/3) as coloured dots. Some representative evolutionary tracks of non-rotating models, for different initial masses (indicated along the tracks in units of solar mass), are also shown with solid black lines.

and a correspondingly lower limit in the Milky Way due to its higher iron content, it is helpful to construct model atmospheres that include this effect and identify its observational signatures. As the density profiles of these kinds of atmospheres near the photosphere are significantly different from those in non-inflated atmospheres, these signatures may indeed be expected.

Asplund (1998) gives a thorough analysis of the Eddington limit in cool star atmosphere models. Indeed, he finds super-Eddington layers and density inversions in his models, and gives arguments for the physically appropriate nature of these phenomena. He also discusses the effects of stellar winds on these features, and finds they may be suppressed by extremely strong winds, but not by winds with mass-loss rates in the observed range. Asplund does not find inflation in his models, again, arguably because the iron opacity peak is not included in his model atmospheres, which appears essential even for our models with cool effective temperatures.

Owocki et al. (2004) and van Marle et al. (2008) studied the winds of stars that reach or exceed the Eddington limit at their surface. As we have shown above, this condition is generally not found in our models (cf. Figs. 2.7 and 2.8). However, it may occur in helium-rich stars (see again Fig. 2.7) and hydrogen-free Wolf-Rayet stars (cf. Heger & Langer 1996), as well as in stars that deviate from thermal or hydrostatic equilibrium. Noticeably, Owocki et al. (2004) find that the mass-loss rates in this case are still quite limited, because of the energy loss attributed to lifting the wind material out of the gravitational potential (see, Heger & Langer 1996).

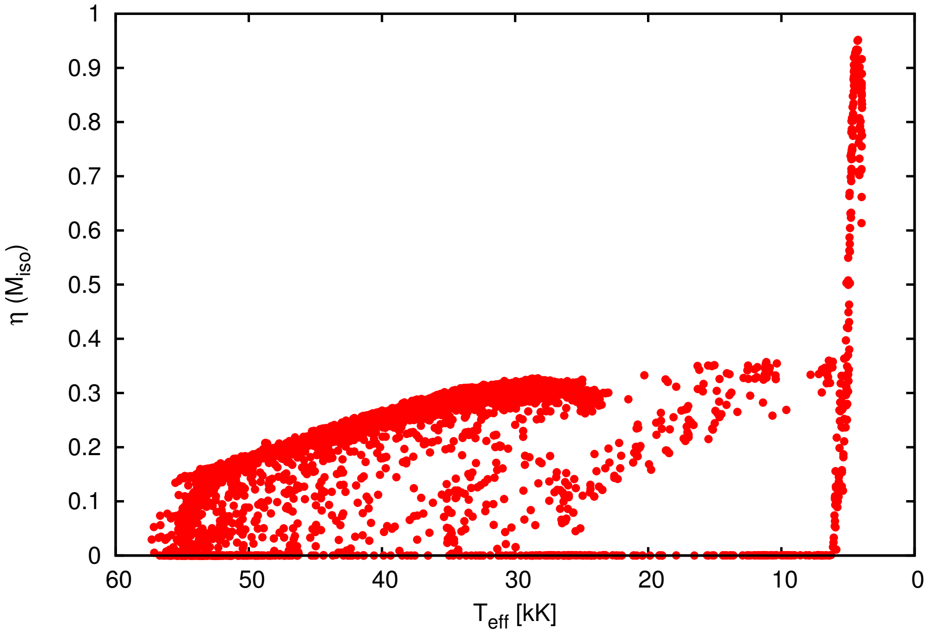

Figure 2.21: Convective efficiency $\eta(M_{\rm iso})$, which is the ratio of the convective flux to the total flux at the position where the isothermal Mach number is the largest in the stellar envelope, as a function of the effective temperature for all analysed stellar models in our grid.

We want to emphasize in this context that the Eddington limit investigated in the quoted models as well as in our own may be different from the true Eddington limit, because of a number of effects that are all related to the opacity of the stellar matter in the stellar envelopes. One is that convection, which is necessarily present in the layers near or above the Eddington limit, may induce density inhomogeneities or clumping that can alter the effective radiative opacity (Shaviv 1998). In fact, depending on the nature of the clumping, the opacity may be enhanced (Gräfener et al. 2012) or reduced (Owocki et al. 2004; Ruszkowski & Begelman 2003; Muijres et al. 2011). Furthermore, such opacity calculations are tedious, and even in the currently used opacities, important contributions might still be missing.

Finally, the effect of stellar rotation on the stability limit in the atmospheres especially of hot stars is clearly important (Langer 1997, 1998; Maeder & Meynet 2000). However, it adds another dimension to this difficult problem and is therefore generally not included (cf. Sect. 2.7.2).

2.7.2 Stellar interior models

The peculiar core-halo density structure of inflated stars was first pointed out by Stothers & Chin (1993), after Iglesias et al. (1992) found the large iron bump in the opacities near 170 000 K. Further studies pointing out this phenomenon comprise Ishii et al. (1999), Petrovic et al. (2006), Gräfener et al. (2012), and Köhler et al. (2015). Conceivably, inflation may be present in further models of very massive stars, but often no statements on the presence or absence of this

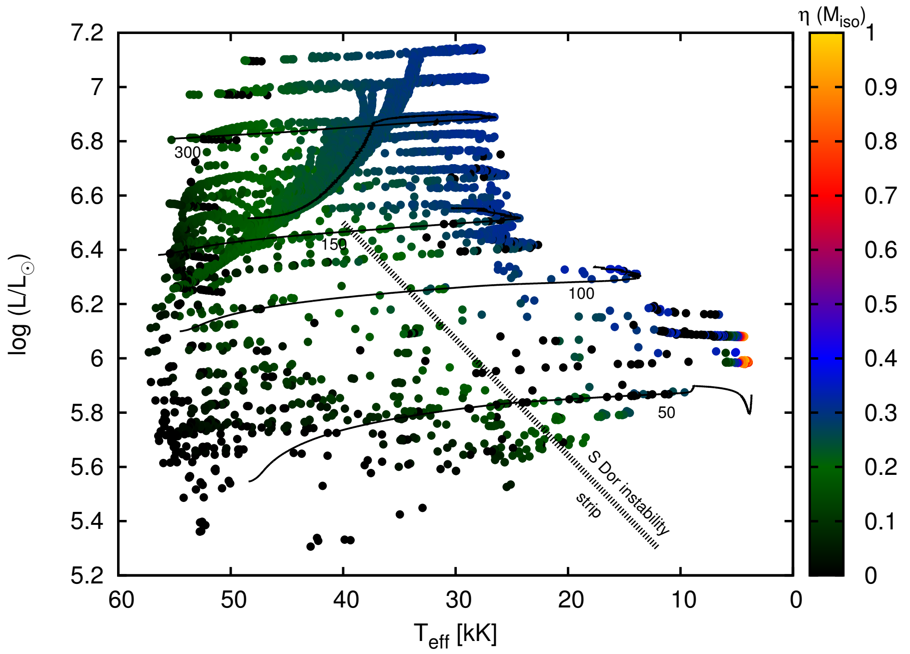

Figure 2.22: Upper HR diagram showing all the inflated stellar models in our grid as coloured dots. The convective efficiency $\eta(M_{\rm iso})$, which is the ratio of the convective flux to the total flux at the position where the isothermal Mach number is the largest in the stellar envelope, is colour coded. Some representative evolutionary tracks of non-rotating models, for different initial masses (indicated along the tracks in units of solar mass), are also shown with solid black lines.

phenomenon are made in these papers.

For example, the models for very massive stars by Yusof et al. (2013) only discuss the electron-scattering Eddington factor in their models. On the ZAMS, their models are hotter and more compact than those of Köhler et al. (2015) analysed here, which implies that inflation is either weaker or absent. This difference might be due to the different treatment of convection in the sub-surface convective zones, where Yusof et al. (2013) assume the mixing length to be proportional to the density scale height instead of the standard pressure scale height. This prohibits the formation of density inversions, and since the density scale height tends to infinity when a model attempts to establish a density inversion, the convection may transport an arbitrarily large energy flux in this scheme. While the physics of convection introduces one of the biggest uncertainties in the atmospheres of stars close to the Eddington limit, efficient convective energy transport in inflated envelopes appears unlikely (cf. Sect. 2.5).

A suppression of inflation may have significant consequences for the evolution of massive stars, as the stellar models stay bluer and as a result have lower mass-loss rates and lower spin-down rates. The final fates of these non-inflated stars is significantly different compared to inflated stars (see Köhler et al. 2015, for a detailed discussion).

Gräfener et al. (2012) find inflation which, for their models without clumping, correspond well to those of Petrovic et al. (2006) for the Wolf-Rayet case, and to our unpublished solar metallicity main-sequence models, which show a bending of the zero-age main-sequence to cool temperatures for $M \gtrsim 100\,\mathrm{M}_\odot$. The models of Ishii et al. (1999) also agree very well. Including the work of Stothers & Chin (1993), we conclude that the effect of inflation in models of massive main-sequence stars is found in at least four independent stellar structure codes, with three of them quantitatively producing very similar results.

As pointed out above, massive star evolutionary models, which include effects of rotation, are being produced routinely these days (cf. Maeder & Meynet 2010; Langer 2012; Chieffi & Limongi 2013), but an investigation of the effect of stellar rotation on the stability limit in the atmospheres of hot stars requires the construction of two-dimensional stellar models.

2.8 Comparison with observations

2.8.1 The VFTS sample

A prime motivation of Köhler et al. (2015) for computing the evolutionary models for the very massive stars analysed here was to provide a theoretical framework for the VLT Flames-Tarantula Survey (VFTS, Evans et al. 2011). Within VFTS, multi-epoch spectral data of about 700 early B and 300 O stars are being analysed through detailed model atmosphere calculations. Within this effort, Bestenlehner et al. (2014) and McEvoy et al. (2015) derived the physical properties of more than 50 very massive stars, with luminosities $\log(L/\mathrm{L}_\odot) > 5.5$. We confront the models of Köhler et al. (2015) with this sample in Fig. 2.23.

Two sets of model data are included in Fig. 2.23, one that uses the effective temperatures of the Köhler et al. models directly, and a second one where the effective core temperature is used as defined in Sect. 2.4 (cf. Eq. 2.10). The latter approximates the surface temperature of our models if inflation was completely absent. An example calculation presented in Sec. 2.10.2, where inflation in a $300\,\mathrm{M}_\odot$ is suppressed by increasing the mixing length parameter, shows that this approximation is indeed quite good. The zero-age main-sequence is also drawn for both sets of models. Note that while wind effects are clearly seen in the spectra of all stars in the sample, the optical depth of their winds is expected not to exceed $\tau = 2$ (cf. Fig. 7 in Köhler et al. 2015) until the stars become very helium rich at their surface. Therefore, the effective temperatures derived from the observations need not be corrected for optically thick winds.

As shown in Bestenlehner et al. (2014), the hottest stars in their sample follow the ZAMS of the Köhler et al. models very closely, well into the regime of inflation. One might expect un-evolved stars to the left of the Köhler et al. ZAMS if inflation was not present. In that case, the stars above $\log L/L_\odot \simeq 6.2$ might spend a significant fraction of their lifetime on the hot side of the Köhler et al. ZAMS. The absence of these hot stars, however, does not conclusively argue that inflation does exist in nature, i.e. even without inflation, the star formation history in 30 Doradus might preclude the existence of stars like this, or they may be hidden in their natal cloud because of their youth (Yorke 1986; Castro et al. 2014).

On the cool side, Fig. 2.23 shows an absence of observed stars for $\log L/L_\odot \gtrsim 6.15$ and $T_\mathrm{eff} \lesssim 35\,000\,\mathrm{K}$. As the evolutionary models predict about 30% of the core hydrogen burning to take place at $T_\mathrm{eff} \lesssim 35\,000\,\mathrm{K}$ in this luminosity regime, which may indicate that the inflation in the models of Köhler et al. is too strong. On the other hand, again, the absence of correspondingly cool stars 30 Doradus may be a result of the local star formation history.

In the luminosity range below, at $5.5 \lesssim \log L/L_{\odot} \lesssim 6.15$, stars as cool as $T_{\rm eff} \lesssim 15\,000$ K are observed for which McEvoy et al. (2015) concluded that they are still core hydrogen burning objects. The observed stars are somewhat cooler than the coolest core effective temperature of our models, which may argue in favour of inflation in real stars. Note that the life time of stars in the regime $T_{\rm eff} < 20\,000$ K is only 10% for the Köhler et al. models in the considered luminosity range.

In summary, as the stellar evolution models for these high masses are still quite uncertain, we do not find possible to argue for or against inflation being present in the observed stars considered here based on Fig. 2.23. In fact, it is intriguing that most of the observed stars are found in the regime where the inflated and non-inflated models overlap. Nevertheless, the observed sample above $\log L/\mathrm{L}_{\odot} \simeq 5.5$ might constitute the best test case, since according to our models, the envelopes of all of them are expected to be strongly affected by the Eddington limit. Model atmosphere calculations for these stars, which include inflation, might shed new light on this question.

2.8.2 Further possible consequences of inflation

S Doradus type variability

Gräfener et al. (2012) argue that the S Doradus type variability of LBVs may be related to the effect of inflation, and, in particular, focussed on the case of AG Car (Groh et al. 2009). They propose that an instability sets in when their $70\,\mathrm{M}_{\odot}$ chemically homogeneous hydrostatic stellar model is highly inflated ($\approx 120\,\mathrm{R}_{\odot}$) by virtue of which the inflated layer becomes gravitationally unbound and a mass-loss episode follows.

In contrast to this idea, our inflated hydrodynamic stellar models do not show any signs of this kind of instability. This could be because of various simplifying assumptions made in the models of Gräfener et al. (2012), in particular, their neglect of the convective flux in the inflated envelopes (cf. Sect.2.6). Nevertheless, the physics of convection is very complex in these envelopes, and our results do not necessarily imply that instabilities do not occur.

In fact, considering the hot edge of the S Doradus variability strip, according to Smith et al. (2004), Fig. 2.22 shows that it roughly separates the models with a low maximum convective efficiency ($\eta_{\rm max} < 0.2$) from those with a higher convective efficiency. If these high fluxes could not be achieved in these envelopes (cf. Sect. 2.6), a dynamical instability might well be possible.

The hot edge of the S Doradus variability in the HR diagram also coincides quite well with the borderline separating mildly ($\Delta r/r_{\rm core} < 1$) from strongly ($\Delta r/r_{\rm core} > 1$) inflated models. Comparing this with the observed distribution of very massive stars in Fig. 2.23, which indicates that essentially no stars are found far to the cool side of this line, could indicate again that strongly inflated envelopes are indeed unstable and might lead to S Doradus type variability and an increased time-averaged mass-loss rate.

LBV eruptions

Glatzel & Kiriakidis (1993a) speculated that strange mode pulsations might be responsible for the LBV phenomenon. These pulsations are characterized by very short growth times ($\sim \tau_{\rm dyn}$)

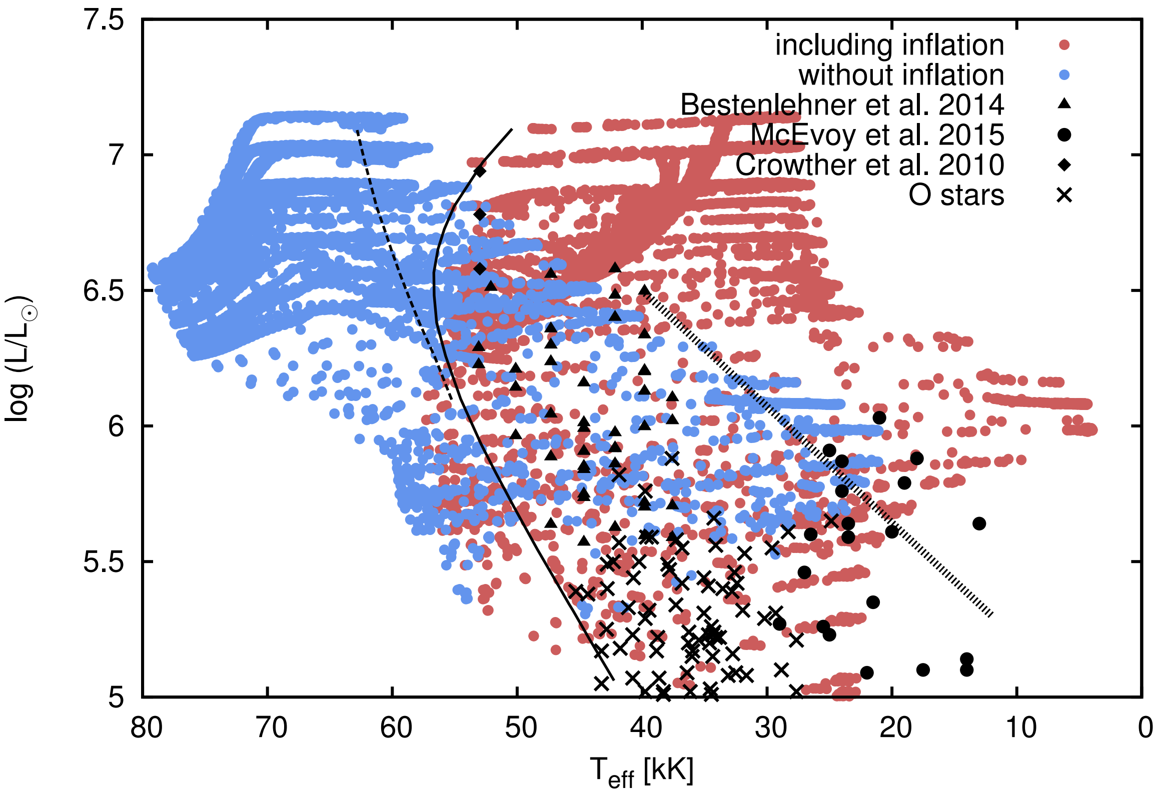

Figure 2.23: Hertzsprung-Russell diagram showing the Köhler et al. (2015) models, which include inflation (red) and corresponding non-inflated stellar models (blue) above $\log L/L_\odot > 5$ (see text for explanation). The triangles refer to all the Of/WN and WNh single stars studied by Bestenlehner et al. (2014) whereas the black dots and diamonds refer to the B-supergiants (single) from McEvoy et al. (2015) and WN5h stars of the core R136 from Crowther et al. (2010), respectively. The O stars observed within the VFTS survey are marked with crosses (Sabín-Sanjulián et al. 2014, Ramirez-Agudelo et al. in preparation). The zero-age main-sequence of the non-rotating stars is marked with the solid line, while the dashed line indicates the approximate position of the zero-age main sequence if inflation was absent (see text for further details). The hot part of the S Doradus instability strip from Smith et al. (2004) is also shown for reference.

and small brightness fluctuations roughly of the order $\sim 10 \ldots 100$ mmag (Glatzel et al. 1999; Grott et al. 2005). However, the mass contained in the pulsating envelopes of their models is negligible compared to the stellar mass, and the associated brightness variations cannot explain the humongous luminosity variations observed in LBV eruptions.

We have seen in Sect. 2.5 that an inflated envelope often produces a density inversion. These density inversions have been repeatedly proposed as a source of instabilities giving rise to eruptive mass-loss in LBVs (Maeder 1989; Maeder & Conti 1994; Stothers & Chin 1993). Given our results, we consider it unlikely that a density inversion can be the sole cause of LBV eruptions. Density inversions are a generic feature present in a multitude of our models (see Fig. 2.16), while the LBV phenomenon is quite rare. Furthermore, the density inversions in our models are found very close to the surface of the star with very small amounts of mass above the inversion.

Given our results, inflation per se appears unlikely to cause LBV eruptions, again, because it occurs too abundantly in our models, and also because the mass of the inflated envelope is generally very small. However, Fig. 2.24 reveals that this is not so for our coolest models. Whereas for most models the mass of the inflated envelope is smaller than $\sim 10^{-3}\,\mathrm{M}_\odot$, intriguingly it rises to several solar masses in the models that have effective temperatures below $\sim 10\,000$ K. These cool models, of which detailed examples are presented in Fig. 2.34, also show the highest Eddington factors (Fig. 2.3) and the strongest inflation (Fig. 2.11). This behaviour is seen in the mass range of $40 \ldots 100\,\mathrm{M}_\odot$, which corresponds well to the masses of observed LBVs.

A key feature in our cool models with massive inflated envelopes is visible in Fig. 2.21. As the opacity in the hydrogen recombination zone becomes very large, effectively blocking any radiation transport, convective efficiencies of the order of $\eta \simeq 1$ are needed to transport the stellar luminosity through this zone. Also, in the iron convection zone at the bottom of the envelope, a high convective efficiency ($\eta \simeq 0.5$) is found in these models. As shown in Figs. 2.19 and 2.20, this requires sonic or even supersonic convective velocities in the framework of the standard MLT as implemented in our code. It thus appears conceivable that in reality convection is less efficient in this kind of a situation, e.g. because of viscous dissipation. When a star enters this region with a massive inflated envelope, throughout which the stellar luminosity can neither be transported by radiation nor by convection, hydrostatic equilibrium is possible any more, and the loosely bound inflated envelope may by dynamically ejected. We believe that this scenario may relate to major LBV eruptions.

As proposed by Langer (2012), a rapid evolutionary timescale of a star may be required to obtain LBV outbursts in addition to the star reaching the Eddington limit. If evolution on the thermal timescale is rapid enough, this might produce LBVs after core hydrogen exhaustion. This rapid evolution may relate to most of the observed LBVs in our Galaxy and the Magellanic Clouds, as well as LBVs after core helium exhaustion, which may address the recently accumulated evidence of LBV outbursts in immediate supernova progenitors (Smith & Arnett 2014).

Supernova shock break-out

A recent study by Moriya et al. (2015) concluded that inflated stellar models can help to explain the extended rise time of the shock break-out signal from the Type Ib supernova SN2008D

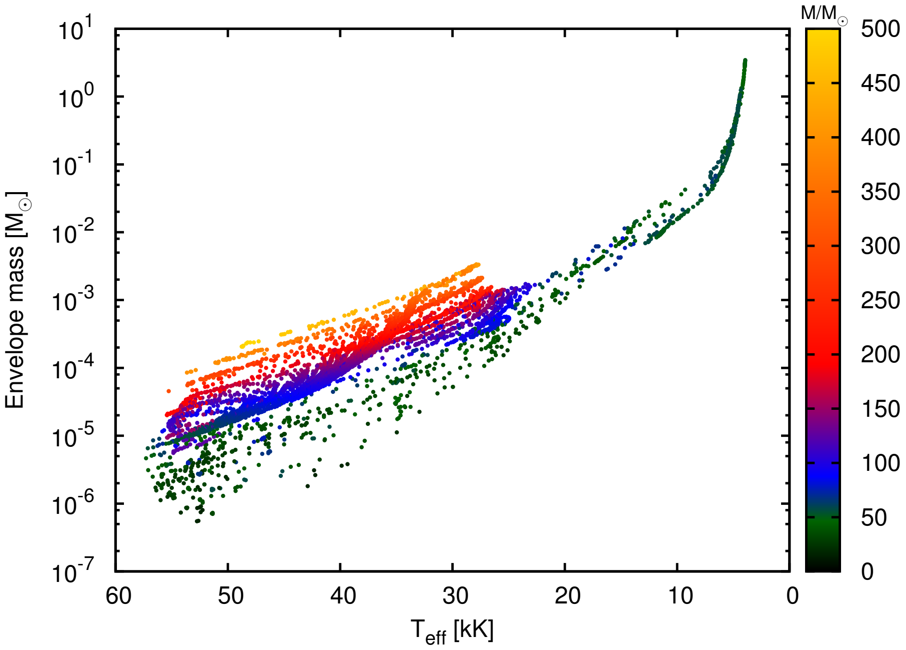

Figure 2.24: Mass contained in the inflated envelope for all inflated models of our grid, as a function of the effective temperature. The effective actual mass of the models is colour-coded (see colour bar to the right).

(Soderberg et al. 2008). In this scenario, the shock break-out occurs deep inside the inflated envelope and consequently the rise time is determined by the radiative diffusion time of the envelope and not the light crossing time. They also noted that more of these kinds of events, if observed in the future, might serve as indicators of inflated supernova progenitors.

Whereas the above result supports the idea that hydrogen-free Wolf-Rayet stars may possess inflated envelopes (Petrovic et al. 2006; Gräfener et al. 2012), LBVs have also been considered to be immediate progenitors of supernovae (Kotak & Vink 2006; Groh et al. 2013). In the realm of high cadence supernova surveys, this opens up the possibility to also test the existence of envelope inflation in hydrogen-rich stars through supernova shock break-out observations.

2.9 Discussion and conclusions

We investigated the internal structures of the massive star models computed by Brott et al. (2011) and Köhler et al. (2015) using a 1-D hydrodynamical stellar evolution code, with particular emphasis on the Eddington limit. We find that the conventional idea of sufficiently massive stars reaching the Eddington limit at the stellar surface is not reproduced by our core hydrogen burning models, not even at 500 M$_\odot$ (cf. Figs. 2.7 and 2.8). Instead, we find a suitably defined Eddington limit inside the star (Eqn. 2.3) is reached by models with $\log(L/L_\odot) \gtrsim 5.6$ (Fig. 2.2), which leads to sub-surface convection, envelope inflation (Fig. 2.13), and possibly to pulsations. Many of our models even exceed this Eddington limit, and in the extreme case of red supergiants even by factors of up to seven (Fig. 2.3), with the consequence that strong density inversions develop such that hydrostatic equilibrium is maintained (Fig. 2.17).

In the analysed models, whose initial composition is chosen to match that of the LMC, all stars above $\sim 40\,\mathrm{M}_\odot$ reach the Eddington limit in their envelopes. As iron opacities are mainly responsible for this phenomenon, we expect that this mass limit is higher at a lower metallicity, and similarly lower for massive stars in our galaxy. Furthermore, there may be two groups of stars for which this limit comes down even further. First, the centrifugal force in rapidly rotating stars may lead to similar conditions in the envelope layers near the stellar equator, i.e. to a strong latitude dependence of inflation. Perhaps, this could give rise to the so-called B[e] supergiants, which show a slow and dense equatorial wind and a fast polar wind at the same time (Zickgraf et al. 1985). Second, the mass losing stars in interacting close binary systems evolve to much higher L/M-values than corresponding single stars (Langer & Kudritzki 2014), and are therefore expected to reach the Eddington limit for much lower initial masses.

The stability of the inflated envelopes is not investigated here, but many of them are likely to be pulsationally unstable (Glatzel & Kiriakidis 1993a; Saio et al. 1998, Sanyal et al. in preparation). If so, it is expected that the pulsations will lead to mass-loss enhancements (e.g. Moriya & Langer 2015), or to the loss of the inflated envelope. In the latter case, the envelope is expected to re-grow unless the achieved time average mass-loss rate exceeds the high critical mass-loss rate (Sect. 2.4.2). We find that in our coolest models, the mass contained in the inflated envelopes can reach several solar masses (Fig. 2.24), and speculate that their dynamical loss may resemble LBV major eruptions (cf. Sect. 2.8.2). Consequently, even though reaching or exceeding the Eddington limit may not immediately lead to strong outflows in stars, clearly the mass-loss rate of the stars is strongly affected, in the sense that the mass-loss is significantly enhanced one way or another.

It will be crucial to test observationally whether luminous, main-sequence stars indeed possess inflated stellar envelopes. This possibility has not yet been investigated with stellar atmosphere models for hot stars. Perhaps the best candidates are the S Doradus variables (Gräfener et al. 2012), which appear in the part of the HR diagram where our models predict a radius inflation by more than a factor of two (cf. Fig. 2.10).

Finally, we note that besides massive stars, the Eddington limit is relevant to various other types of stars, as luminous post-AGB star, X-ray bursts, Novae, R Corona Borealis stars, and accreting compact objects. It may be interesting to assess to what extent similar phenomena as found in this work might play a role in these objects.

2.10 Supplementary material

2.10.1 Interior structure of a $85\,\mathrm{M}_\odot$ stellar model

2.10.2 Effect of efficient convection on inflation

Knowing that convective flux is proportional to the mixing length, we show here (Fig. 2.30) that by increasing the mixing length parameter α in an inflated $300\,\mathrm{M}_\odot$ model near the ZAMS, the inflation gradually goes away and what we are left with is an almost non-inflated star, whose radius is well-approximated by core radius r_core of the inflated model.

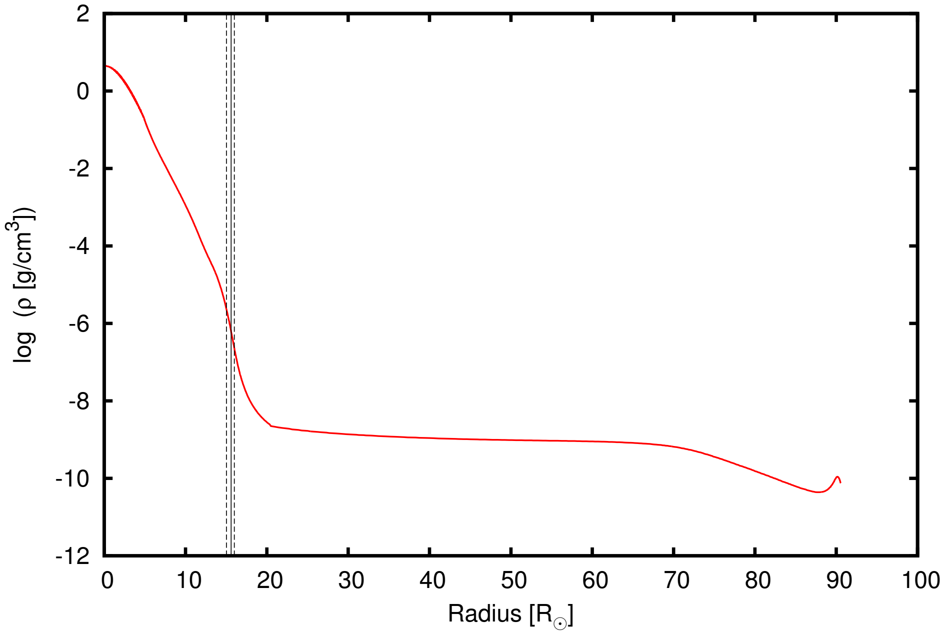

Figure 2.25: Density structure of the stellar model. The black solid line marks the base of the inflated envelope, i.e. where $\beta = 0.15$. The intersection of the dotted lines with the red line on either side mark the points where $\beta = 0.15 \pm 0.045$.

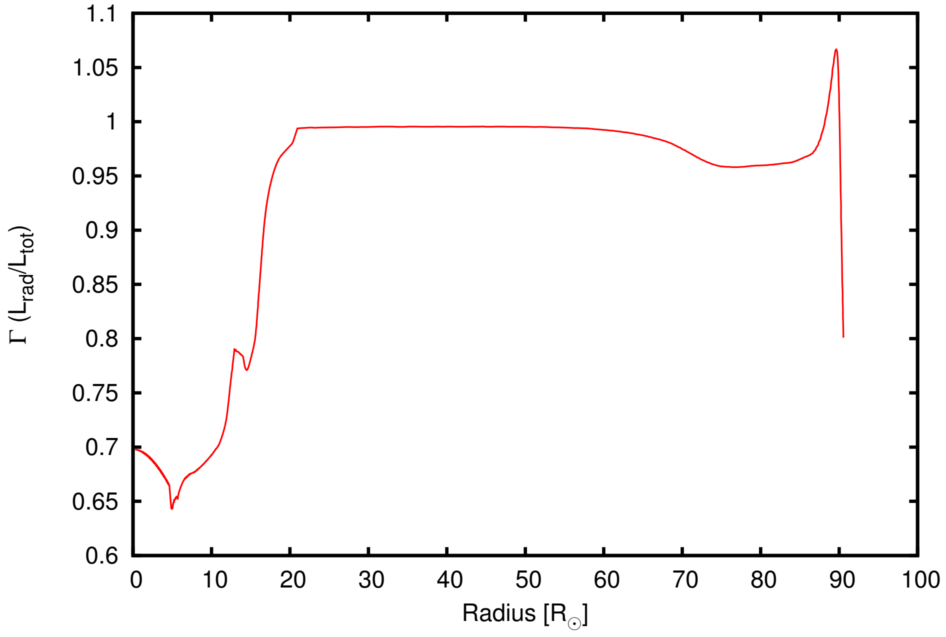

Figure 2.26: Run of Γ in the interior of the stellar model.

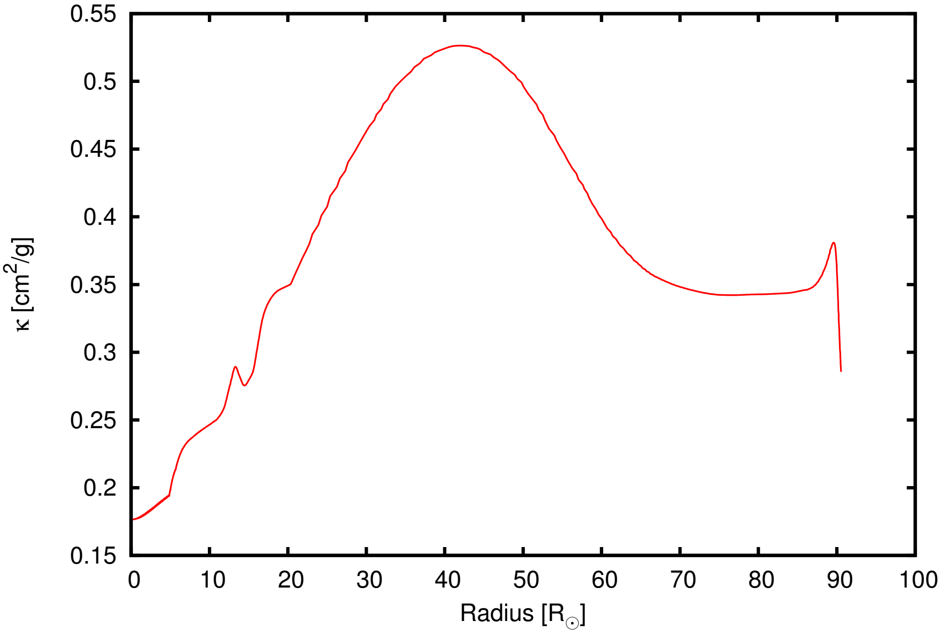

Figure 2.27: Rosseland mean opacity κ in the interior of the stellar model.

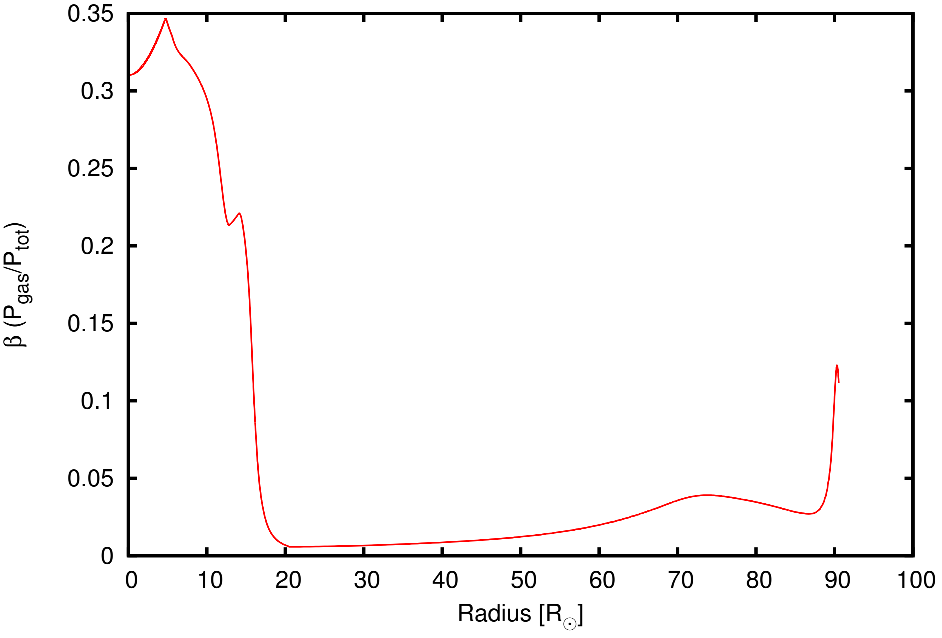

Figure 2.28: Run of $\beta(= P_{\rm gas}/P_{\rm tot})$ in the interior of the stellar model.

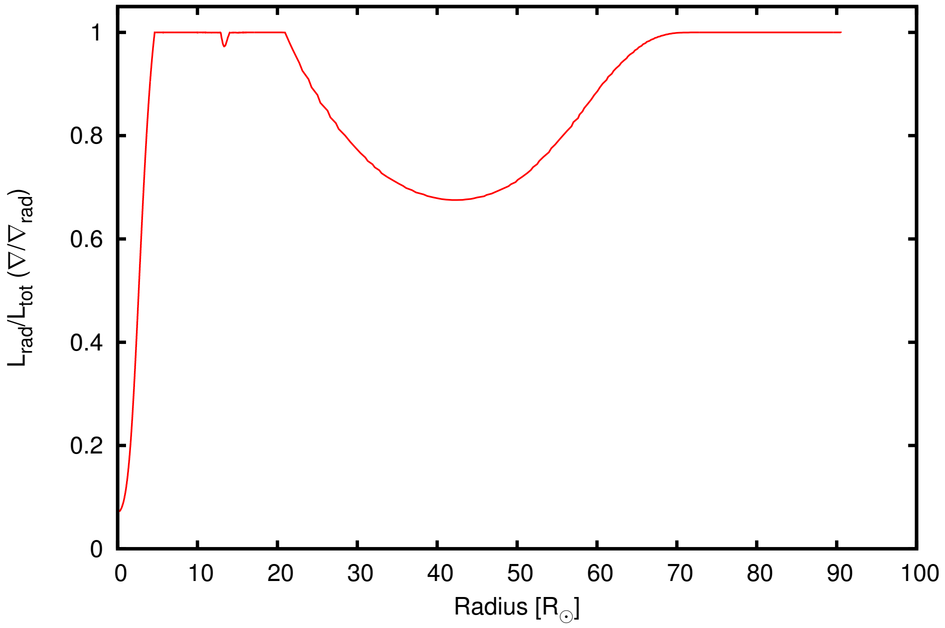

Figure 2.29: Fraction of flux carried by radiation ($L_{\mathrm{rad}}/L_{\mathrm{tot}}$) in the interior of the stellar model.

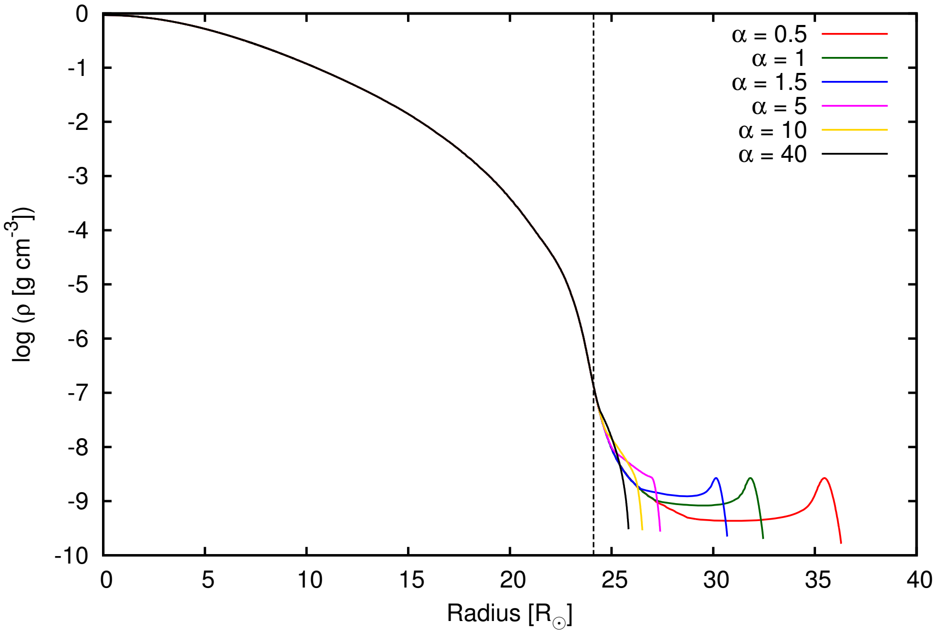

Figure 2.30: Density profile of a 300 $M_\odot$ model with different values of the mixing length parameter α (see Sec. 2.2). The black dotted line marks the location of r_{core}, i.e. the base of the inflated envelope where $\beta = 0.15$.

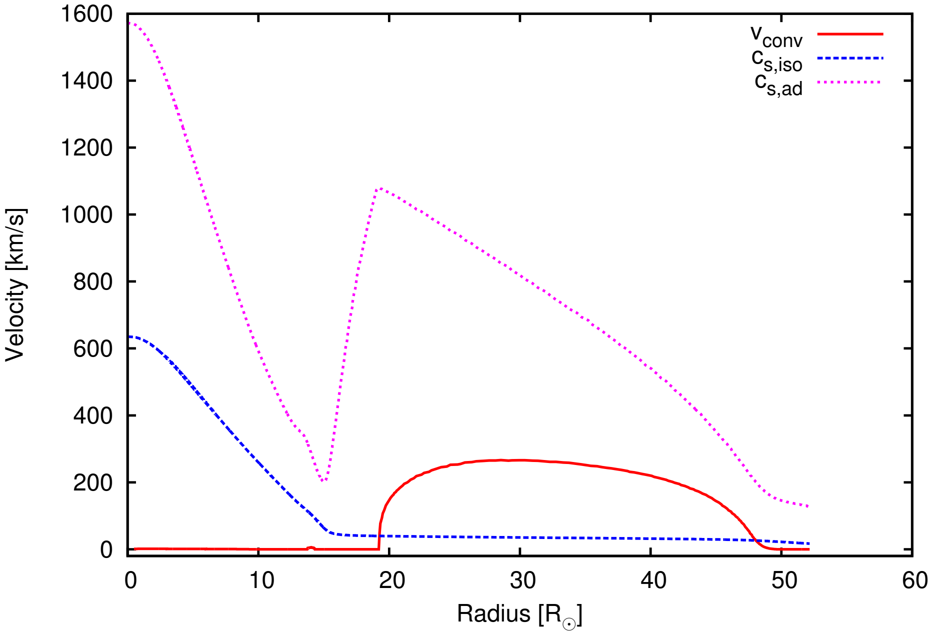

Figure 2.31: Convective velocity, isothermal sound speed, and adiabatic sound speed profiles in a 147 $M_\odot$ WNL type star with $Y_s = 89\%$.

2.10.3 Convective velocity profile in a WR model

In Fig. 2.31, the convective velocity is shown as a function of radius in a massive (147 $M_\odot$) WR-type ($Y_S = 0.89$) stellar model. The variation of isothermal and adiabatic sound speeds are also plotted for comparison. The convective velocities exceed the local isothermal sound speed in the envelope where conditions are non-adiabatic, i.e. the thermal adjustment time is short. In these models, turbulent pressure becomes important (which is not taken into account in our models) as well as standard MLT fails to be a good approximation for modelling convection.

2.10.4 Representative models

The profiles of different relevant physical quantities are shown for a few selected stellar models at five distinct effective temperatures corresponding to the three peaks in $\Gamma_{\max}$ and the two troughs in between the peaks (cf. Fig. 2.2).

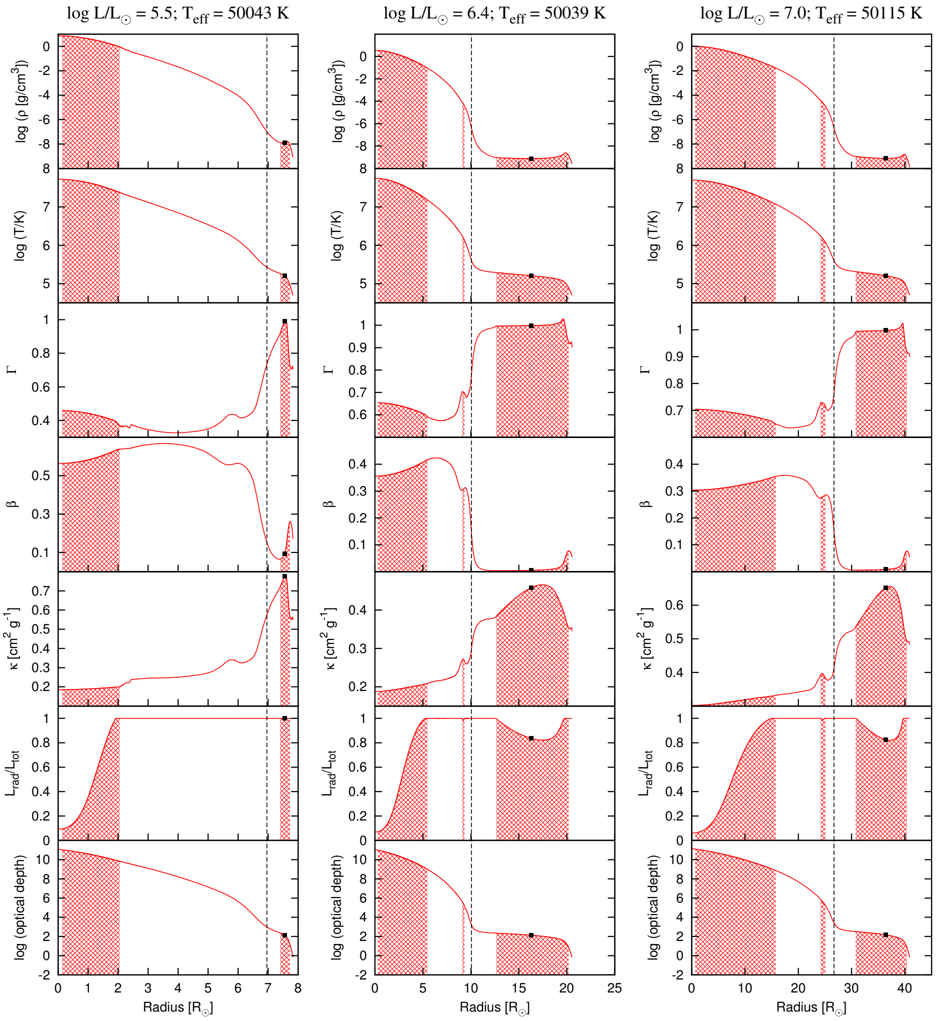

Figure 2.32: Detailed structure examples for stellar models with an effective temperature near 50 000 K, for three different luminosities (cf. Fig. 2). The dashed line marks the point at which β falls below 0.15, i.e. the beginning of the inflated envelope. The square symbol marks the temperature $T_{\rm Fe}$ at which κ is maximum because of the iron opacity bump. The hatched regions show the convective zones.

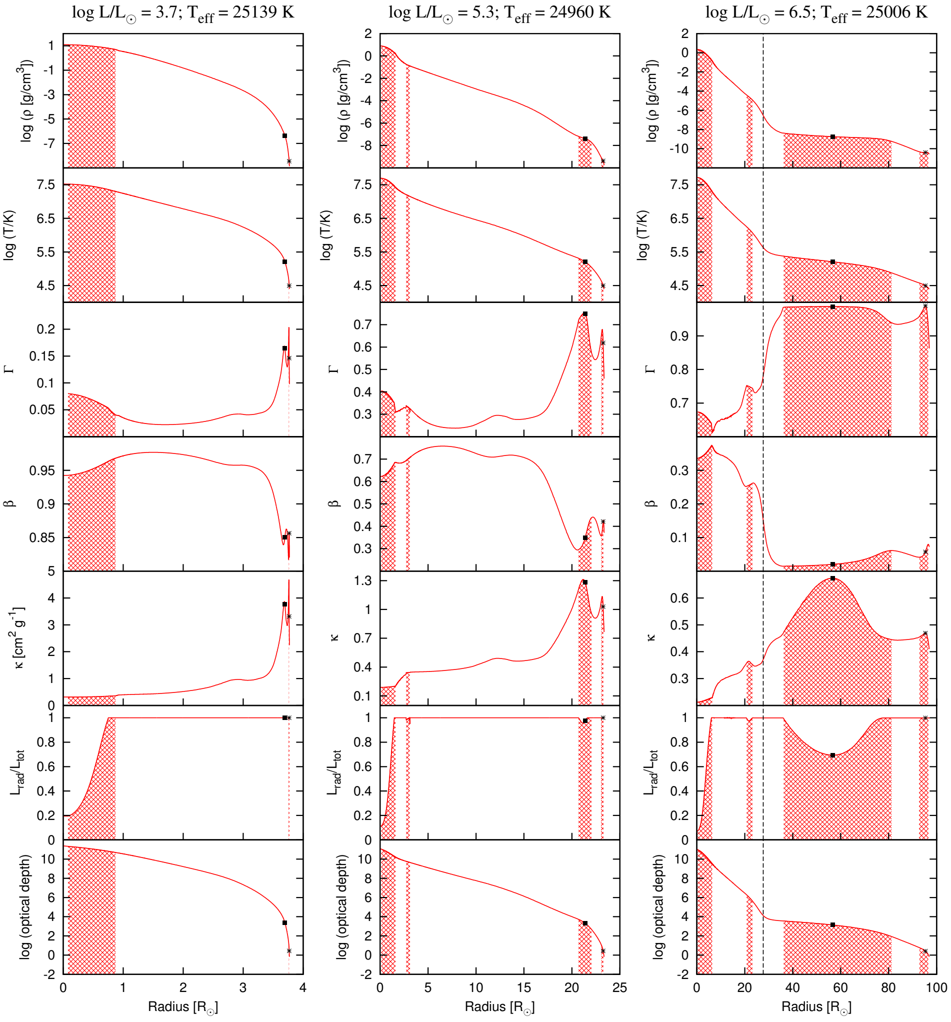

Figure 2.33: Detailed structure examples for stellar models with an effective temperature near 25 000 K, for three different luminosities (cf. Fig. 2). The dashed line marks the point at which β falls below 0.15, i.e. the beginning of the inflated envelope. The square and the cross mark the temperatures $T_{\rm Fe}$ and $T_{\rm Fe}$ at which κ is maximum because of the iron and the helium opacity bumps respectively. The hatched regions show the convective zones.

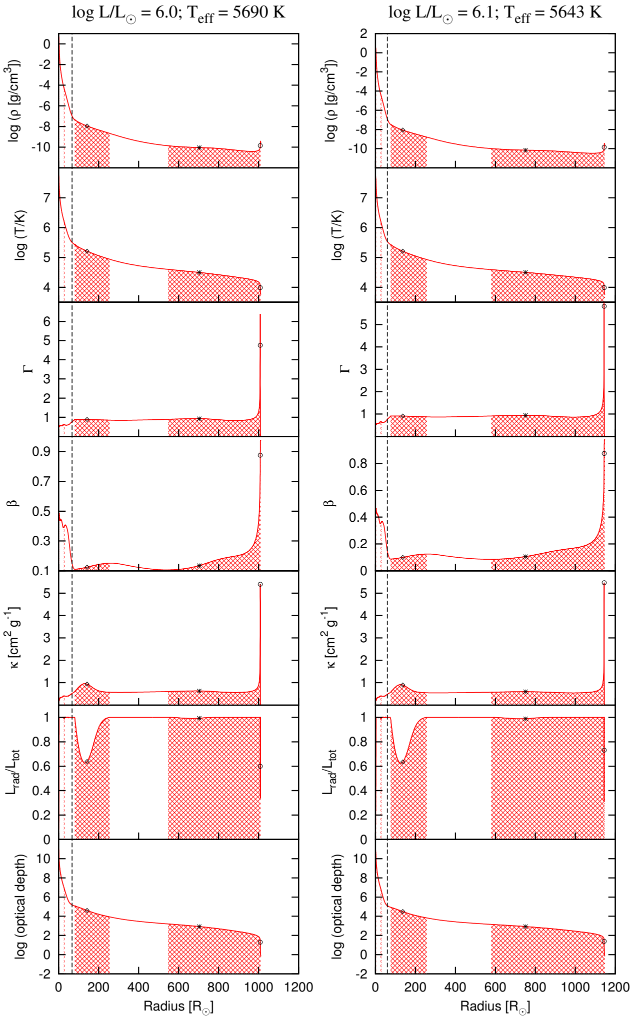

Figure 2.34: Detailed structure examples for stellar models with an effective temperature near 5 000 K, for two different luminosities (cf. Fig. 2). The dashed line marks the point at which β falls below 0.15, i.e. the beginning of the inflated envelope. The square, cross and the circle mark the temperatures T_{Fe}, T_{He}, and T_{H} at which κ is maximum because of the iron, helium, and hydrogen opacity bumps respectively. The hatched regions show the convective zones.

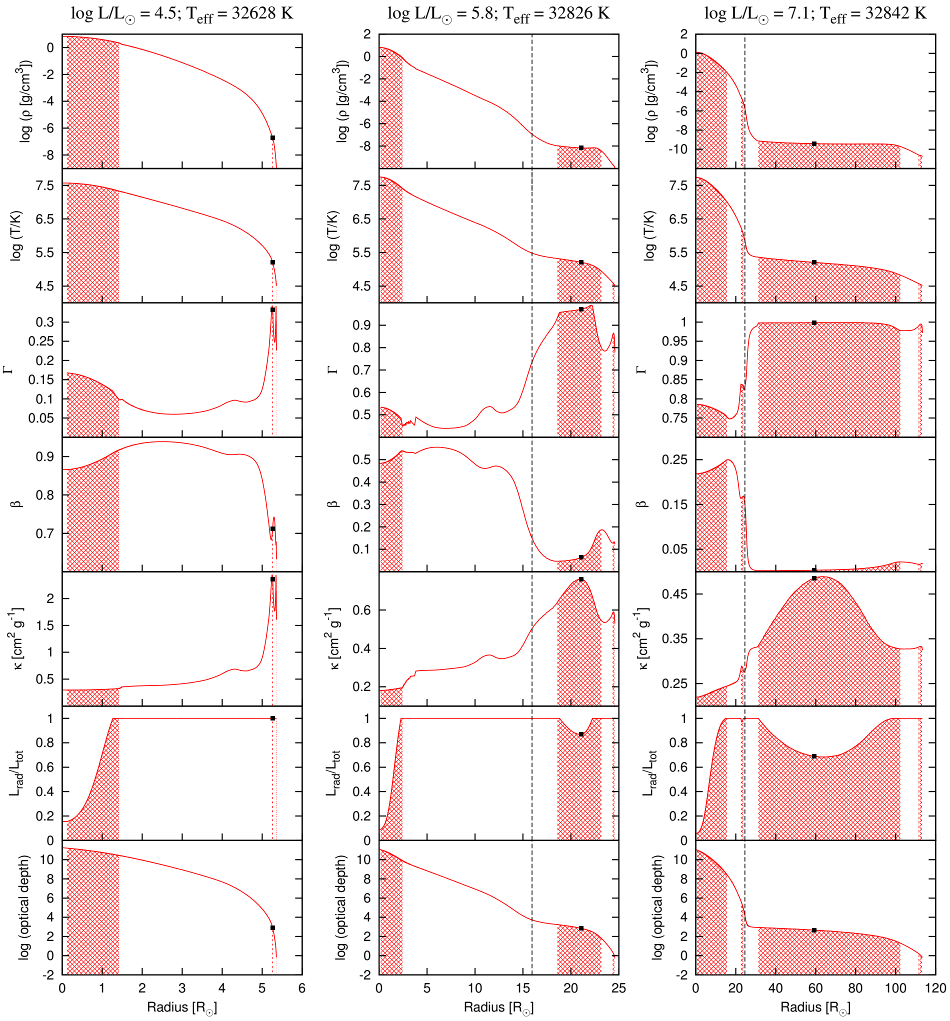

Figure 2.35: Detailed structure examples for stellar models with an effective temperature near 32 000 K, for three different luminosities (cf. Fig. 2). The dashed line marks the point at which β falls below 0.15, i.e. the beginning of the inflated envelope. The square symbol marks the temperature $T_{\rm Fe}$ at which κ is maximum because of the iron opacity bump. The hatched regions show the convective zones.

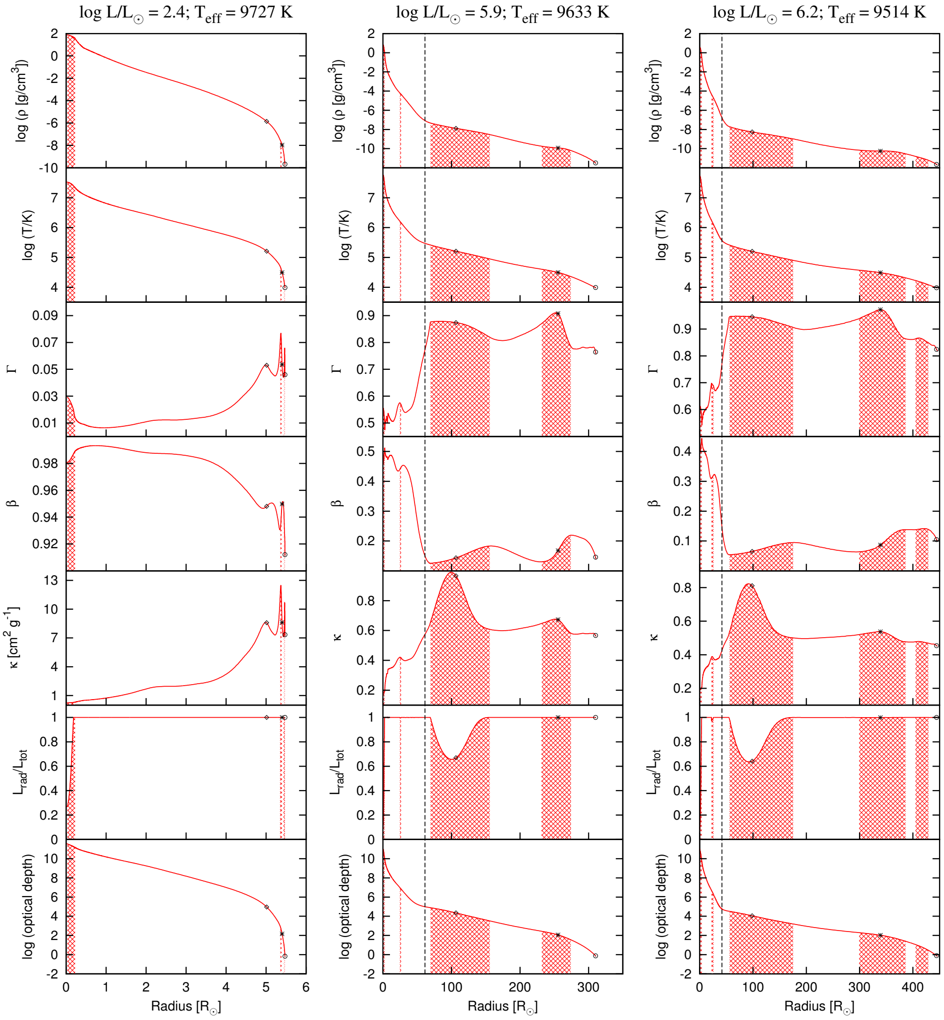

Figure 2.36: Detailed structure examples for stellar models with an effective temperature near 10 000 K, for three different luminosities (cf. Fig. 2). The dashed line marks the point at which β falls below 0.15, i.e. the beginning of the inflated envelope. The square, cross and the circle mark the temperatures $T_{\rm Fe}$, $T_{\rm He}$, and $T_{\rm H}$ at which κ is maximum because of the iron, helium, and hydrogen opacity bumps respectively. The hatched regions show the convective zones.

CHAPTER 3

The metallicity dependence of envelope inflation in massive stars

D. Sanyal, N. Langer, D. Szécsi, S.-C. Yoon and L. Grassitelli

Accepted in *Astronomy & Astrophysics*

3.1 Introduction

Massive stars, although rare, are cosmic engines in the universe. They drive the dynamical and chemical evolution of galaxies with their strong stellar winds, high luminosities and spectacular explosions. The earliest massive stars, i.e. the metal-free Population III stars may have played a major role in the reionisation of the universe (Bromm et al. 2009). Furthermore, massive stars in low metallicity environments are believed to be the progenitors of long duration gamma ray bursts and pair instability supernovae (Heger & Woosley 2002; Langer et al. 2007). Recent discoveries of superluminous supernovae like SN 2007bi (Gal-Yam et al. 2009) also point towards very massive stars as progenitors. Modelling the evolution of massive stars even on the main sequence become challenging at higher masses because of two major uncertainties: mass-loss and energy transport processes (Langer 2012). Accurate models of massive stars across a wide range of metallicities are therefore needed to facilitate comparisons with the available observational data.

Recently evidence has accumulated that stars more massive than the often accepted upper mass limit of $\sim 150\,\mathrm{M}_\odot$ (Figer 2005) exist in the local universe. For example, Crowther et al. (2010) estimated present day masses of up to $260\,\mathrm{M}_\odot$ for several stars in the Tarantula nebula of the LMC. Furthermore, in the recently concluded VLT-FLAMES Tarantula Survey of massive stars (Evans et al. 2011) in the LMC, Bestenlehner et al. (2014) identified three stars with initial mass estimates of $\gtrsim 150\,\mathrm{M}_\odot$. Therefore models of very massive stars with up-to-date physics have become increasingly relevant.

While the mass-luminosity ($M - L$) relation for main-sequence stars is steep at lower masses, $L \propto M^5$ for $M \approx \mathrm{M}_\odot$, it is much less so at higher masses where $L \propto M^{1.1}$ for $M \approx 500\,\mathrm{M}_\odot$ (Köhler et al. 2015). In general one can show that $L \propto M^\alpha$ such that $\alpha \to 1$ for $M \to \infty$

(Kippenhahn et al. 1990). Therefore one might wonder whether the Eddington limit, which is proportional to L/M, will ever be reached considering simple opacity laws. The Eddington limit is considered to be of central importance to the stability consideration of massive stars as noted by A. S. Eddington in Eddington (1926), where he pointed out that if stars have a luminosity greater than its Eddington luminosity, then the radiation emitted would blow up the star.

The classical Eddington limit, that is proportional to the electron-scattering opacity and the star's L/M ratio, is reached at $\gtrsim 10^5\,\mathrm{M}_\odot$ for Solar composition (Kato 1985, 1986). But, when the Eddington limit is defined in the stellar interior considering the Rosseland mean opacity, Sanyal et al. (2015) showed that main-sequence models with LMC composition reach the Eddington limit at a mass of $M \simeq 40\,\mathrm{M}_\odot$. Such stellar models, instead of developing a strong outflow, re-adjust their structure such that a dilute and extended envelope is produced, a process which is called envelope inflation. This effect was earlier pointed out by Ishii et al. (1999) for zero-age main-sequence models, and by Petrovic et al. (2006) and Gräfener et al. (2012) for helium star models. As a result of such an envelope structure the surface temperatures of these models are much lower than they would have been without this effect, and has consequences for the further evolution of the stars (Köhler et al. 2015). Indeed, the distribution of OB stars in our Galaxy shows many stars with masses $> 30\,\mathrm{M}_\odot$ in the effective temperature range $10\,000 - 30\,000\,\mathrm{K}$, and it has been suggested that these stars are affected by envelope inflation (Castro et al. 2014).

The metallicity (Z) of a star affects many of its physical properties like the wind mass-loss rate, opacity and the equation of state. The OPAL opacity tables from Iglesias et al. (1992) introduced an opacity peak at $T \sim 2 \times 10^5\,\mathrm{K}$ caused by bound-bound transitions of iron-group elements. This opacity peak drastically changed the envelope structure of stellar models (Stothers & Chin 1993) and even new pulsational instability strips were discovered in the Hertzsprung-Russell diagram (Pamyatnykh 1999). Since the Eddington factor depends on opacity, the Fe-bump which is a function of Z plays a major role in determining the extent of envelope inflation in a massive star model.

In this paper, we extend the study by Sanyal et al. (2015) over a wide range of metallicities from Galactic to metal-free, and investigate the properties of the stellar models in the context of the Eddington limit and envelope inflation. Section 3.2.1 presents an overview of the grids of models used in this study while in Sections 3.2.2 and 3.3 respectively we explain our concept of the Eddington limit and envelope inflation. We discuss how the Eddington limit and envelope inflation change with metallicity in Sec. 3.4. We give our conclusions in Sec. 3.5.

3.2 Method

3.2.1 Stellar models

The stellar models used in the present study were computed with a one-dimensional hydrodynamic Lagrangian code (BEC) that includes up-to-date input physics including rotation (for details, see Heger et al. 2000; Yoon et al. 2006; Brott et al. 2011; Köhler et al. 2015, and references therein). Grids of models computed with five metallicities were used, i.e., for the Milky Way (MW), LMC, SMC, I Zwicky 18 (I Zw 18) and metal-free (PopIII). The Z_{MW}, the Z_{LMC} and the Z_{SMC} models are published in Brott et al. (2011) and Köhler et al. (2015),

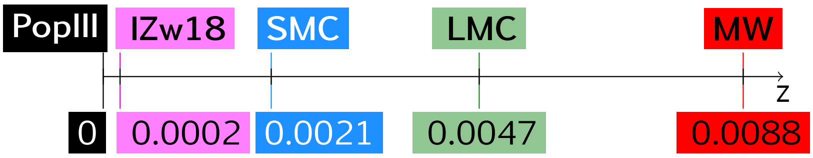

Figure 3.1: The mass fraction of the metals for the chemical compositions used in our model grids.

whereas the $Z_{\mathrm{I\,Zw\,18}}$ and the Z_{PopIII} models are from Szécsi et al. (2015) and Yoon et al. (2012b), respectively. The initial chemical compositions and the initial mass ranges in each of these grids are summarised in Table 3.1, and the values of the metallicities on a linear scale are shown in Fig. 3.1. In this paper, we consider only the core hydrogen burning models that are either non-rotating or slowly rotating, i.e. with $v_{\mathrm{rot}} \leq 100\,\mathrm{km\,s^{-1}}$, v_{rot} being the initial equatorial rotational velocity at the photosphere.

Table 3.1: The initial chemical compositions (in mass fraction) and the range of initial masses (in units of $\mathrm{M_\odot}$) of the stellar evolutionary sequences at different metallicities that were used in this study. The symbol $X_{\mathrm{i},\odot}$ refers the mass fraction of the element i in the Sun.

	MW	LMC	SMC	I Zw 18	PopIII
$X_{\mathrm{Fe}}/X_{\mathrm{Fe},\odot}$	1	0.454	0.246	0.025	0
$X_{\mathrm{O}}/X_{\mathrm{O},\odot}$	1	0.641	0.276	0.028	0
X_{He}	0.264	0.256	0.251	0.248	0.240
M_{init}	3 – 100	1 – 500	5 – 60	9 – 294	10 – 1000

The standard non-adiabatic mixing length theory (MLT, Böhm-Vitense 1958; Kippenhahn et al. 1990) was used to model the energy transport in the convective zones in the stellar interior with a mixing length parameter of $\alpha = l/H_{\mathrm{p}} = 1.5$ (Langer 1991), where l is the mixing length and H_p is the pressure scale height. The parameters for core-convective overshooting ($\alpha = 0.335$) and rotationally induced chemical mixing ($f_c = 0.0228$, $f_\mu = 0.1$) were adopted from Brott et al. (2011). Transport of angular momentum by Spruit-Tayler dynamo (Spruit 2002) was treated following Petrovic et al. (2005). Radiative opacities from the OPAL tables (Iglesias & Rogers 1996) were used for temperatures above 8000 K. For temperatures below 8000 K the opacity tables from Alexander & Ferguson (1994) were used.

3.2.2 The Eddington Limit

Conventionally, a star is considered to be at the Eddington limit when its luminosity L equals its Eddington luminosity (L_{Edd}), defined as the condition when the radiative acceleration (g_{rad}) balances the gravitational acceleration (g) at the stellar surface. The radiative acceleration is proportional to the stellar luminosity and the opacity κ. Considering electron scattering as the only source of opacity, i.e., $\kappa = \kappa_e$, the classical Eddington factor is defined as

$$\Gamma_{\mathrm{e}} = \frac{g_{\mathrm{rad}}}{g} = \frac{\kappa_e L}{4\pi c G M}, \tag{3.1}$$

where the physical constants have their usual meaning. Using this definition, stellar models reach the Eddington limit only at masses $M \gtrsim 10^5$ $\mathrm{M}_\odot$ (Kato 1986).

When the Rosseland mean opacities are used, the LMC models from Köhler et al. (2015) do not reach the Eddington limit at their surface, even at 500 $\mathrm{M}_\odot$ (Sanyal et al. 2015). However, one can also define an Eddington factor locally (Langer 1997) such that

$$\Gamma(r) := \frac{L_{\mathrm{rad}}(r)}{L_{\mathrm{Edd}}(r)} = \frac{\kappa(r) L_{\mathrm{rad}}(r)}{4\pi c G M(r)}, \tag{3.2}$$

where $M(r)$ is the Lagrangian mass coordinate, $\kappa(r)$ is the Rosseland mean opacity and $L(r)$ is the local luminosity. Since the convective luminosity does not contribute to the radiative acceleration, it is not considered in Eqn. (3.2). Using this definition, core-hydrogen burning LMC models with masses as low as $\sim 40\,\mathrm{M}_\odot$ reach the Eddington limit in their interior (Sanyal et al. 2015). However, instead of a super-Eddington outflow, a hydrostatic structure with an extended envelope is obtained (cf. Sec. 3.3), often associated with a density inversion. It has been argued in the literature (Langer 1997; Sanyal et al. 2015) that the concept of the Eddington limit as a stability criterion does not apply in the stellar interior. If not explicitly stated otherwise, we will use the definition in Eqn. 3.2 for the Eddington factor in the rest of the paper.

Since the Rosseland mean opacity κ depends on the chemical composition and hence the metallicity, the Eddington factor is also expected to be a function of metallicity. Sanyal et al. (2015) showed that in the LMC models from Köhler et al. (2015), the opacity peaks caused by the partial ionisation of iron group elements, helium and hydrogen shape the profile of the Eddington factor inside a massive star model. In this paper we investigate how the metallicity influences the Eddington factor in the stellar interior.

3.2.3 Mass-loss

MW, LMC, SMC and I Zw 18models:

For stellar models with effective temperatures higher than 22 000 K, the mass-loss prescription from Vink et al. (2001) was employed to account for the winds of O- and B-type stars. The mass-loss rate prescription from Nieuwenhuijzen & de Jager (1990) was used at effective temperatures less than 22 000 K, if the Nieuwenhuijzen & de Jager (1990) mass-loss rate exceeded that of Vink et al. (2001). In the Wolf-Rayet (WR) evolutionary phases, i.e. when the surface helium mass fraction (Y_s) is greater than 70%, the empirical mass-loss rates from Hamann et al. (1995) was used, scaled down by a factor of 10 (Yoon et al. 2006).

Pop III models:

For metal-free hot stars, a very low mass-loss rate of $10^{-14}\ \mathrm{M}_\odot\ \mathrm{yr}^{-1}$ is predicted near the classical Eddington limit (Marigo et al. 2003; Krtička & Kubát 2006; Yoon et al. 2012b). Therefore, in the Z_{PopIII} grid stellar wind mass-loss rates were applied only if there was any surface enrichment of CNO elements by rotational mixing. Hence the non-rotating models practically did not suffer from any mass-loss over their lifetimes. For hydrogen-rich ($X_s(H) > 0.3$) rotating stars, the mass-loss prescriptions from Kudritzki et al. (1989) and Nieuwenhuijzen & de Jager (1990) were used for $T_{\mathrm{eff}} > 10^4$ K and $T_{\mathrm{eff}} > 10^4$ K respectively, with a metallicity scaling of $Z^{0.69}$. For helium-rich ($X_s(H) < 0.3$) stars, mass-loss rates following the prescription of Nugis & Lamers (2000) were applied that has a metallicity scaling of $Z^{0.5}$. However, this mass loss enhancement for helium-rich stars is employed only up to $Z = 10^{-5}$, because at higher metallicities iron lines become important and the CNO lines are not any more the main driving force causing the stellar wind (Vink & de Koter 2005).

Rotationally enhanced mass-loss

The effect of rotationally enhanced mass-loss (Friend & Abbott 1986; Langer 1997) is treated in our models as,

$$\dot{M}(\upsilon) = \dot{M}(\upsilon = 0)\left(\frac{1}{1-\Omega}\right)^{0.43}, \tag{3.3}$$

where

$$\Omega = \frac{\upsilon}{\upsilon_{\mathrm{crit}}} \quad \text{and} \quad \upsilon_{\mathrm{crit}} = \sqrt{\frac{GM}{R}(1-\Gamma_{\mathrm{avg}})}. \tag{3.4}$$

Here Γ_{avg} is the Eddington factor averaged over the region with optical depth between 2/3 and 100. The enhancement of the mass-loss rate is limited by the thermal timescale mass-loss rate of the star to avoid the singularity in Eqn. (3.3) as υ approaches υ_{crit} (Yoon et al. 2012b). Note that for the models analysed in this paper the enhancement to the mass-loss rate is negligible.

3.2.4 Additional models

In the evolutionary sequences computed by Brott et al. (2011) and Köhler et al. (2015), the data regarding the structure of a stellar model is stored for every 50th computed model, i.e., at non-regular time intervals since the time steps are not uniform along the evolution. For the $Z_{\mathrm{I\,Zw\,18}}$sequences, every 250th model is stored. In order to have a higher model density in certain parts of the HR diagram for the present study, several evolutionary tracks (without rotation) were re-computed with the same input parameters, as summarised in Table 3.2.

3.3 Envelope inflation

As already mentioned in Sec. 3.2.2, stellar layers reaching the Eddington limit in their interior lead to extended and dilute envelopes (Ishii et al. 1999; Gräfener et al. 2012; Köhler et al. 2015; Sanyal et al. 2015). An example of the density structure of such an inflated stellar model is

Table 3.2: The initial masses (in units of $M_\odot$) of the non-rotating evolutionary sequences that were re-computed for this study.

MW	LMC	SMC	I Zw 18
40	40	50	100
50	60	60	150
60	70	80	196
80	100		

shown in Fig. 3.2 where the region with a steeply declining density profile is referred to as the non-inflated core and the region with a relatively flat density profile is referred to as the inflated envelope. Whereas the core radius ($r_{\rm core}$) of this model is 25.2 $R_\odot$, the extent of the inflated envelope is about 1.7 times that of $r_{\rm core}$. The profile of the Eddington factor shows that in the core it is $\Gamma < 1$, but in the envelope $\Gamma \approx 1$. At the surface of the star, Γ drops to 0.82.

To our knowledge, an analytical criterion for inflation is not available in the literature for models at various evolutionary stages, i.e from hot WR stars (Petrovic et al. 2006) to cool core-hydrogen burning red supergiants (Gräfener et al. 2012; Sanyal et al. 2015; Szécsi et al. 2015). In this study we follow Sanyal et al. (2015) to determine whether a stellar model is inflated or not. Since inflation is related to values of the Eddington factor, which in turn implies dominance of radiation pressure over gas pressure, the inflated region must have a small enough value of β, where β is the ratio of the gas pressure ($P_{\rm gas}$) to the total pressure (P). However, for inflated models with $T_{\rm eff} \lesssim 10\,000$ K (cf. Sec. 3.4.3) the assumption of a small β-value is not valid any more in the outer part of the inflated envelope (cf. Appendix D in Sanyal et al. 2015). However, at the base of the inflated region we find this assumption to be always valid. For all the model grids considered in this paper we therefore adopt a threshold value of $\beta = 0.15$ to identify the base of the inflated envelope $r_{\rm core}$ in a stellar model in accordance with Sanyal et al. (2015). We motivate our choice of using a threshold value of β to identify the occurrence of an inflated envelope below.

The equation of hydrostatic equilibrium inside a star is given as

$$\frac{dP}{dr} = -\rho g, \tag{3.5}$$

where ρ is the density at r. Writing $P = P_{\rm gas} + P_{\rm rad}$ where the radiation pressure is $P_{\rm rad} = \frac{1}{3}aT^4$, the above equation can be cast in the following form:

$$(\Gamma - 1) = \frac{1}{\rho g}\frac{dP_{\rm gas}}{dr}. \tag{3.6}$$

Therefore, $\Gamma \to 1$ leads to a vanishing gas pressure gradient and $\Gamma > 1$ in the hydrostatic stellar interior merely implies a positive gas pressure gradient (Joss et al. 1973; Paxton et al. 2013).

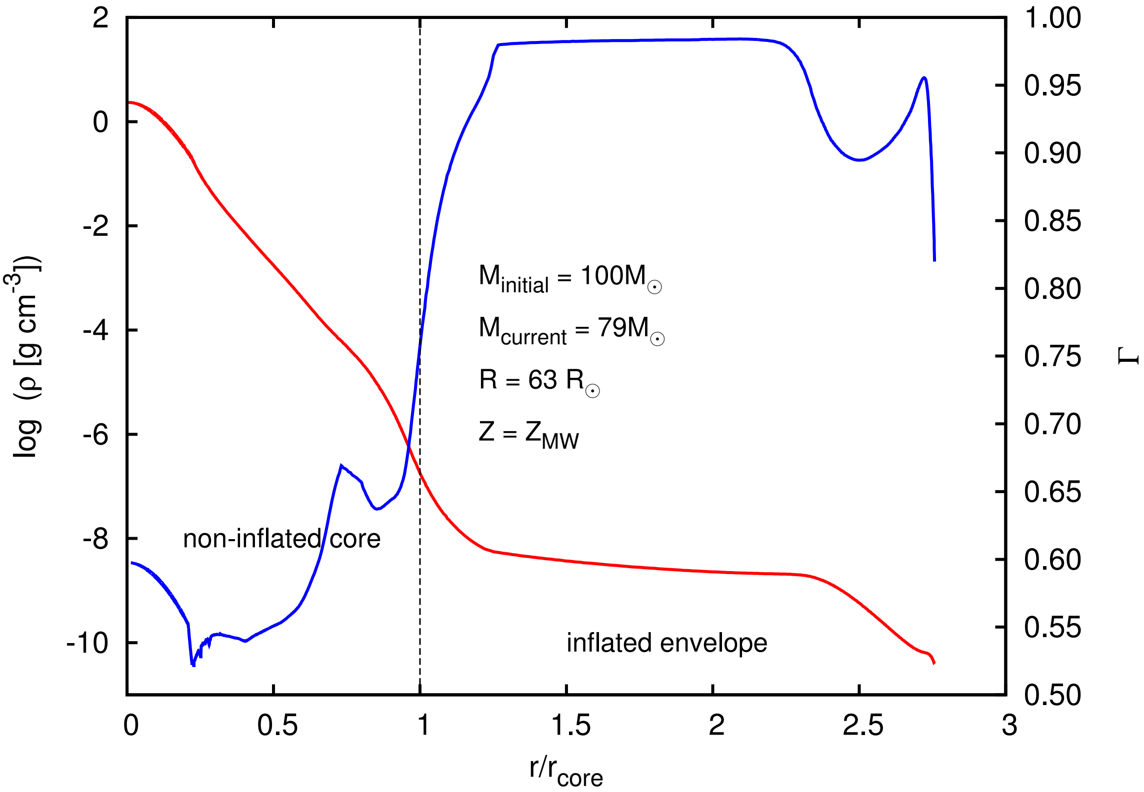

Figure 3.2: Density profile of a 79 $M_\odot$ solar metallicity core-hydrogen burning model showing the inflated envelope. The model had an initial mass of 100 $M_\odot$. The radial co-ordinate has been scaled with the core radius $r_{\rm core}$. The blue line (refer to the right Y-axis) shows the run of the Eddington factor Γ (eqn. 3.2) in the interior of the model. The Eddington factor gets close to unity in the inflated region.

Using Eqn. (3.5) in Eqn. (3.6), we get

$$(\Gamma - 1) = -\frac{dP_{\rm gas}}{dP} = -\frac{d(\beta P)}{dP} \tag{3.7}$$

$$= -\beta - P\frac{d\beta}{dP}. \tag{3.8}$$

Locally, for β either constant or slowly varying, it is

$$\Gamma \simeq 1 - \beta. \tag{3.9}$$

Therefore $\Gamma \lesssim 1$ implies a low value of β. Since we adopted $\beta = 0.15$ as the inflation criterion, we expect to find inflated models with $\Gamma > 0.85$, and this is indeed the case (Sanyal et al. 2015). Equation 3.9 was earlier arrived at by Gräfener et al. (2012) and the validity of the assumption of a constant β in the inflated envelope was shown in studies by Gräfener et al. (2012) and Sanyal et al. (2015).

To show that Eqn. (3.9) is consistent with the occurrence of a flat density profile, Eqn. (3.6) can also be written as

$$(\Gamma - 1) = \frac{1}{\rho g}\frac{d}{dr}\left(\frac{R\rho T}{\mu}\right). \tag{3.10}$$

Rearranging Eqn. (3.10) and dividing by ρT on both sides (assuming a constant μ), we get

$$\begin{aligned}\frac{1}{H_\rho} := \frac{d\ln\rho}{dr} &= \frac{\mu}{RT}(\Gamma - 1)g - \frac{d\ln T}{dr}\\ &= \frac{g\mu}{RT}\left(\Gamma - 1 + \nabla\beta\right),\end{aligned}$$

where H_ρ is the density scale height and ∇ is the temperature gradient defined as $\nabla := \frac{d\ln T}{d\ln P}$. Substituting $\beta = 1 - \Gamma$ in the above expression, we obtain

$$\frac{1}{H_\rho} = \frac{\mu g}{RT}(\nabla + 1)(\Gamma - 1), \tag{3.11}$$

which implies that $H_\rho \to \infty$ as $\Gamma \to 1$. Therefore, when $\Gamma(r)$ is close to unity, the density scale height becomes very large and leads to an extended, flat density profile which we identify as a signature of inflation.

Quantitatively, we define inflation in a stellar model as $\Delta r/r_{\rm core} := (R_\star - r_{\rm core})/r_{\rm core}$, where $R_\star$ is the stellar radius and $r_{\rm core}$ is the radial co-ordinate where the β value drops below 0.15 for the first time in the stellar interior. Since there is some arbitrariness in our inflation criterion only those models for which our criterion predicts $\Delta r/r_{\rm core} > 0.05$ are considered to be inflated.

Langer (1997) showed that if the Eddington factor as defined in the stellar interior as

$$\Gamma'(r) = \frac{\kappa(r)L(r)}{4\pi cGm(r)}, \tag{3.12}$$

i.e., taking the total luminosity into account, then the Schwarzschild criterion for convective instability can be written in the following form:

$$\Gamma'(r) \geq (1 - \beta)\frac{32 - 24\beta}{32 - 24\beta - \beta^2}. \tag{3.13}$$

For $\beta \ll 1$, the above inequality reduces to

$$\Gamma'(r) \geq (1 - \beta). \tag{3.14}$$

Since $\Gamma = \Gamma' \frac{L_{\rm rad}}{L}$ from Eqns. (3.2) and (3.13), the above inequality can be written as

$$\Gamma \geq (1 - \beta)\frac{L_{\rm rad}}{L} \tag{3.15}$$

Since $L_{\rm rad} \leq L$ everywhere inside the star, from Eqns. (3.9) and (3.14) we conclude that the inflated envelope will always be convectively unstable. Furthermore, the densities in the sub-surface convection zones of massive stars are low, and convection is strongly non-adiabatic such that in general the luminosity carried by convection is much smaller than that carried by

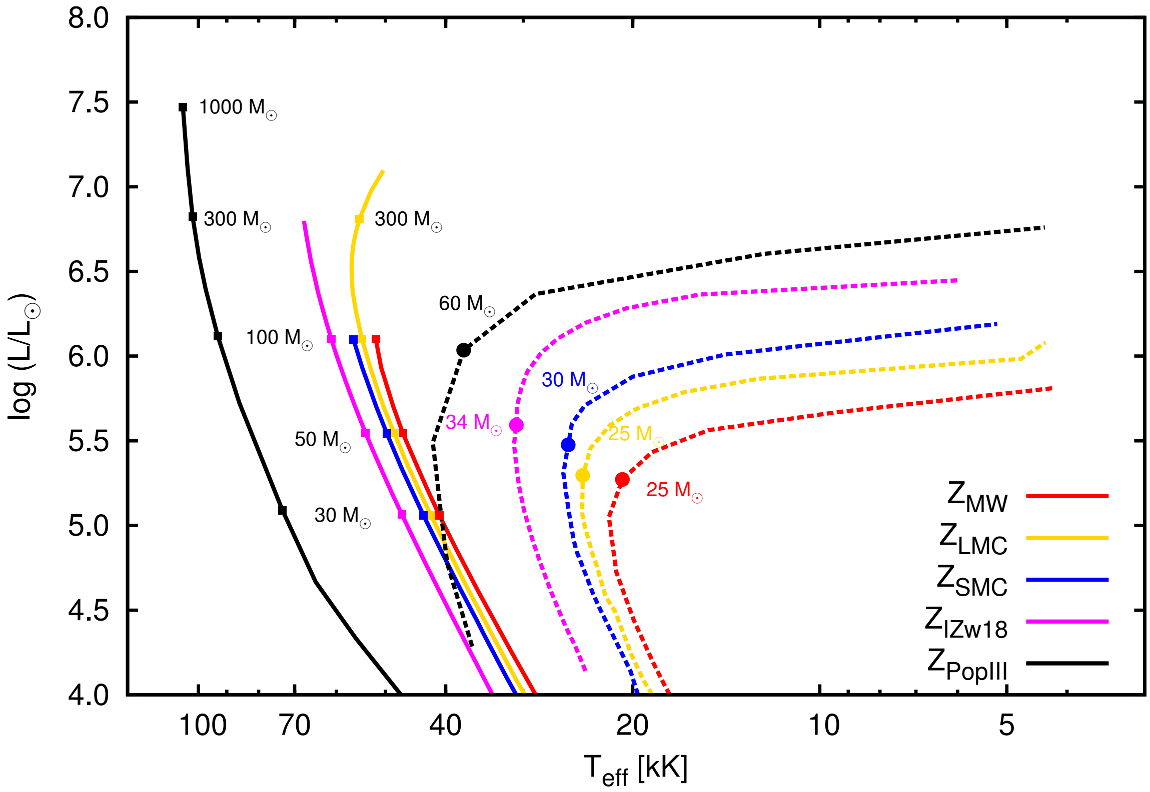

Figure 3.3: The zero-age main-sequence (solid lines) and the terminal-age main-sequence lines (dotted lines) above $\log(L/L_\odot) > 4$ of the analysed stellar models at different metallicities. The masses of some representative models (black squares) are indicated along the ZAMS. The position of the TAMS when the models start to develop envelope inflation is marked with coloured dots and the the corresponding initial masses of those models are labelled alongside.

radiation, and hence $L_{\rm rad}/L \approx 1$, or $\Gamma \approx \Gamma'$.

3.4 Results

3.4.1 Hertzsprung-Russell (HR) diagram

The HR diagram in Fig. 3.3 shows the zero-age main-sequence (ZAMS) and the terminal-age main-sequence (TAMS) of the analysed non-rotating models. The ZAMS is defined by the condition that 3% of hydrogen (by mass) has been burnt whereas the TAMS is defined by the location at which the models reach the maximum radius over their main-sequence lifetime, i.e., until the central helium mass fraction is < 0.98.

The ZAMSs of the different metallicities are located roughly parallel to one another up to $\log L/L_\odot \sim 6$ on the HR diagram, such that the Pop III ZAMS has the highest $T_{\rm eff}$ (and smallest radius) and the MW ZAMS has the lowest $T_{\rm eff}$ (and largest radius) for corresponding model masses.

The LMC ZAMS reaches a maximum $T_{\rm eff}$ of ~ 57 000 K and then starts to bend towards lower values around log $L/\rm L_\odot$ ~ 6.6, that corresponds to a mass of ~ 200 $\rm M_\odot$. Above this critical mass the surface temperature of the ZAMS models decrease further. The lower the metallicity, the higher is the luminosity and the effective temperature at which the bend is expected to be located (Ishii et al. 1999). This feature is not seen for all the metallicities in Fig. 3.3 because the initial mass ranges of the evolutionary sequences do not extend to high enough values (see Table 3.1). Nevertheless one can notice an increase in the slope of the ZAMS's in the upper HR diagram.

Using the latest OPAL opacities, the bending of the ZAMS was earlier investigated by Ishii et al. (1999). They computed models with metallicities ranging from $Z = 0.1$ to $Z = 0.004$ and found that the ZAMS curves redwards at sufficiently high masses for all the metallicities. The Solar metallicity ZAMS in their study had a bend at $M \sim 100\,\rm M_\odot$ which is consistent with our results.

The redward curving of the ZAMS is a consequence of envelope inflation of massive luminous stars, as discussed in Sec. 3.3. When the layers in the stellar interior reach the Eddington limit either because of an opacity bump or because of a high L/M ratio, the high radiation pressure pushes the layers outwards such that density and hence opacity decreases, and the Eddington factor obtains a value $\lesssim 1$.

If convection is efficient then the star does not need to re-adjust its structure, but in the luminous stars discussed here the low densities in their outer layers implies that convective energy transport within the framework of the standard MLT is not efficient enough to bring down the Eddington factor below one. Therefore the envelope expands giving rise to a core-halo density structure (Fig. 3.2).

Table 3.3: Model properties (mass, luminosity, effective temperature and the classical Eddington factor) at the points marked by filled dots in Fig. 3.3 where the TAMSs bend redwards.

Z	$M_{\rm init}$ ($\rm M_\odot$)	$M_{\rm now}$ ($\rm M_\odot$)	log $L/\rm L_\odot$	$T_{\rm eff}$ [K]	$\Gamma_{\rm e}$
MW	25	23.6	5.27	20783	0.20
LMC	25	24.4	5.29	24066	0.21
SMC	30	29.3	5.48	25409	0.26
I Zw 18	34	33.8	5.59	30787	0.30
PopIII	60	60.0	6.03	37417	0.47

The redward bend is also present in the TAMS lines of all metallicities. The higher the metallicity, the lower is the luminosity at which the bend occurs, similar to the trend expected for the ZAMS lines. The TAMS however curves redwards at a lower luminosity than the ZAMS. For example, the $Z_{\rm LMC}$ TAMS bends at log $L/\rm L_\odot \approx 5.3$ whereas the ZAMS bends at log $L/\rm L_\odot \approx 6.6$. From the mass-luminosity relation for homologous stars, we know that $L \propto \mu^\beta$ for a fixed mass, where the exponent β varies in the range $3 - 6$ (Kippenhahn et al. 1990). Therefore, at TAMS a model has a higher L/M value than at ZAMS because of a higher mean molecular weight.

The stellar parameters at the points (marked with filled dots in Fig. 3.3) where the TAMS lines bend towards cooler effective temperatures are noted in Table 3.3. This feature marks the onset of envelope inflation because below this bend we do not find any TAMS model to be inflated but above the bend we find inflated models. With a decrease in metallicity the opacity in the stellar envelope decreases (cf. Sec. 3.4.4) and hence $\Gamma \approx 1$ can be achieved only with a higher L/M value. Therefore the low-Z TAMS models show envelope inflation at higher luminosities. The TAMS extends to temperatures below $\sim 5000\,\mathrm{K}$, leading to core hydrogen-burning red supergiant models. We note that the TAMS bending occurs before we identify the first inflated model. This might be related to our ad-hoc criterion for inflation.

Furthermore, the TAMS for Z_{MW} , Z_{LMC} and $Z_{\mathrm{I\,Zw\,18}}$bend bluewards above $\log L/\mathrm{L}_{\odot}$ of 5.7, 6.0 and 6.8 respectively that has not been shown in Fig. 3.3 for the sake of clarity. This blueward bend occurs because the mass-loss rates in this part of the HR diagram are high enough to strip the hydrogen-rich outer layers of the envelope and produce helium-rich WR models (Brott et al. 2011; Köhler et al. 2015). Once the helium-rich layers are exposed, the mass-loss rates increase even further such that the models evolve towards higher surface temperatures, or the helium ZAMS.

3.4.2 The spectroscopic HR diagram

In the spectroscopic HR (sHR) diagram introduced by Langer & Kudritzki (2014), instead of the luminosity the quantity $\mathscr{L} := T_{\mathrm{eff}}^4/g$ is plotted as a function of the effective temperature. This has the advantage over the standard HR diagram that one neither needs to know the distance to a star nor its reddening to represent it on a sHR diagram. Furthermore, the quantity $\mathscr{L}$ is proportional to Γ_{e} such that

$$\Gamma_{\mathrm{e}} = \frac{\kappa_{\mathrm{e}} L}{4\pi c G M} = \frac{\kappa_{\mathrm{e}} \sigma T_{\mathrm{eff}}^4}{c g} = \frac{\kappa_{\mathrm{e}} \sigma}{c} \mathscr{L}, \tag{3.16}$$

where the constants have their usual meaning. Hence for Solar hydrogen abundance,

$$\log(\Gamma_{\mathrm{e}}) \simeq \log(\mathscr{L}/\mathscr{L}_{\odot}) - 4.6. \tag{3.17}$$

Figure 3.4 shows the maximum Eddington factor Γ_{max} in the interior of the analysed models for the five grids. Since the iron bump opacity increases non-linearly (cf. Fig. 3.8) with increasing iron abundance, i.e., with increasing metallicity, layers in the stellar interior reach the Eddington limit at a lower $\mathscr{L}$, i.e., at a lower L/M. This is demonstrated in the different panels of Fig. 3.4. Whereas we find models with $\Gamma_{\mathrm{max}} > 0.9$ for masses as low as $\sim 30\,\mathrm{M}_{\odot}$ in the MW grid, the same is achieved at $M \sim 100\,\mathrm{M}_{\odot}$ in the Pop III grid. Furthermore, an evolutionary model with a higher initial mass encounters a higher Γ_{max} earlier in its evolution because of its higher L/M ratio. For example, the $50\,\mathrm{M}_{\odot}$ MW sequence starts to develop super-Eddington layers in the midst of its main-sequence life, whereas the $80\,\mathrm{M}_{\odot}$ sequence already has $\Gamma_{\mathrm{max}} > 1$ on its ZAMS.

In the Z_{MW} and the Z_{LMC} grids, there are models with $\Gamma_{\mathrm{max}} > 1$ in the T_{eff} range $35 - 55\,\mathrm{kK}$. These models have the Fe opacity peak close to their surface where convective energy transport is inefficient such that Γ_{max} reaches values above one (Sanyal et al. 2015). In the temperature

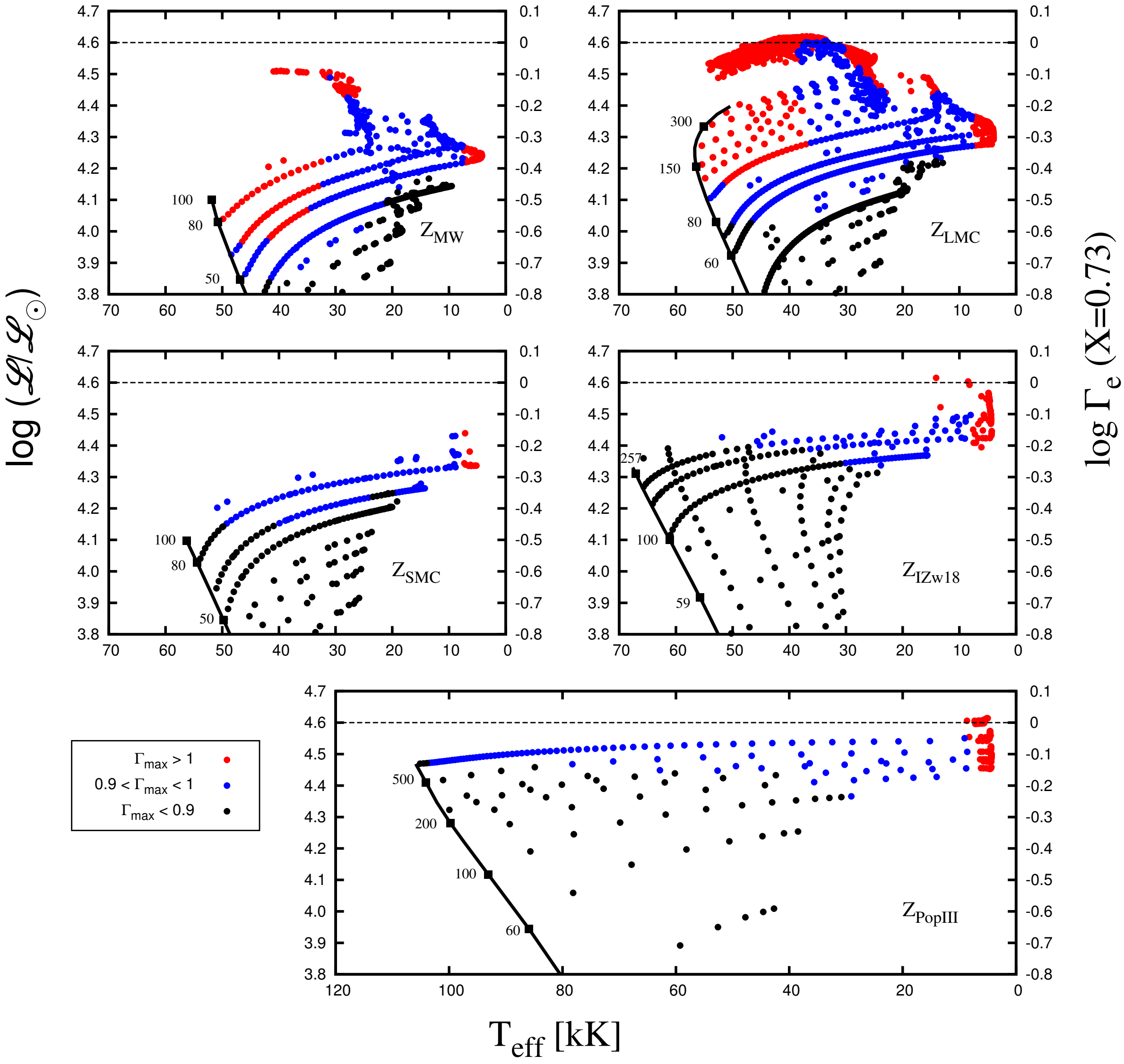

Figure 3.4: Spectroscopic Hertzsprung-Russell diagrams showing the non-rotating and slowly-rotating core-hydrogen burning models in the five grids corresponding to the different metallicities (see labels). The left Y-axis shows the quantity $\log(\mathscr{L}/\mathscr{L}_\odot)$ whereas the right Y-axis shows the corresponding values of $\log(\Gamma_e)$, in all the five panels. The Γ_e values are computed at the stellar surface considering electron-scattering opacity with a hydrogen abundance of $X = 0.73$ (completely ionised) and the black dotted line marks the location $\Gamma_e = 1$. Note that the assumption of completely ionised hydrogen breaks down for models with $T_{\rm eff}$ below $\approx 10\,000$ K. Black, blue and red dots correspond to models with $\Gamma_{max} < 0.9$, $0.9 < \Gamma_{max} < 1$ and $\Gamma_{max} > 1$, respectively. Only the models with $\log(\mathscr{L}/\mathscr{L}_\odot) > 3.8$ have been shown. The black solid line is the ZAMS and the masses of some representative models (in units of $M_\odot$) have been indicated.

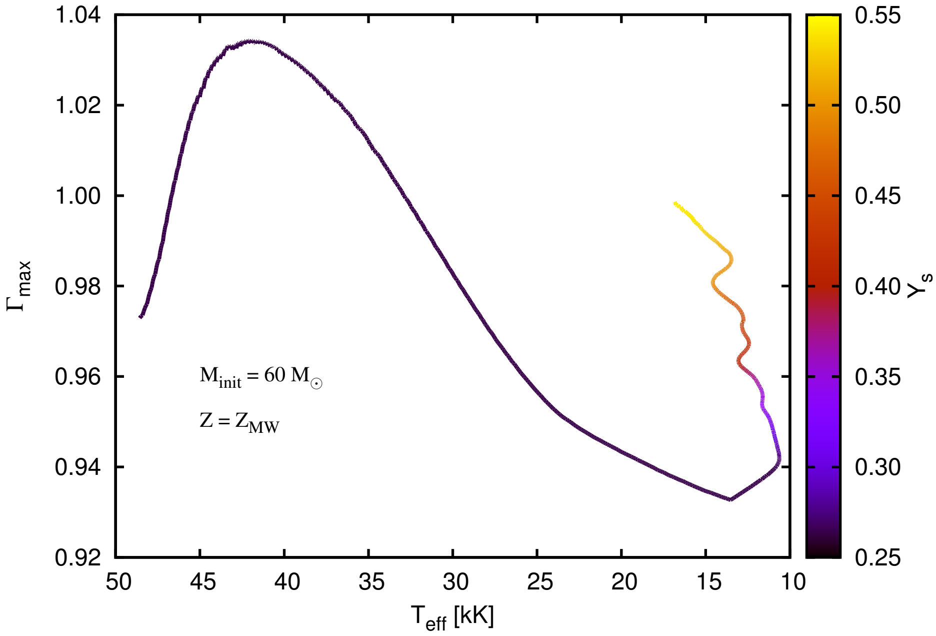

Figure 3.5: Evolution of $\Gamma_{\rm max}$ with $T_{\rm eff}$ for the $60\,{\rm M}_\odot$ $Z_{\rm MW}$ sequence. The colour depicts the surface helium mass fraction.

range 20 – 30 kK but at $\log(\mathscr{L}/\mathscr{L}_\odot) > 4.4$, we also find models with $\Gamma_{\rm max} > 1$. These models are hydrogen-deficient, either because of strong mass-loss or because of efficient rotational mixing previously. The super-Eddington layers in these models are caused by the helium opacity bump located close to their surface, coupled with inefficient convection. The models with SMC metallicity or lower do not evolve to have helium-rich envelopes during their main-sequence evolution, at least not in the mass and rotational velocity range considered here. For the SMC and the I Zw 18metallicity, the Fe-opacity peak, although present, is much weaker compared to the MW and the LMC. In other words, to reach the same value of $\Gamma_{\rm max}$ the models with lower metallicity need to have a higher L/M ratio.

In the $60\,{\rm M}_\odot$ MW sequence for example, $\Gamma_{\rm max}$ exceeds unity very close to the ZAMS but at $T_{\rm eff} < 32$ kK $\Gamma_{\rm max}$ falls below one. This drop in $\Gamma_{\rm max}$ is explained by relatively efficient convection in the envelope as the Fe-bump moves deeper into the star where densities are relatively higher. The evolution of $\Gamma_{\rm max}$ versus $T_{\rm eff}$ for the $60\,{\rm M}_\odot$ sequence is shown in Fig. 3.5. The increase of $\Gamma_{\rm max}$ at $T_{\rm eff} < 14\,000$ K is explained by strong mass-loss that increases the L/M ratio and the surface helium abundance. However we note that $\Gamma_{\rm e}$ increases throughout its main-sequence evolution. A similar trend exists in other evolutionary sequences in Fig. 3.4.

None of the Pop III models in the investigated parameter range have $\Gamma_{\rm max} > 1$ at $T_{\rm eff} > 10\,000$ K. Since the Fe-bump is completely absent, $\Gamma = 1$ is never reached. Neither are these models helium-enriched at their surface because of negligible wind mass-loss that would have increased their L/M ratio.

The $\log \Gamma_{\rm e}$ values shown on the right Y-axis in Fig. 3.4 gives little information about the $\Gamma_{\rm max}$ in the stellar interior. For example the $80\,{\rm M}_\odot$ MW ZAMS model has super-Eddington layers in its envelope but its Γ_e value is only 0.27. This shows that Γ_e is not a good proxy for the true Γ while investigating the structure and the stability of massive star envelopes.

At the stellar surface the classical Eddington factor can not exceed unity if hydrostatic equilibrium is to be maintained. Therefore $\Gamma_e = 1$ is an impenetrable upper limit (Langer & Kudritzki 2014). However in the $Z_{\rm LMC}$ grid there are apparently many models with $\Gamma_e > 1$ (Fig. 3.4) but they are all helium enriched at the surface such that $X \ll 0.73$ (Köhler et al. 2015). The true $\Gamma_e = 1$ for these models therefore is located at a higher $\mathscr{L}$ such that they all lie below it. For example, if $X = 0$ the $\Gamma_e = 1$ line in Fig. 3.4 shifts upwards by 0.24 dex.

Across all the metallicities, there are models with $\Gamma_{\rm max} > 1$ at $T_{\rm eff} < 9000\,$K. This is because of the opacity peak caused by hydrogen recombination, and hence is not influenced by the metal content in the star. The $\Gamma_{\rm max}$ values of these models can be as high as 6 for the MW models to $\gtrsim 8$ for the Pop III models, i.e., in the outer envelope (around the hydrogen recombination temperature) of such a model the luminosity transported by radiation can be a few times the Eddington luminosity (Sanyal et al. 2015). The opacities in the hydrogen recobination zone can be ~ 10 times that of the Fe-opacity peak. Hydrostatic equilibrium in these super-Eddington layers is maintained by building up a positive gas pressure gradient and a positive density gradient (Joss et al. 1973; Sanyal et al. 2015).

One might expect that these peculiar structures, coupled with the fact that they are located beyond the observed Humphreys-Davidson (H-D) limit (Humphreys & Davidson 1979) are prone to various instabilities and possibly undergo violent mass-loss episodes such that it prevents them from staying long enough on the cool side of the H-D limit. However, in our hydrodynamic 1-D models we find no sign of a violent outflow.

3.4.3 dependence of envelope inflation on metallicity

The extent of envelope inflation in the analysed models is summarised in the sHR diagrams in Fig. 3.6. Comparing with Fig. 3.4, we note that barring a few, none of the models with $\Gamma_{\rm max} < 0.9$ are inflated whereas models with $\Gamma_{\rm max} > 1$ all have inflated envelopes. Therefore, as mentioned in Sec. 3.3 the occurrence of inflated envelopes is related to models approaching the Eddington limit (as defined by Eqn. (3.2)) in their interior. In general, the hotter models are less inflated than the cooler models for a given $\mathscr{L}$, in agreement with the results obtained by Sanyal et al. (2015). This is expected because the effective temperature is strongly affected by inflation. The strongest inflation is found in models with $T_{\rm eff} \lesssim 8000\,$K, for all Z. The most extreme cases are found in the $Z_{\rm I\,Zw\,18}$and the $Z_{\rm PopIII}$ models, where $\Delta r/r_{\rm core}$ can go up to a few hundred.

The Eddington limit is either approached with large opacities or with a high L/M ratio. Models with lower metal abundances, i.e. with a weaker Fe-opacity bump, need to attain a higher L/M ratio, or a higher Γ_e, to reach the Eddington limit and inflate their envelopes. Therefore inflation starts at higher $\mathscr{L}$ as Z goes down. However, we reiterate that reaching the Eddington limit is a sufficient, but not a necessary condition for envelope inflation to occur (cf. Eqns. (3.9) and (3.11)) because the gas pressure gradiant might also contribute in inflating the envelope.

Figure 3.7 marks the regions in the sHR diagram that separates the non-inflated models from the inflated ones, considering the same sample as in Fig. 3.6. For each metallicity grid the $T_{\rm eff}$ range of the models were divided into 20 equispaced bins and in each bin the un-inflated model

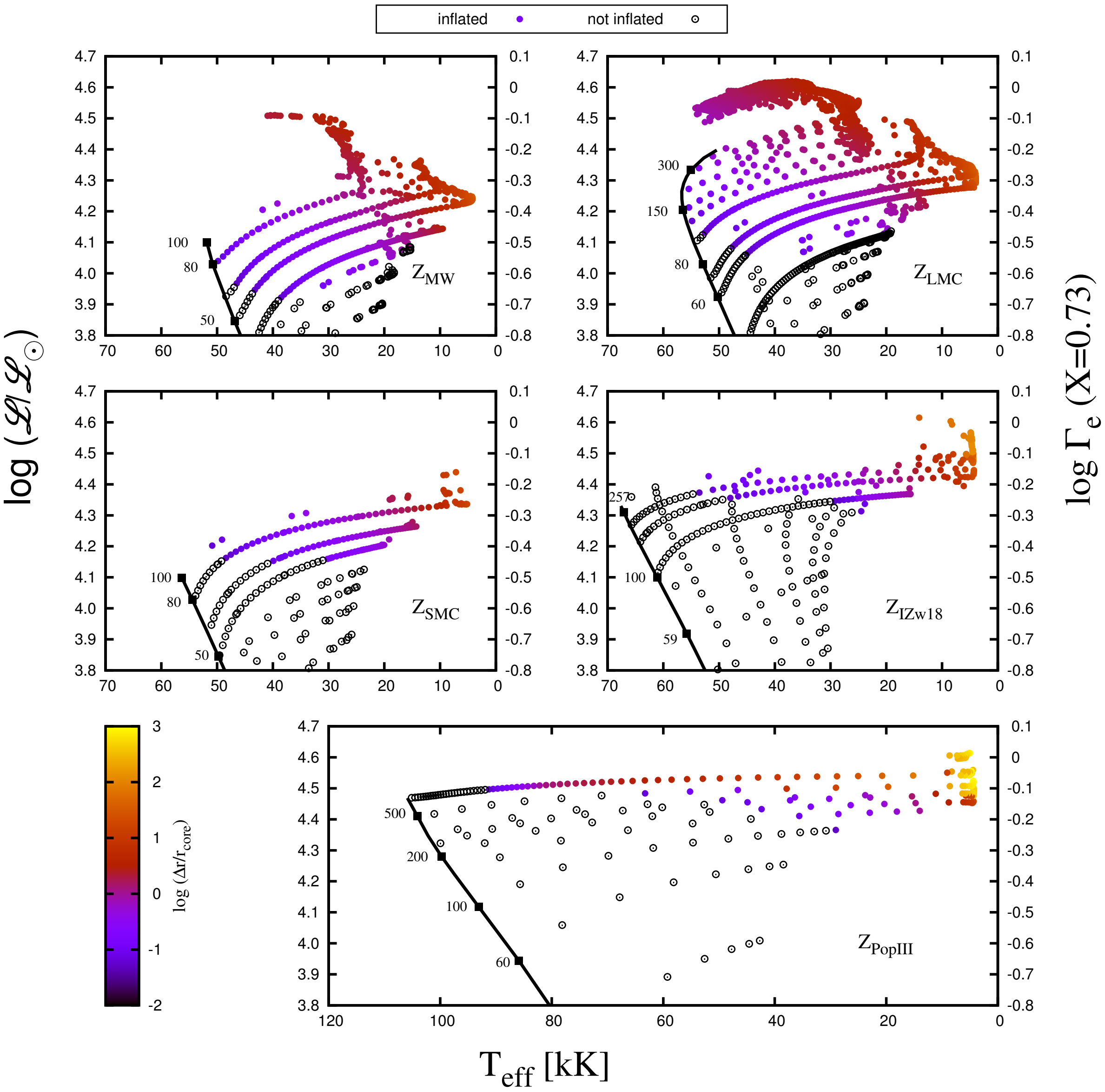

Figure 3.6: An sHR diagram showing the metallicity dependence of inflation for the analysed models in our grid. The left Y-axis shows the quantity $\log(\mathscr{L}/\mathscr{L}_\odot)$ whereas the right Y-axis shows the corresponding values of $\log(\Gamma_e)$. The Γ_e values are computed assuming a solar hydrogen abundance (completely ionised). Models marked with open black dots are not inflated whereas the coloured dots represent models with inflated envelopes. The colour of the dots indicate the strength of inflation, $\log(\Delta r/r_{\rm core})$. The black line is the ZAMS, and the masses of some representative models (in units of $M_\odot$) are indicated along it.

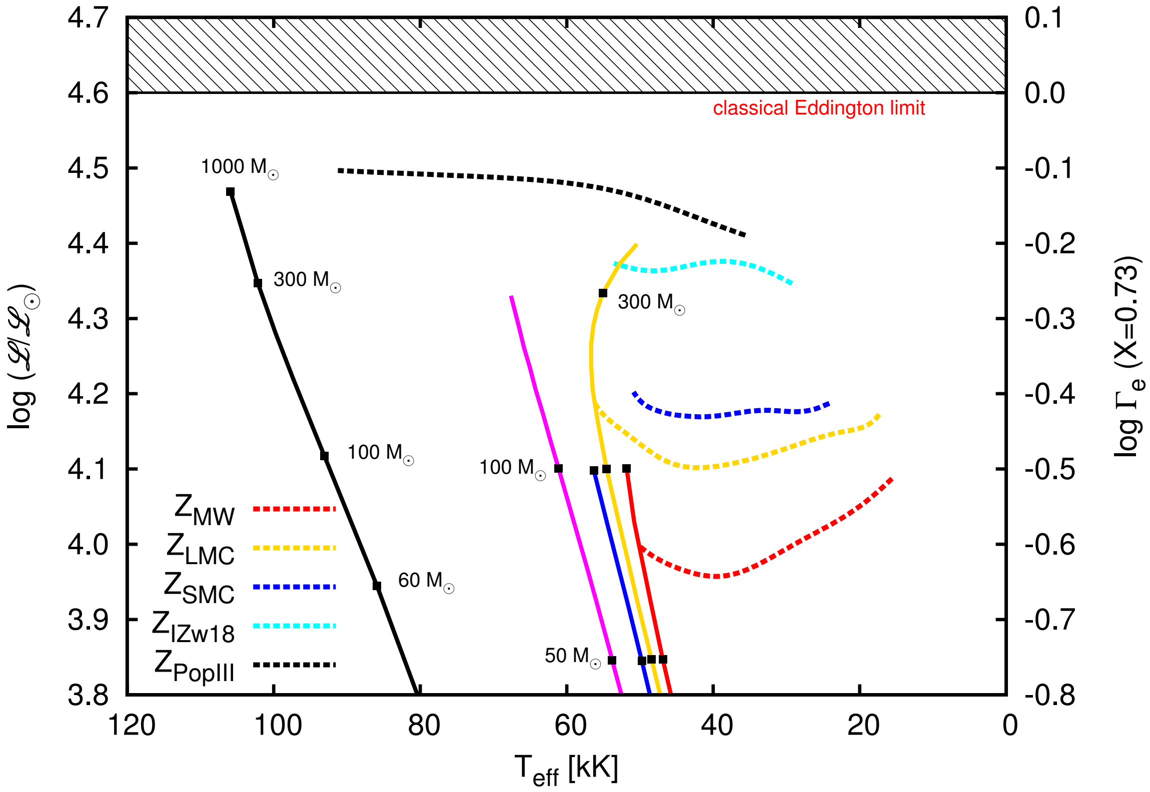

Figure 3.7: Spectroscopic Hertzprung-Russell diagram showing the boundaries (dotted lines) between non-inflated and inflated models for different metallicities such that below a given line, we do not find any inflated model for that metallicity. The solid lines represent the ZAMS. The masses at ZAMS for some of the models have been indicated. The right Y-axis represents the logarithm of the classical Eddington factor considering $X = 0.73$, similar to Figs. 3.4 and 3.6. The horizontal line marks the location $\Gamma_e = 1$ and the hatched region above it is the forbidden zone where no hydrostatic model can lie.

with the highest $\mathscr{L}$ was selected. These data points were then joined and the resulting line was smoothed using Bézier splines. These lines do not extend to $T_{\rm eff}$ below $\sim$ 10 000 K (see Fig. 3.6). This is because we do not find any core-hydrogen burning model that is not inflated in this temperature range and hence the boundaries cannot be drawn.

The lines for $Z_{\rm MW}$ and $Z_{\rm LMC}$ show a pronounced dip around $T_{\rm eff} \sim$ 35 kK. This is because of the influence of the Fe-bump coupled with inefficient convection, as previously mentioned. At lower temperatures convection becomes more efficient and so these lines move upwards to higher $\mathscr{L}$. For lower metallicities this dip is not clearly identified because the Fe-bump is either weak, or absent.

In the MW and LMC grids, the models start to develop inflated envelopes even on the ZAMS, at masses above $\sim$ 80 M$_\odot$ and $\sim$ 125 M$_\odot$ respectively. At lower metallicities this is also expected to happen, albeit at higher masses and hence at higher $\mathscr{L}$, which is beyond the parameter space explored here.

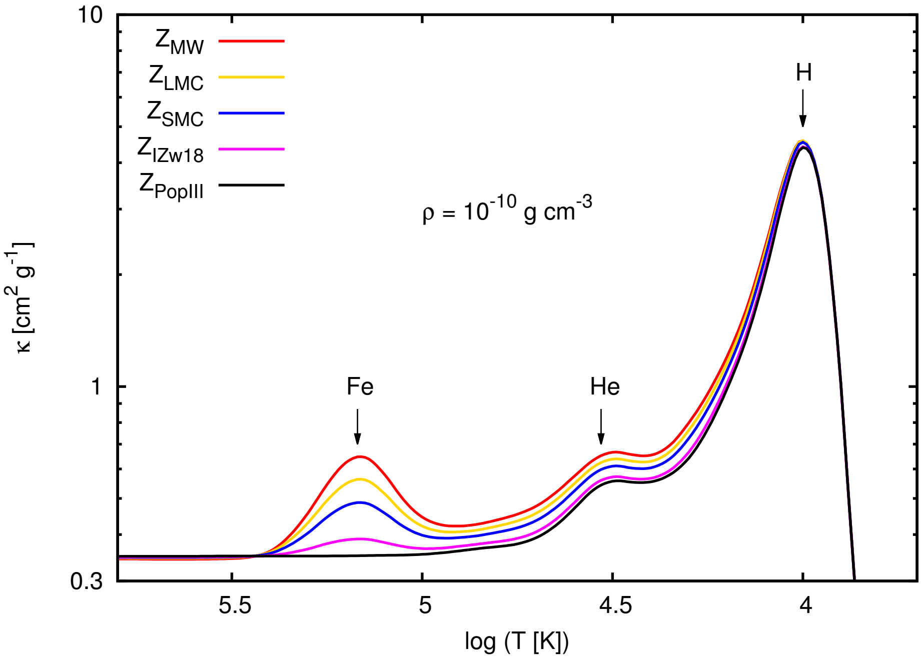

Figure 3.8: Interpolated opacities from the OPAL tables for $T_{\rm eff} > 8000$ K and from Alexander & Ferguson (1994) for $T_{\rm eff} > 8000$ K. The density is fixed at $\rho = 10^{-10}$ g cm^{-3} and opacities for the five metallicities used in this study are shown. The opacity peaks caused by iron, helium and hydrogen ionisation are marked.

3.4.4 Role of opacity in determining envelope structure

OPAL opacities

The Rosseland mean opacity κ is a function of density, temperature and chemical composition such that for a given ρ and T, κ increases with an increase in metallicity. This is demonstrated in Fig. 3.8 where the three opacity peaks caused by partial ionisation of iron, helium and hydrogen at their characteristic temperatures are visible. Note that the opacity does not vary linearly with metallicity around the Fe bump temperature. The slope $\frac{d\kappa}{dZ}$ is higher for higher values of Z. In this section we investigate how the strength of these opacity peaks determine the density structure of the inflated envelope.

In Fig. 3.9, we take a look at the OPAL opacities around the Fe-bump for the MW and LMC metallicities. As mentioned before, in the inflated envelope the condition $\Gamma \approx 1$ holds true. Let the corresponding opacity be $\kappa_{\rm Edd}$ such that $\Gamma = \kappa_{\rm Edd} L_{\rm rad} / 4\pi c G m \approx 1$. Consider two models with the same L/M but with metallicities $Z_{\rm MW}$ and $Z_{\rm LMC}$ such that $\kappa_{\rm Edd} = 0.6$ (dot-dashed line), and assume that the convective efficiency is negligible. At the peak of the Fe-bump ($\log(T/K) \approx 5.22$) marked by the vertical black line, the MW model has to decrease its density by two orders of magnitude, from 10^{-8} g cm^{-3} to $\approx 10^{-10}$ g cm^{-3} whereas the LMC model only has to go down to $\sim 10^{-9}$ g cm^{-3} to satisfy the constraint $\Gamma = 1$. Therefore, the higher metallicity model will adjust its envelope structure such that it has a lower envelope density. In practice however, convection may mediate this effect (Sanyal et al. 2015).

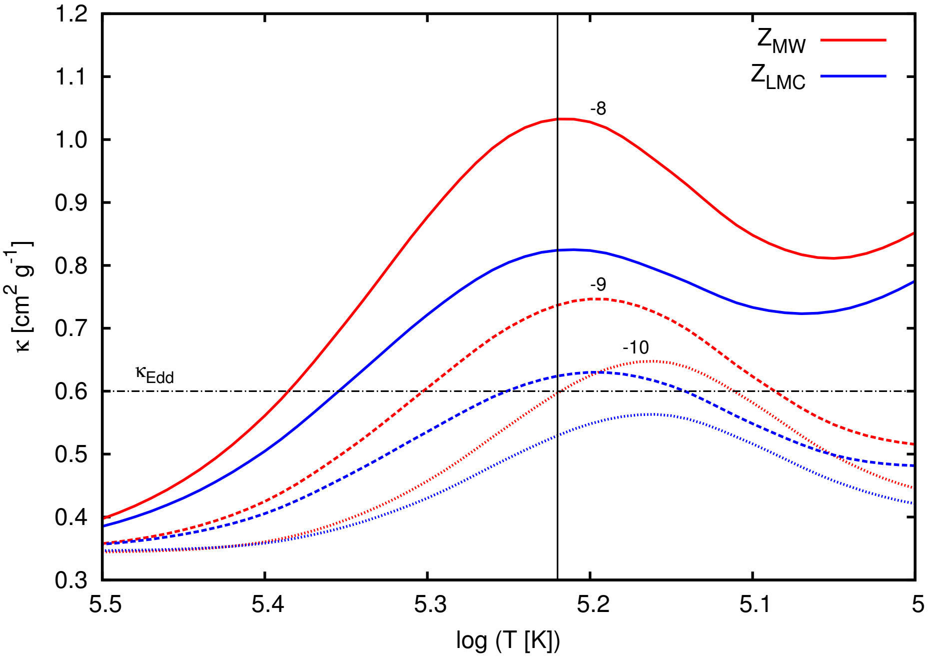

Figure 3.9: OPAL opacities for two metallicities $Z_{\rm MW}$ and $Z_{\rm LMC}$, and three different values of $\log(\rho\,[\,{\rm g\,cm^{-3}}])$ each, i.e., −8, −9 and −10, as indicated in the plot. The dot-dashed line at $\kappa = 0.6$ is the assumed location of $\kappa_{\rm Edd}$.

Opacity in the inflated envelope

As mentioned before, the opacity bumps caused by the partial ionisation zones at characteristic temperatures play a major role in determining the structure of an inflated envelope. As prototypical examples, we have selected three sequences with $Z = Z_{\rm LMC}$ and initial masses $60\,{\rm M}_\odot$, $70\,{\rm M}_\odot$ and $100\,{\rm M}_\odot$. The base of the inflated envelope in these models is located around the characteristic Fe-bump temperature $T_{\rm Fe} \approx 180\,000$ K. The maximum opacity within the Fe-bump ($\kappa_{\rm Fe}^{\rm max}$), i.e. between $5 < \log(T/K) < 5.5$, for the three sequences are shown in the top panel of Fig. 3.10, for that part of the evolution where the models are not helium-enriched at the surface, i.e. $Y_{\rm s} < 0.3$. At any given value of $\Delta r/r_{\rm core}$, the higher mass model has a lower $\kappa_{\rm Fe}^{\rm max}$ because it has higher luminosity, and hence needs to decrease its opacity further to maintain $\kappa \approx \kappa_{\rm Edd}$.

The $60\,{\rm M}_\odot$ sequence for example develops a larger inflated envelope as it evolves, while increasing its $\mathscr{L}$. The opacity within the Fe-bump and $\kappa_{\rm Fe}^{\rm max}$ therefore decrease in the initial phase because convection is relatively inefficient. As the model evolves to cooler effective temperatures, the Fe-bump goes deeper inside the star where densities are higher, and convection becomes efficient. Hence, $\kappa_{\rm Fe}^{\rm max}$ increases at $T_{\rm eff} \lesssim 25\,000$ K. In the case of the $70\,{\rm M}_\odot$ sequence however, there is a drop in $\kappa_{\rm Fe}^{\rm max}$ at $T_{\rm eff} < 5000$ K. In this phase of the evolution, a high mass-loss rate ($\sim 10^{-5}\,{\rm M}_\odot\,{\rm yr}^{-1}$) causes a sharp increase in $\mathscr{L}$. As a result, $L_{\rm rad}$ increases in the Fe-bump region. But the convective efficiency does not increase enough (for details, see Sec. 3.6.1) such that it can prevent $\kappa_{\rm Fe}$ from going down.

Models with a higher metallicity have a stronger Fe-bump, the effect of which is seen in

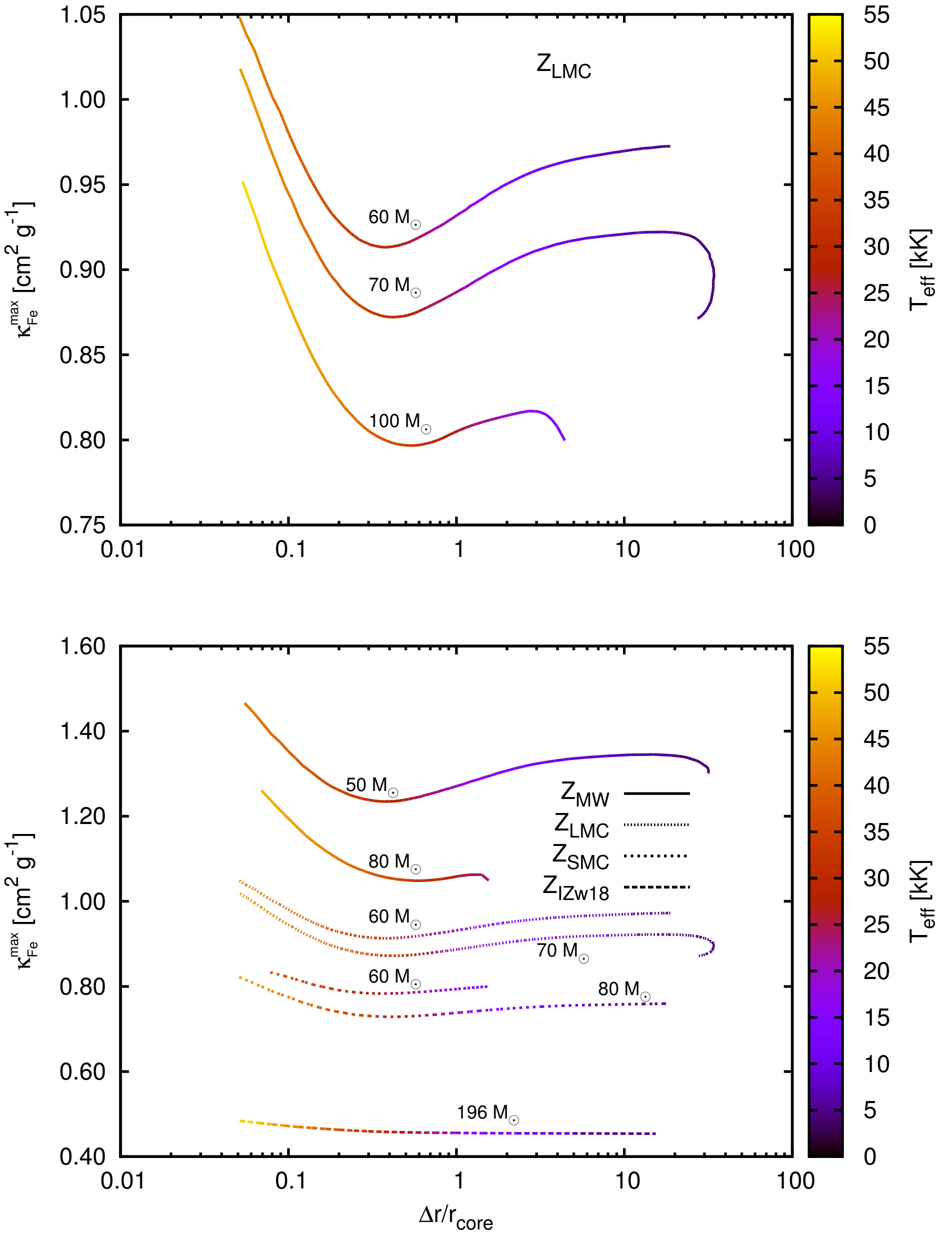

Figure 3.10: *Top:* Maximum opacity within the Fe-bump region for three different evolutionary sequences with initial masses 60, 70 and 100 $M_\odot$ from the LMC grid, as a function of $\Delta r/r_{\rm core}$. The effective temperature of the model is colour-coded. Only the part of the evolution where $Y_s < 0.3$ has been plotted. *Bottom:* Same as in the top panel, but for four metallicities.

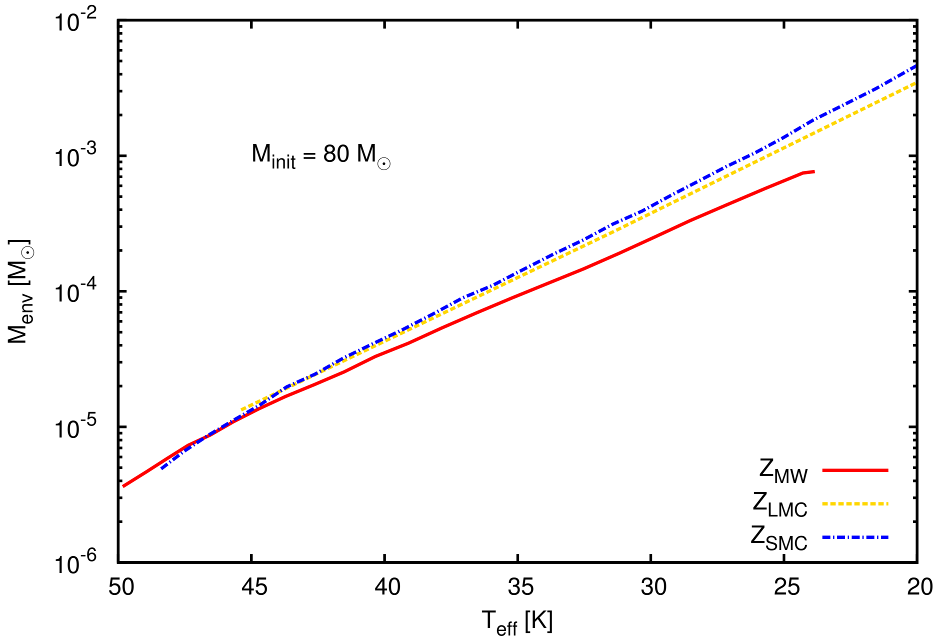

Figure 3.11: Envelope mass versus effective temperature for the 80 $M_\odot$ sequences from the MW, LMC and SMC grids. Only models in the T_{eff} range 20 – 50 kK and with $Y_s < 0.3$ are shown.

the bottom panel of Fig. 3.10. While κ_{Fe}^{max} for the 80 $M_\odot$ Z_{MW} model with the highest T_{eff} is $\sim 1.2\,cm^2\,g^{-1}$, the same quantity for the 196 $M_\odot$ $Z_{I\,Zw\,18}$model is $\sim 0.5\,cm^2\,g^{-1}$. The slope of κ_{Fe}^{max} versus $\Delta r/r_{core}$ is steeper for the Z_{MW} evolutionary sequences compared to the other sequences at lower metallicities because of the nature of the OPAL opacities explained in Sec. 3.4.4.

3.4.5 Mass contained in the inflated envelopes

In this section we investigate the inflated envelope masses of our models. In Fig. 3.11 we compare the 80 $M_\odot$ sequences in the MW, LMC and SMC model grids and show that for a given T_{eff}, the higher metallicity model has a lower envelope mass. At relatively high effective temperatures ($T_{eff} > 45\,000$ K), i.e. when the sequences start developing inflated envelopes for the first time during their evolution, the envelope masses for all three sequences are similar but at as they evolve to lower T_{eff}, the distinction becomes clear. For example, at $T_{eff} = 30\,000$ K the 80 $M_\odot$ Z_{MW} model has a distinctly smaller envelope mass than the corresponding Z_{LMC} and Z_{SMC} models, the difference in their core radii being negligible. The Z_{LMC} and the Z_{SMC} models however have comparable envelope masses over the whole T_{eff} range. This trend is probably related to the relative strength of the iron opacity peaks for these metallicities (cf. Fig. 3.8).

For evolutionary sequences of a given metallicity, say, Z_{LMC} , the ones with higher $\mathscr{L}$'s have lower envelope masses (M_{env}), as shown in the top panel of Fig. 3.12. For small inflation, i.e. $\Delta r/r_{core} < 0.1$, the envelope mass in the three Z_{LMC} sequences is comparable but as $\Delta r/r_{core}$ increases, the sequences separate out such that for a given $\Delta r/r_{core}$, the 100 $M_\odot$ sequence with the highest $\mathscr{L}$ has the lowest envelope mass and comparing with Fig. 3.10, the lowest κ_{Fe}^{max}.

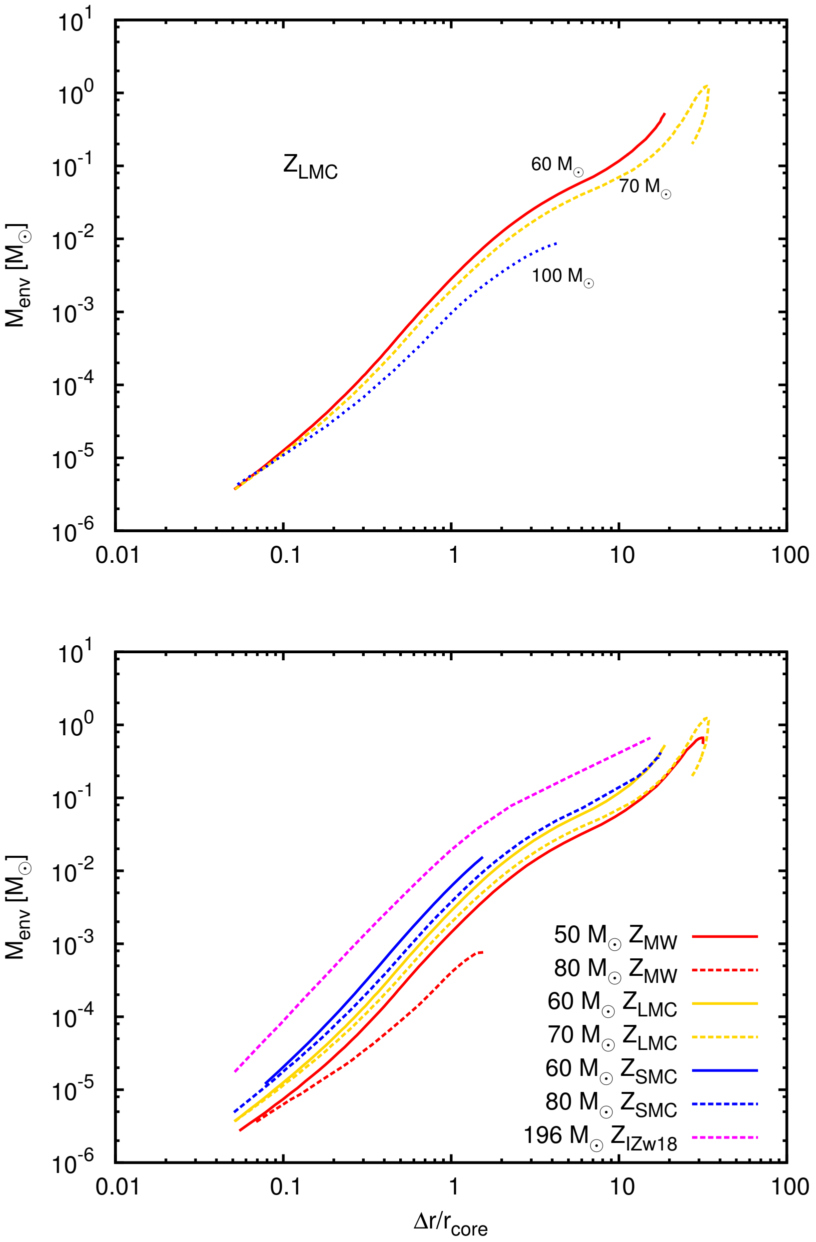

Figure 3.12: *Top:* Inflated envelope masses for 3 sequences from the LMC grid as a function of $\Delta r/r_{\rm core}$, such that $Y_s < 0.3$.
Bottom: Same as in the top panel, but for four metallicities.

We note that for the 70 $M_\odot$ sequence for example, the envelope mass varies by more than five orders of magnitude over its main-sequence lifetime. The drop in $M_{\rm env}$ near the end of the 70 $M_\odot$ sequence is because of its blueward evolution in the HR diagram caused by strong mass-loss (cf. Sec. 3.4.3).

In the bottom panel of Fig. 3.12, a few representative sequences from the MW, LMC, SMC and I Zw 18grids are shown that depicts how $M_{\rm env}$ changes with inflation. The higher metallicity models have lower envelope mass for a fixed $\Delta r/r_{\rm core}$. For example, at $\Delta r/r_{\rm core} = 1$, the 60 $M_\odot$ $Z_{\rm LMC}$ sequence has $M_{\rm env} = 3\times10^{-3}\,M_\odot$ while the 60 $M_\odot$ $Z_{\rm SMC}$ sequence has $M_{\rm env} = 6\times10^{-3}\,M_\odot$. At high inflation ($\Delta r/r_{\rm core} > 10$), some of the lines touch each other which is probably related to the different L/M ratios of the models.

We investigate the envelope masses of all the inflated models in Fig. 3.13. The envelope mass spans several orders of magnitude from $\sim 10^{-5}\,M_\odot$ to $\sim 100\,M_\odot$. In general we find that $M_{\rm env}$ increases with a decrease in $T_{\rm eff}$ for a given metallicity. This increase in $M_{\rm env}$ is distinctly steeper at $T_{\rm eff} \lesssim 8000$ K (bottom panel of Fig. 3.13) compared to that at $T_{\rm eff} > 10\,000$ K. Below 10 000 K, the low-Z models have very massive envelopes (bottom panel of Fig. 3.13). The models which contain the hydrogen opacity bump show strong density inversions (Sanyal et al. 2015) and because of this sharp rise in density the envelope mass increases.

At $T_{\rm eff} > 10\,000$ K, there is a spread in $M_{\rm env}$ over a few orders of magnitude but at the lowest effective temperatures, the spread is much narrower. This is because the sequences which evolve to effective temperatures below $\sim$ 8000 K do so for a narrow mass range. At higher initial masses strong mass-loss prevents them from evolving to low surface temperatures, and at lower initial masses inflation is not strong enough.

The envelope mass is determined both by the extent of inflation ($\Delta r/r_{\rm core}$) and the metallicity. As the metallicity increases, the models with the most massive inflated envelopes (the cool supergiants) are found at lower masses. This is a consequence of the applied mass-loss rates. The wind mass-loss prescriptions used in stellar evolution codes are generally functions of luminosity, temperature, mass, radius and chemical composition of the model. With an increase in luminosity or mass, the wind mass loss rates increase and the most massive stars in our $Z_{\rm MW}$ and $Z_{\rm LMC}$ grids become helium-rich WR stars (Köhler et al. 2015) and do not become cool enough to contain massive envelopes ($\gtrsim 1\,M_\odot$), as explained in the previous paragraph. At lower Z this happens at higher masses. At $Z = 0$ models never become helium-rich at the surface unless they are very fast rotators.

3.5 Discussion and conclusions

We have performed a study of the envelope structures of main-sequence massive star models computed with the following metallicities: $Z_{\rm MW}$, $Z_{\rm LMC}$, $Z_{\rm SMC}$, $Z_{\rm I\,Zw\,18}$and $Z_{\rm PopIII}$. We investigated the Eddington factors in their interior and its connection to envelope inflation as a function of metallicity.

As expected we found that the Eddington limit is metallicity dependent such that models with a higher Z reach $\Gamma = 1$ in their interior at a lower mass. While a 30 $M_\odot$ MW model has $\Gamma \approx 1$ in its interior, it requires a 150 $M_\odot$ Pop III model to reach similar Eddington factors on the hot side of the HR diagram, i.e., at $T_{\rm eff} > 10\,000$ K. For models with $T_{\rm eff}$ below the

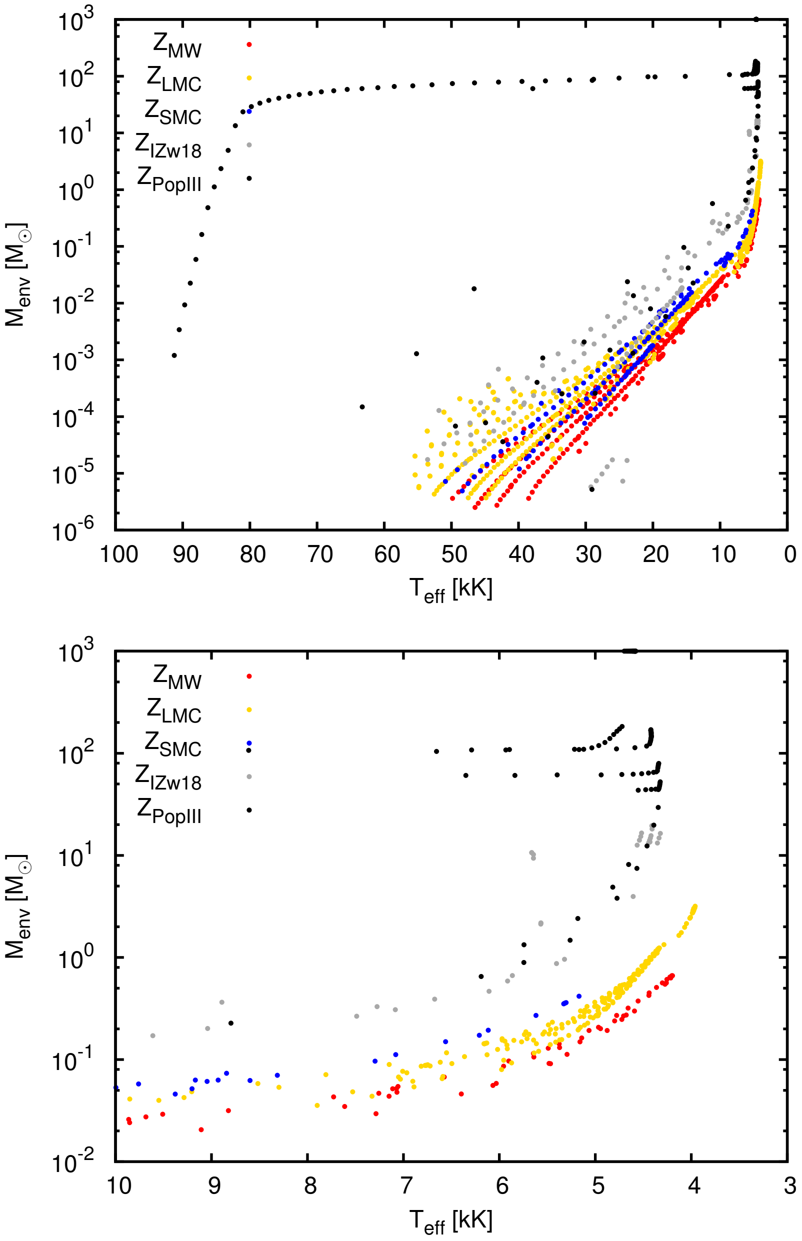

Figure 3.13: Mass contained in the envelope of inflated models as a function of their effective temperatures, for the five metallicities considered in this study. Only models with $Y_s < 0.3$ are shown. The bottom panel only shows models at $T_{\rm eff} < 10\,000$ K.

hydrogen recombination temperature, metallicity has no effect and super-Eddington layers can be found down to $\sim 5\,\mathrm{M}_\odot$ models, although in the post main-sequence phase (Langer et al. 2015). Proximity to the Eddington limit leads to envelope inflation in our models. We find inflated models at all the metallicities investigated, albeit at different L/M ratios (Fig. 3.7). At a higher Z, envelope inflation starts at lower masses because of larger opacities that help approach $\Gamma \approx 1$. We reiterate that envelope inflation might already start to develop before reaching the Eddington limit because of the contribution from the gas pressure gradient (cf. Sec. 3.3). Envelope inflation is responsible for the redward bending of the ZAMS and the TAMS in the upper HR diagram (Fig. 3.3), that is also supported by observations (Castro et al. 2014). The extent of inflation might be used to infer the value of α_{MLT} for massive stars by comparing the main-sequence width of the models against the observational TAMS (Castro et al. 2014; Bestenlehner et al. 2014).

We find that the mass contained in the inflated envelopes can range from $\sim 10^{-6}\,\mathrm{M}_\odot$ in the hot, luminous models to $\sim 100\,\mathrm{M}_\odot$ in the cool supergiant type models, across the whole range of metallicities investigated. While the observational signatures of these envelopes needs to be explored further, the ones with high envelope masses ($M_{\mathrm{env}} > 1\,\mathrm{M}_\odot$) seem to be promising candidates for explaining the violent LBV eruptions, for e.g., the 1860 outburst η Car, and other η Car analogs (Khan et al. 2015) or supernova imposters. These models are near the Eddington limit, have several solar masses in the loosely bound envelope and can potentially match the energy output of $10^{49} - 10^{50}$ erg seen in an LBV outburst. The details of the instability responsible for the outburst still needs to be investigated in detail. On the other hand, if the inflated envelopes are lost episodically from the models with small envelope masses, $10^{-3}\,\mathrm{M}_\odot$ or lower, it will cause them to shrink to the non-inflated core radius but will not be able to change the bolometric luminosity appreciably. These models have been put forward to explain the S-Doradus type variations by Gräfener et al. (2012).

Moriya et al. (2015) proposed that an observational consequence of a supernova progenitor with an inflated envelope is that it extends the rise time of the supernova shock-breakout signal. This naturally explains the long (~ 50 s) shock breakout X-ray signal detected from the Type Ic SN 2008D (Soderberg et al. 2008) that is believed to have had a compact WR progenitor.

Luminous helium stars also show pronounced core-halo structures and such models have been investigated in the past (Ishii et al. 1999; Petrovic et al. 2006; Gräfener et al. 2012; Tramper et al. 2015). The apparent mismatch in radii between model atmosphere calculations and stellar interior models of massive Galactic Wolf-Rayet stars has been claimed to have been reconciled by envelope inflation (Gräfener et al. 2012).

The inflated models are potentially unstable against the so-called strange-mode instability (Gautschy & Glatzel 1990; Glatzel & Kiriakidis 1993a) because of low heat capacities in their dilute envelopes (Glatzel 1994). Glatzel & Kiriakidis (1993a) reported that their solar metallicity models with $\log(\mathscr{L}/\mathscr{L}_\odot) \gtrsim 4$ are unstable to strange-mode oscillations. This result coincides with the boundary between the inflated and non-inflated models in our Z_{MW} grid. Furthermore, these oscillations might drive mass-loss from the star (Grott et al. 2005). The pulsational properties of our models will be explored in detail in a forthcoming study.

A critical ingredient in the physics of envelope inflation is convection, i.e. how convective energy transport is treated in these regions. The MLT is probably not the best model of convection in the radiation-pressure dominated regions where convective velocities approach the sound speed (Canuto & Mazzitelli 1991; Sanyal et al. 2015). In the literature, stellar models computed with increased convective efficiency do not show signs of envelope inflation (Ekström et al. 2012; Yusof et al. 2013). Jiang et al. (2015) recently performed 3-D radiation hydrodynamics simulations of massive star envelopes and concluded that for a $80\,\mathrm{M}_\odot$ ZAMS model, standard MLT overestimates the convective flux in the inflated region around the Fe-bump. In that case inflation in our 1-D models has been largely underestimated, and it will be interesting to look at the quantitative differences. Jiang et al. (2015) also found turbulent velocities that exceed the isothermal sound speed, driving shocks in the envelope and creating an inhomogeneous, clumpy medium. They, however, do not see any phenomenon that can lead to the ejection of the envelope. We note that they only simulated a small patch of the envelope around the Fe-bump, whereas we find the largest Eddington factors and the strongest inflation in our coolest models that contain the hydrogen recombination zone in their interior (Fig. 3.4).

Grassitelli et al. (2016b) recently investigated the role of turbulent pressure (P_{turb}) in stellar models computed with the metallicities Z_{MW} , Z_{LMC} and Z_{SMC} , and found that its effect on stellar structure is negligible regardless of the metallicity (Grassitelli et al. 2015b). However, the ratio of P_{turb} to P_{total} in the stellar envelope decreases for lower metallicities at a given temperature and luminosity. This trend is consistent with our results for inflation (Figs. 3.6 and 3.7). At higher metallicities the density in the inflated envelope is lower which implies inefficient convection and therefore a large and negative entropy gradient. Hence the convective velocities and the Mach number is also higher which leads to higher turbulent pressure.

Furthermore, Grassitelli et al. (2015b) found a correlation between macroturbulent velocities in Galactic OB stars and the fraction of turbulent pressure in the stellar envelope models. Since the turbulent pressure contribution in the inflated envelope becomes stronger in the upper HR diagram, high macroturbulent velocities ($\gtrsim 80\,\mathrm{km\,s^{-1}}$, Simón-Díaz 2015; Grassitelli et al. 2015b) might well be a signature of envelope inflation in hot, massive stars. The conditions in the inflated envelope might be inferred via asteroseismic studies (Aerts et al. 2014), especially if the connection between inefficient convection and high-order non-radial pulsations is confirmed (Aerts et al. 2009; Grassitelli et al. 2015a,b).

It might be interesting to look at the fate of the inflated envelopes in close binaries, since $\sim 70\%$ of all massive stars are believed to interact during their lifetimes (Sana et al. 2012). The loosely bound envelopes might help to stabilise mass-transfer in close massive binary systems, especially in metal-rich systems where this is expected to happen at lower masses. In close binaries, the hydrogen envelope is usually lost from the mass donor that bares its helium core and increases the L/M ratio. Helium stars with solar metallicity start to develop inflated envelopes from $\sim 10\,\mathrm{M}_\odot$ (see Fig. 19 in Köhler et al. (2015)). Many of the type Ib/c progenitors in binary systems are thus expected to have inflated envelopes (Woosley et al. 2010).

3.6 Supplementary material

3.6.1 Evolution of a $70\,\mathrm{M}_\odot$ inflated LMC model

We present the evolution of a typical inflated model, the $70\,\mathrm{M}_\odot$ Z_{LMC} sequence, with respect to its inflated envelope and the properties at the Fe-bump.

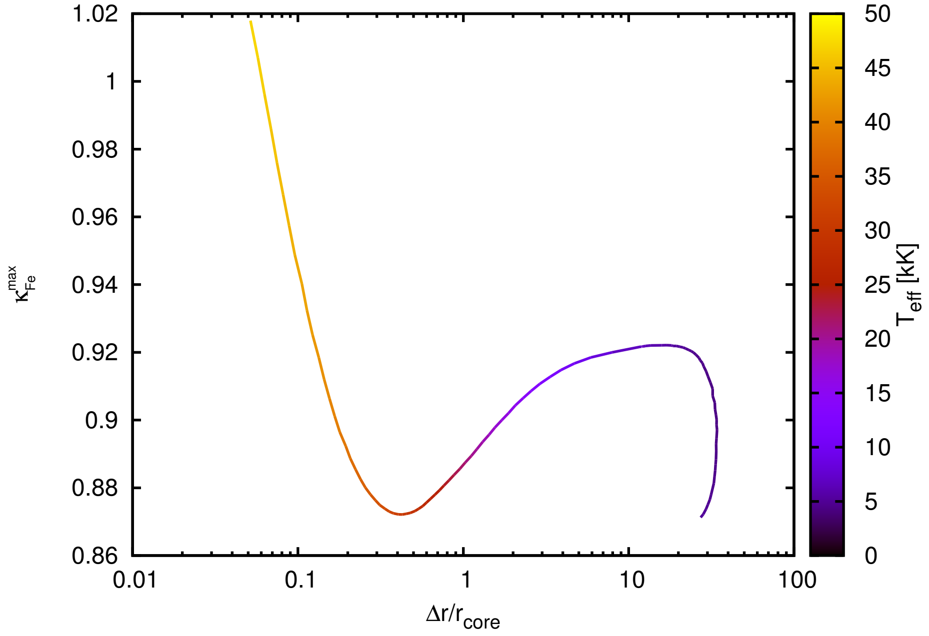

Figure 3.14: Maximum opacity in the temperature range $5 < \log(T/K) < 5.5$ with change in inflation.

The κ_{Fe}^{max} (Fig. 3.14) and the density at κ_{Fe}^{max} (Fig. 3.15) decrease initially as $\Delta r/r_{core}$ increases, because of an increase in L_{rad}/M (Fig. 3.16). The product of these two quantities, which is proportional to Γ, also increases initially up to $\Delta r/r_{core} \approx 0.1$ (Fig. 3.17) Thereafter it starts decreasing with a decrease in L_{rad}/M. The L_{rad}/M decreases in this phase of the evolution because of a rise in convective efficiency at this location, shown in Fig. 3.18. This is because as T_{eff} of the model keeps decreasing, the Fe-bump moves deeper inwards into the star where density is higher and hence convection is relatively efficient. When convection is capable of transporting the energy, L_{rad} need not be high such that $\Gamma = 1$. The inflated envelope keeps on increasing in size in spite of Γ_{Fe} coming down to values as low as 0.91.

At $\Delta r/r_{core} \gtrsim 20$, L_{rad}/M and Γ_{Fe} increase again while κ_{Fe}^{max} decreases. Since the star experiences high mass-loss rates at such low effective temperatures, its L/M ratio increases sharply in this phase (Fig. 3.19), but the convective efficiency does not increase as much. Hence to let the relatively high radiative flux to pass through, the model reduces its opacity which pushes up the value of Γ at that location. Note that at T_{eff} below ~ 8000 K the location of Γ_{max} is in the hydrogen recombination zone and not within the Fe-bump.

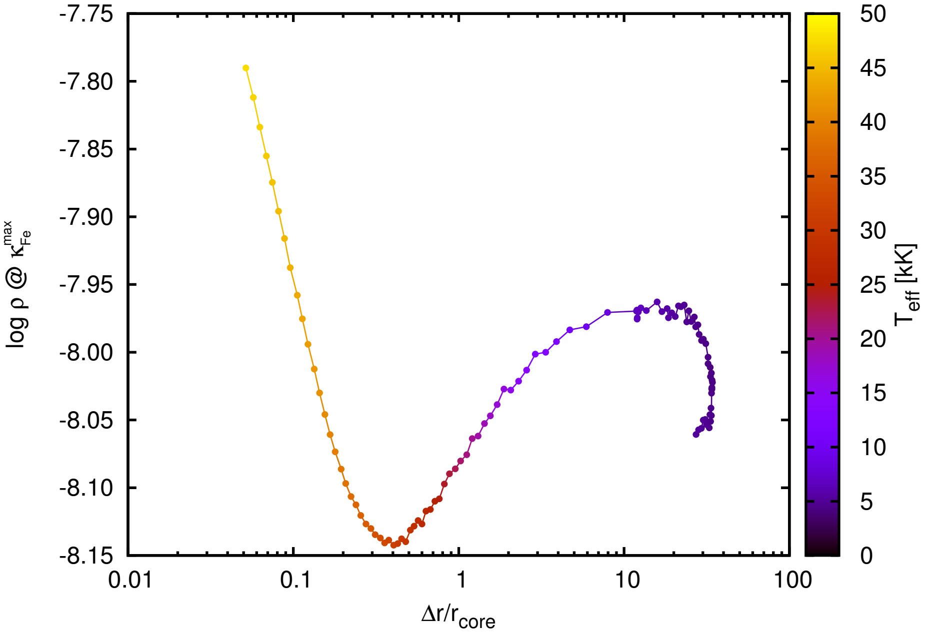

Figure 3.15: Density at the position of $\kappa_{\mathrm{Fe}}^{\max}$, with change in $\Delta r / r_{\mathrm{core}}$.

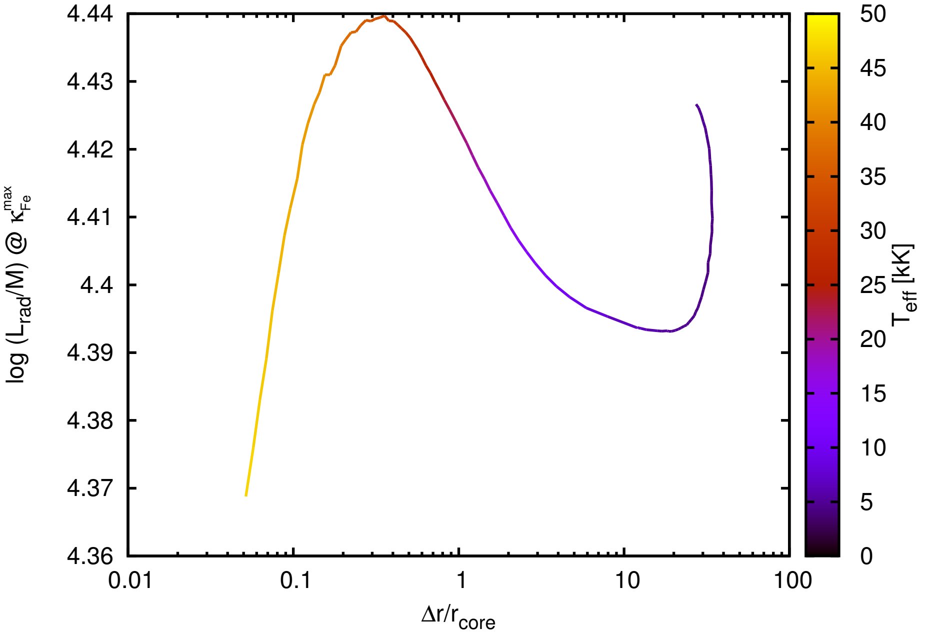

Figure 3.16: The L_{rad} / M ratio at the position of $\kappa_{\mathrm{Fe}}^{\max}$, with change in $\Delta r / r_{\mathrm{core}}$.

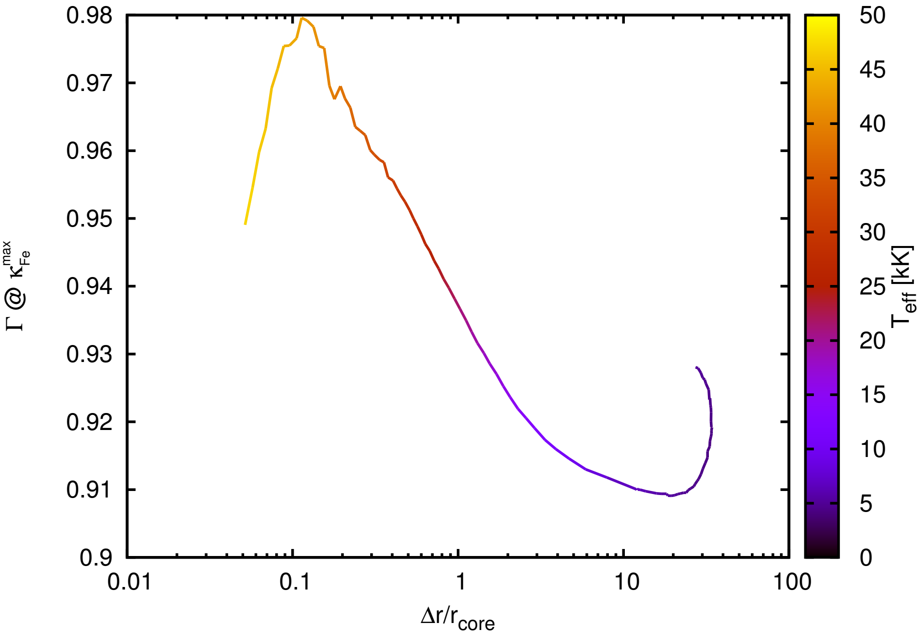

Figure 3.17: The Γ value at the position of $\kappa_{\rm Fe}^{\rm max}$, with change in $\Delta r/r_{\rm core}$.

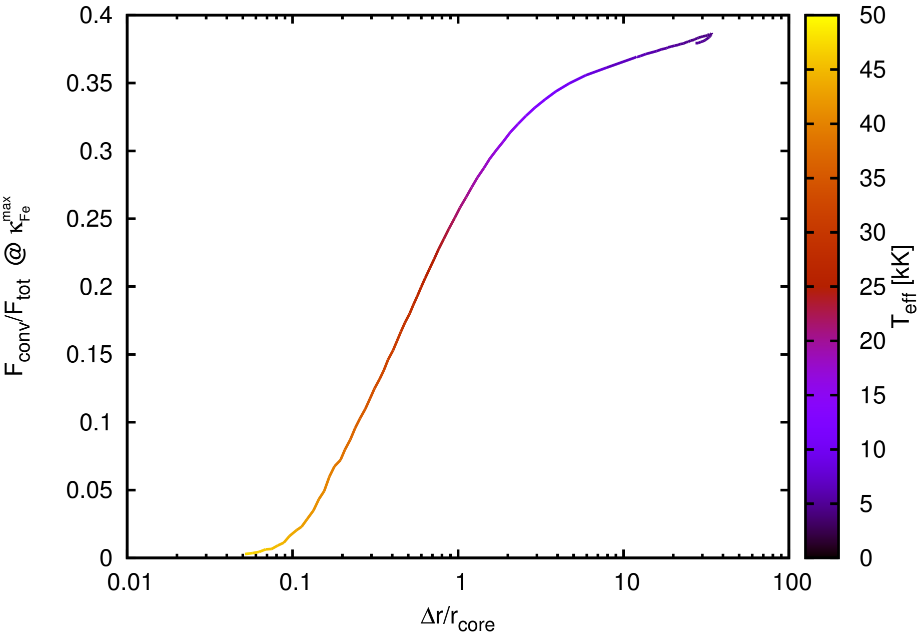

Figure 3.18: The ratio of convective flux to the total flux ,at the position of $\kappa_{\rm Fe}^{\rm max}$, with change in $\Delta r/r_{\rm core}$.

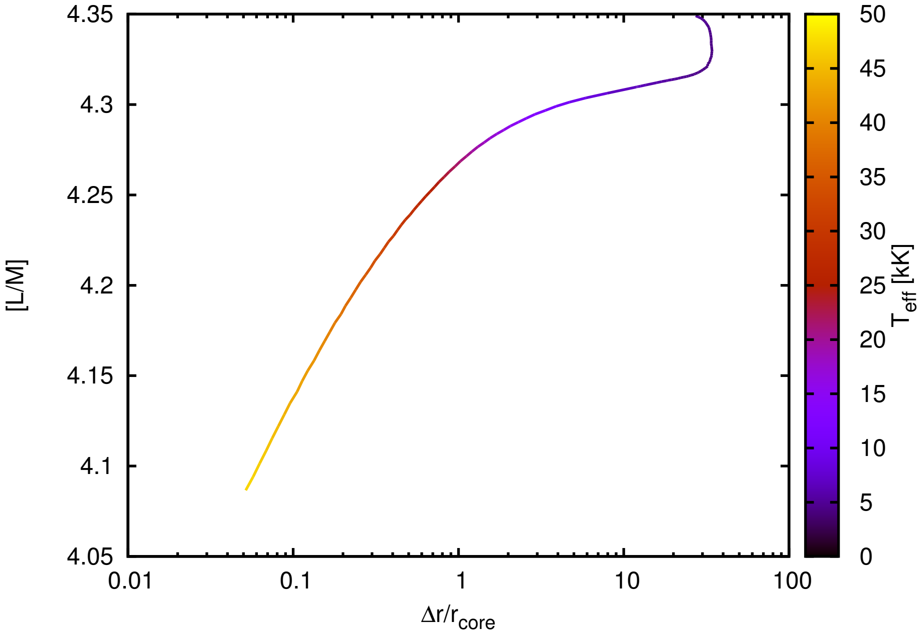

Figure 3.19: Change of $\mathscr{L}$ with $\Delta r/r_{\mathrm{core}}$.

CHAPTER 4

Extended supernova shock breakout signals from inflated stellar envelopes

T. J. Moriya, **D. Sanyal**, and N. Langer
Astronomy & Astrophysics, 2015, 575, L10

For this chapter, I computed all the stellar evolutionary models starting from the helium zero-age main-sequence up to at least carbon ignition in the core. I also contributed to the analysis and interpretation of the results and the preparation of the draft.

4.1 Introduction

The first electromagnetic signals from a supernova (SN) are emitted when the shock wave that travels through the stellar interior reaches the stellar surface (e.g., Colgate 1974; Klein & Chevalier 1978; Ensman & Burrows 1992; Matzner & McKee 1999; Tominaga et al. 2011; Tolstov et al. 2013). Photons trapped in the shock wave are suddenly released near the surface and start to be observed at this moment. This sudden release of photons in the shock wave near the stellar surface is called shock breakout.

The shock breakout signals are strongly affected by the properties of the SN progenitor and can be used to estimate them. Especially the duration of the shock breakout signals is assumed to approximately correspond to the light-crossing time t_{lc} of the progenitor, that is, $t_{\mathrm{lc}} \simeq R_\star/c$, where $R_\star$ is the progenitor radius and c is the speed of light. If a Wolf-Rayet (WR) star explodes, its shock breakout signal is expected to have a duration of about $1-10$ sec because typical radii of WR stars are on the order of $1-10\ \mathrm{R}_\odot$ (e.g., Crowther 2007; Woosley et al. 2010).

The shock breakout durations are, however, suggested to be extended for several reasons. For example, if the circumstellar medium (CSM) density is high enough to be optically thick, shock breakout durations can be extended as a result of photon diffusion in the dense CSM (e.g., Balberg & Loeb 2011; Svirski & Nakar 2014a,b). Aspherical photospheres may also cause an extension of the shock breakout durations (Suzuki & Shigeyama 2010; Couch et al. 2011). In addition, the duration of the shock breakout signals from Type Ib SN 2008D was observed to last for ~ 300 sec with a rise time of ~ 60 sec (Soderberg et al. 2008; Modjaz et al. 2009), indicating a progenitor radius of $R_\star \simeq t_{\mathrm{lc}}c \sim 130\ \mathrm{R}_\odot$. The indicated progenitor radius is too large to correspond to a WR star, but its SN spectral type and the early light curve modeling point to a WR progenitor with a radius smaller than $10\ \mathrm{R}_\odot$ (e.g., Chevalier & Fransson 2008; Rabinak & Waxman 2011, see also Dessart et al. 2011; Bersten et al. 2013). The observed long shock breakout duration may also indicate the existence of mechanisms to extend shock breakout signals.

In this Letter, we argue that shock breakout rise times can be extended significantly if SN progenitors have inflated envelopes. In that case, the shock breakout signals diffuse in the inflated envelope, resulting in the extension of the shock breakout rise times. The diffusion times t_{d} of canonical WR SN progenitors are shorter than the light-crossing time t_{lc} (Table 4.1). However, we show that the diffusion time can be much longer than the light-crossing time in inflated WR SN progenitors even if their radii are on the order of the solar radius.

We first explain the inflation of stellar envelopes and our inflated stellar evolution models in Sect. 4.2. We show the effect of the inflated envelopes on the SN shock breakout signals in Sect. 4.3. Our conclusions and their implications are summarized in Sect. 4.4.

4.2 Inflation of stellar envelopes

We first discuss the inflation of stellar envelopes. Inflation refers to the extended low-density envelopes in stellar models that reach Eddington luminosity in their outer layers (Ishii et al. 1999; Petrovic et al. 2006; Gräfener et al. 2012). The phenomenon was first discussed by Kato (1985, 1986) in the context of supermassive stars, considering electron-scattering as the only opacity source. The envelope inflation in the models discussed below is, however, caused by the Fe-group opacity bump at $T \sim 200$ kK (Ishii et al. 1999; Petrovic et al. 2006; Gräfener et al. 2012). When the stellar envelope approaches the Eddington luminosity, it will become convectively unstable (Langer 1997). The convective luminosity would need to carry any super-Eddington flux so that the radiative luminosity does not exceed the Eddington luminosity. However, if the envelope density is too low, convection cannot become efficient enough to transport sufficient energy inside the envelope. Then, the star expands its envelope in order to find a structure with a lower opacity so that the Eddington luminosity is not exceeded.

To discuss the actual structure of inflated envelopes in WR SN progenitors, we performed stellar evolution calculations by using an advanced one-dimensional hydrodynamic binary stellar evolution code (BEC; see Heger et al. 2000; Yoon et al. 2006; Woosley et al. 2010; Brott et al. 2011) to model WR stars as nonrotating hydrogen-free helium stars. The code solves the Lagrangian version of the equations for mass, energy, and momentum conservation together with convective and radiative energy transport and is explicitly coupled to a diffusive mixing scheme and a nucleosynthesis network (see Kozyreva et al. 2014 for details). BEC incorporates the latest input physics (Heger et al. 2000; Yoon et al. 2006; Woosley et al. 2010; Brott et al. 2011; Köhler et al. 2015) and is well-suited to investigate stars evolving close to the Eddington limit with inflated envelopes (Köhler et al. 2015; Sanyal et al. 2015).

In particular, the opacities used to compute the models were interpolated from the OPAL tables (Iglesias & Rogers 1996), which contain an opacity enhancement around $T \sim 200$ kK due to Fe-group elements. Convection was treated within the framework of the standard mixing-length theory (Böhm-Vitense 1958) with the mixing length set to 1.5 times the local pressure scale height. The WR mass-loss recipe proposed by Nugis & Lamers (2000) was used for our computations. The stellar surface was set at the photosphere where the optical depth is 2/3. We investigate the evolution of helium stars with initial masses of 10 and 12 $\mathrm{M}_\odot$ in this Letter. We explored two sets of models, one with solar metallicity and the other with half-solar metallicity. The half-solar metallicity models were computed until the oxygen-burning stage, while solar metallicity models were only computed until carbon ignition because we encountered numerical problems to iteratively converge models with large inflated envelopes that are larger at higher metallicity (Ishii et al. 1999). The inflation in these models at the time of the SN explosion could thus be somewhat stronger than we assume here. The evolutionary tracks of the models in the Hertzsprung-Russell (HR) diagram are presented in Fig. 4.1. The final stellar properties are summarized in Table 4.1.

The helium zero-age main-sequence models of both 10 and 12 $\mathrm{M}_\odot$ stars are marginally inflated. As a consequence of the applied mass loss, they lose mass and decrease in luminosity during the core helium-burning phase. After helium is exhausted in the core, the stars begin to contract and become hotter and brighter. The models are hardly inflated during this phase because the Fe-group opacity bump is only partially contained inside the stars. When the helium-shell ignites, the evolutionary tracks eventually move toward cooler temperatures because of the mirror principle (e.g., Kippenhahn et al. 2012). As the models become cooler, they become significantly inflated and exhibit a pronounced core-halo structure, as shown in Fig. 4.2. The electron-scattering Eddington factors of our models are shown in Table 4.1. When the full opacity is counted into the Eddington factor, all models reach the critical value of one. The envelope inflation is stronger for the solar metallicity models because the prominence of the Fe-group opacity bump increases with metallicity, as found in the studies by Ishii et al. (1999) and Petrovic et al. (2006). For comparison, we also show a polytropic star with $M_\star = 7\ \mathrm{M}_\odot$ and $R_\star = 2.4\ \mathrm{R}_\odot$ obtained with the polytropic index of 3 which does not have an inflated envelope. Figure 4.2 shows that our stellar models have extended low-density layers on top of the core structure. This type of the envelope inflation is also found in the previously reported models with similar final core masses (Yoon et al. 2012b). The evolution and final position of our stars in the HR diagram are consistent with their models.

4.3 Shock breakout in inflated stellar envelopes

The shock breakout in a SN occurs when photons start to leak from the shock wave, that is, when the dynamical timescale t_{dy} of the shock propagation in the remaining unshocked stellar envelope with radius ΔR ($t_{\mathrm{dy}} \simeq \Delta R/v_{\mathrm{sh}}$) becomes similar to the diffusion timescale $t_{\mathrm{d}} \simeq \tau\Delta R/c$, where v_{sh} is the shock velocity and τ is the optical depth in the remaining unshocked stellar envelope (e.g., Weaver 1976). The shock breakout condition can be simply expressed as $\tau \simeq c/v_{\mathrm{sh}}$. For a shock breakout at the stellar surface without the inflated envelope, ΔR is so small that t_{d} is smaller than the light-crossing time $t_{\mathrm{lc}} \simeq R_\star/c$, making the shock breakout duration $t_{\mathrm{lc}} \simeq R_\star/c$. For example, in the case of the 2.4 $\mathrm{R}_\odot$ polytropic star we show in Fig. 4.2, the light-crossing time is $t_{\mathrm{lc}} \simeq 5.60$ sec and the diffusion time is $t_{\mathrm{d}} \simeq 1.31$ sec, assuming $v_{\mathrm{sh}} = 10000\ \mathrm{km\ s^{-1}}$ (Table 4.1).

Table 4.1: Stellar properties and corresponding timescales.

Z ($Z_\odot$)	M_i ($M_\odot$)	$M_\star$ ($M_\odot$)	Γ_e	$\dot{M}$ (10^{-6} $M_\odot$ yr^{-1})	$\dot{M}/\dot{M}_\mathrm{max}$	$R_\star$ ($R_\odot$)	t_lc (sec)	ΔR^{30} ($R_\odot$)	t_d^{30} (sec)	ΔR^{20} ($R_\odot$)	t_d^{20} (sec)	ΔR^{10} ($R_\odot$)	t_d^{10} (sec)
1	10	6.8	0.412	8.1	0.45	2.43	5.67	1.73	121	1.01	47.0	0.130	3.01
1	12	7.8	0.439	7.6	0.57	2.31	5.38	1.71	119	1.70	78.6	0.372	8.62
0.5	10	7.4	0.398	6.4	0.066	1.06	2.47	0.189	13.2	0.188	8.72	0.163	3.78
0.5	12	8.6	0.428	8.3	0.11	1.33	3.10	0.356	24.9	0.351	16.27	0.306	7.09
-	-	$7^{(a)}$	-	-	-	2.4	5.60	0.0187	1.31	0.0170	0.788	0.0140	0.325

Notes. Initial metallicity, initial stellar mass, final stellar mass, final surface electron-scattering Eddington factor, final mass-loss rate, final ratio of the mass-loss rate to the critical mass-loss rate, final stellar radius, light-crossing time $t_\mathrm{lc} = R_\star/c$, distance from the radius at $\tau = 30$ to $R_\star$, diffusion time for $\tau = 30$ ($\upsilon_\mathrm{sh} = 10000$ km s^{-1}), distance from the radius at $\tau = 20$ to $R_\star$, diffusion time for $\tau = 20$ ($\upsilon_\mathrm{sh} = 15000$ km s^{-1}), distance from the radius at $\tau = 10$ to $R_\star$, and diffusion time for $\tau = 10$ ($\upsilon_\mathrm{sh} = 30000$ km s^{-1}). $^{(a)}$ Polytropic star with a polytropic index of 3.

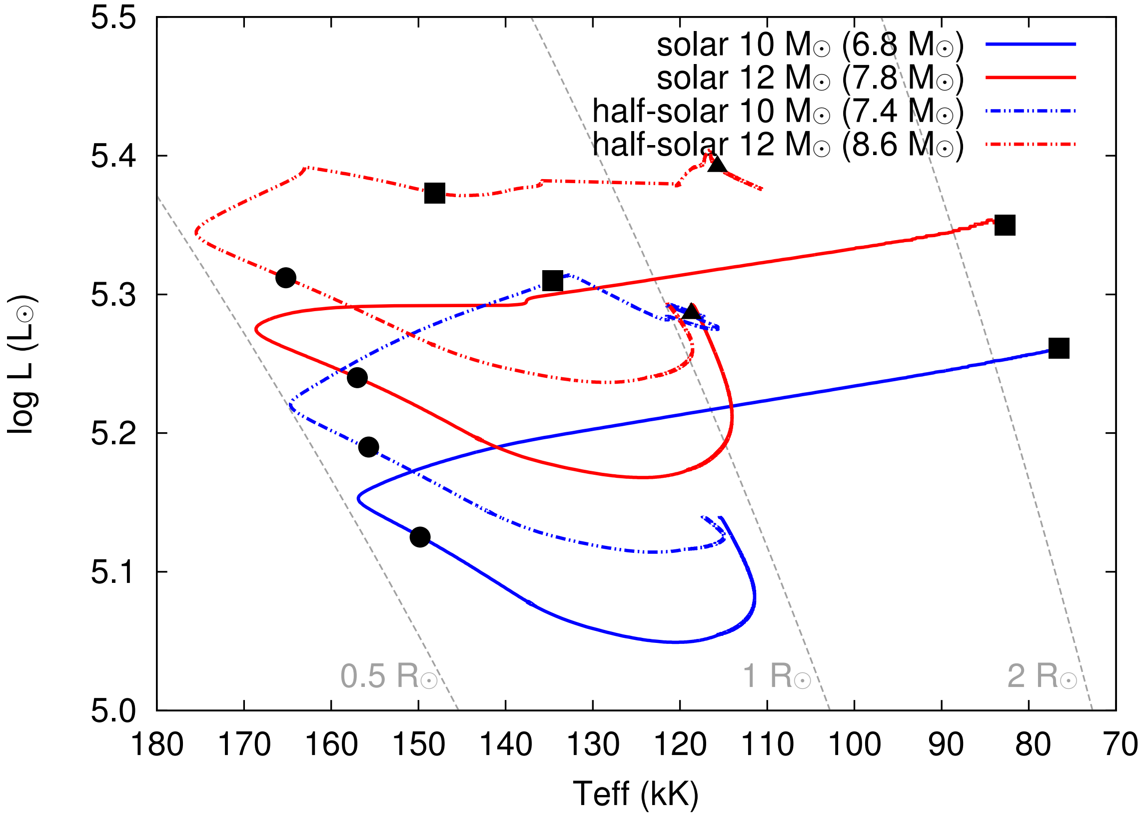

Figure 4.1: Evolutionary tracks of the helium star models in the HR diagram. The initial metallicity, initial mass, and final mass of the models are shown. The locations of helium-shell ignition (circles), core carbon ignition (squares), and core oxygen ignition (triangles) are marked. Lines of the constant radii of 0.5, 1, and 2 $R_\odot$ are also shown.

The inflated stellar models are characterized by extended low-density envelopes (Fig. 4.2). As a result, ΔR can be much larger than the corresponding values for the uninflated stellar models. In Fig. 4.3, we show the optical depth in our stellar models. In Table 4.1, we summarize the light-crossing time $t_{\rm lc}$ and the diffusion time $t_{\rm d}$ for several shock velocities. In the uninflated polytropic model, the shock breakout occurs at the edge of the stellar surface ($\Delta R = 0.0187\ R_\odot$ for $\tau = 30$), making the diffusion time shorter than the light-crossing time. If the progenitor has an inflated envelope, however, the shock breakout can occur at the bottom of the inflated envelope, keeping ΔR large when the shock breakout occurs. For example, our solar-metallicity $10\,M_\odot$ model has $\Delta R = 1.73\ R_\odot$ for $\tau = 30$ because of the envelope inflation. The large ΔR makes the diffusion time ($t_{\rm d} \simeq 121$ sec) much longer than the light-crossing time ($t_{\rm lc} \simeq 5.67$ sec). Thus, the timescale of the shock breakout signals within the inflated envelopes can be dominated by the diffusion time, and their rise time is determined by the diffusion time. The subsequent light curve is expected to decline exponentially with an e-folding timescale of the diffusion time due to the photon diffusion in the shocked envelope. Overall, the total shock breakout duration becomes significantly longer than the light-crossing time. The dynamical timescales of our inflated envelopes at the time of their explosions are $\sim$ 2000 sec, and the inflated envelopes can

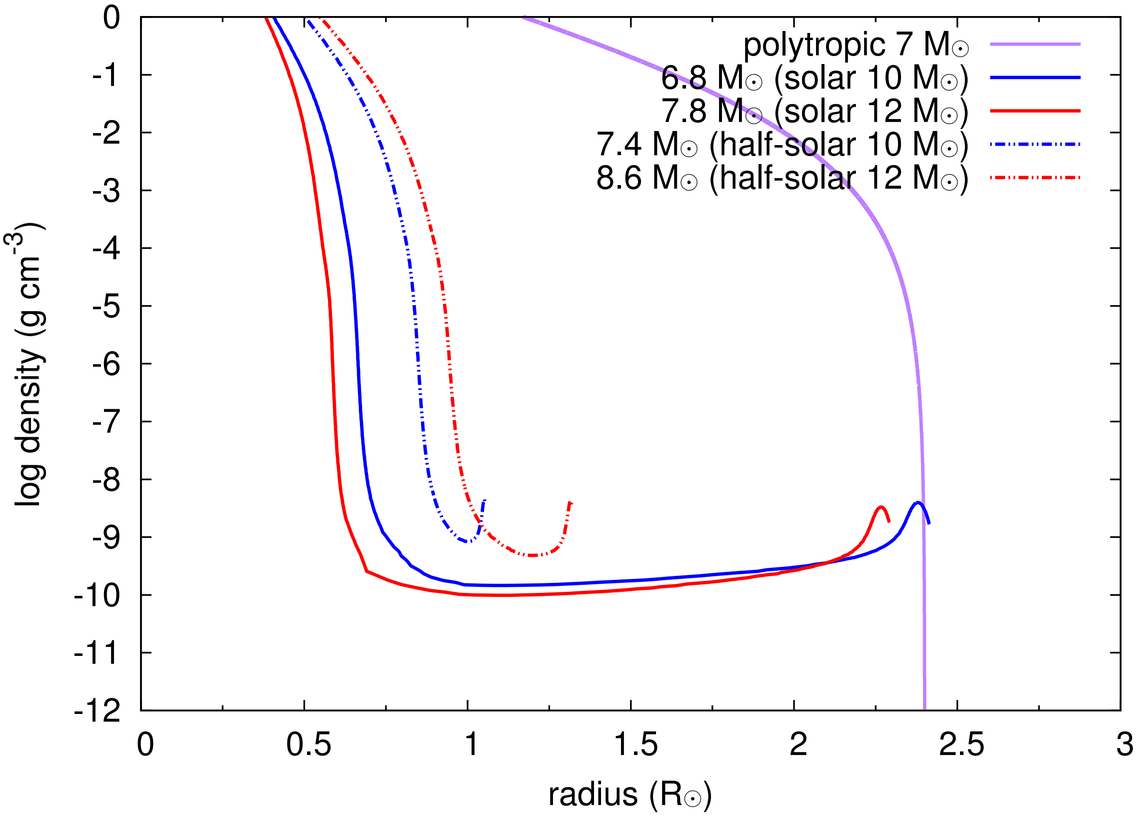

Figure 4.2: Final density structure of our stellar models. We also show the structure of a star without the envelope inflation, which is a polytiropic star of 7 $M_\odot$ and 2.4 $R_\odot$ with the polytropic index of 3. The inflated stellar models have the extended low-density regions on top of the core structure.

be sustained until the shock passes through.

We have computed the diffusion times for several shock velocities between 10000 and 30000 km s^{-1}. If the shock velocity at the shock breakout is too high, the diffusion time becomes shorter than the light-crossing time. In our models, the diffusion time starts to be shorter than the light-crossing time when the shock velocity is higher than ∼ 30000 km s^{-1} (Table 4.1). The shock velocity is suggested to reach above 30000 km s^{-1} at the shock breakout in WR stars (e.g., Nakar & Sari 2010). However, previous studies assume that WR stars only have a steeply declining envelope as in our polytropic model. A flat inflated envelope exists on top of the steeply declining core in the density structure of our models. The flat density structure decelerates the shock significantly, and the shock velocity at the shock breakout in inflated envelopes can be lower than 30000 km s^{-1}. Because the shock propagation in inflated stellar structure has not yet been investigated, hydrodynamical modeling in inflated envelopes is required to estimate the shock velocity at breakout in this case.

The sizes of the inflated envelopes in the half-solar-metallicity models are smaller than those in the solar-metallicity models because the Fe-group opacity bump is weaker with decreasing metallicity. However, the diffusion time can still be longer than the light-crossing time, and the shock breakout rise times can be longer than 10 sec in these WR stars.

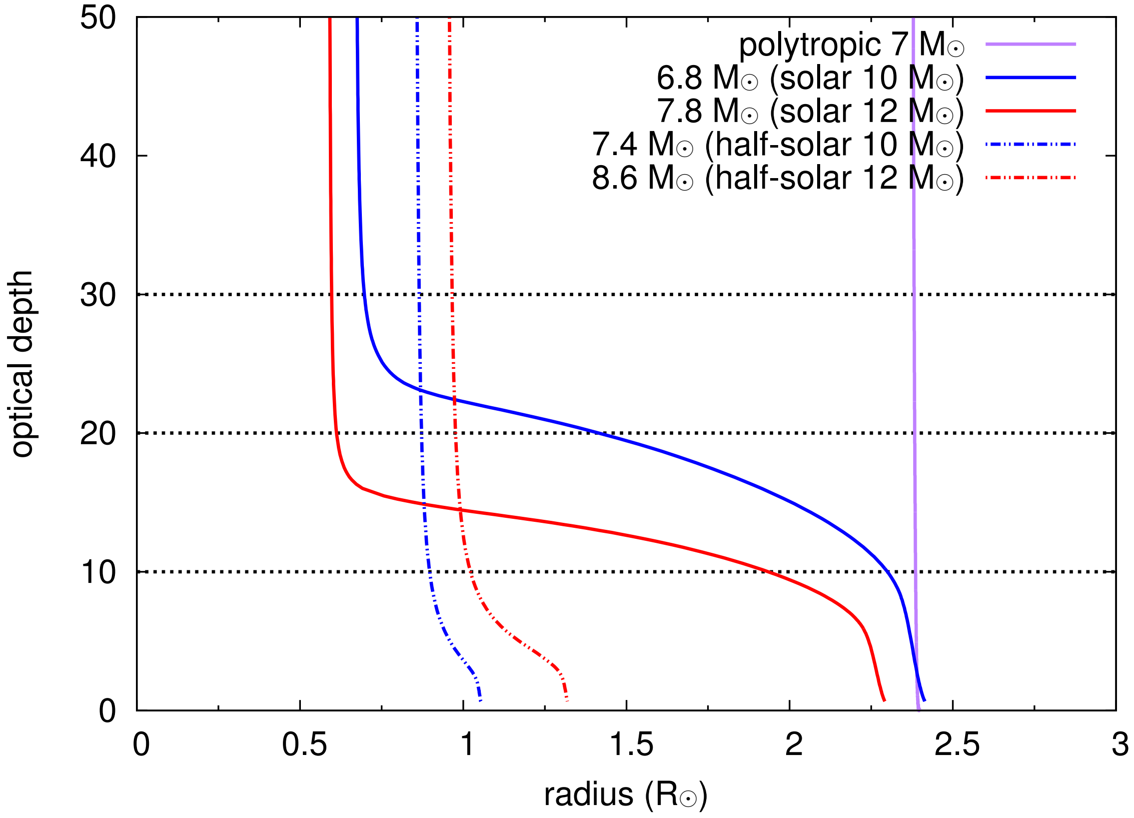

Figure 4.3: Optical depth τ in our models. The optical depth in the polytropic star is obtained with the constant opacity of 0.2 cm^2 g^{-1}.

Although higher metallicity models are preferred to have large ΔR and thus long t_d in terms of opacity, the inflated envelope can disappear because of higher mass-loss rates. Petrovic et al. (2006) showed that the inflated envelope disappears when the mass-loss rate of the star is higher than the critical mass-loss rate defined as

$$\dot{M}_\mathrm{max} \simeq 4\pi R_m^2 \rho_m \sqrt{\frac{GM_\star}{R_m}}, \tag{4.1}$$

where ρ_m is the lowest density in the inflated envelope and R_m is the radius at the lowest density (see also Gräfener et al. 2012). We show the ratio of the mass-loss rate in our models to the critical mass-loss rate in Table 4.1. Our solar-metallicity models are close to the critical mass-loss rates. Higher-metallicity stars are likely to exceed the critical mass-loss rate.

Although we have focused on WR SN progenitors in this Letter, stars do not need to be WR stars to have inflated envelopes. When stars are near the Eddington luminosity, they can have inflated envelopes even if they are hydrogen-rich. For example, luminous blue variables are hydrogen-rich stars that are close to the Eddington luminosity, and they have recently been suggested to be SN progenitors (e.g., Gal-Yam et al. 2009). They can also have inflated envelopes when they explode.

To confirm that some SN progenitors are actually inflated stars, observational consequences of the inflated envelopes in SN observational properties other than the shock breakout rise times are required to be investigated. Because the inflated envelopes in our models only have $\sim 10^{-8}$ $\mathrm{M}_\odot$, they are not likely to strongly affect later SN observables such as its light curve. However, the shock breakout spectra or very early SN spectra such as that recently obtained by Gal-Yam et al. (2014) may be affected by an inflated envelope. It is especially important to distinguish the shock breakout extension caused by an inflated envelope from that produced by a dense stellar wind because the shock breakout signals can be extended by the photon diffusion in both cases. Estimates of the progenitor mass-loss rate, for instance from multiwavelength SN observations, may constrain the wind density near the stellar photosphere and thereby confirm or rule out a shock break-out extension caused by winds (see Sect. 4.3.1 for the case of SN 2008D). Maeda (2013) also discusses possible observational consequences of the inflated envelopes.

4.3.1 SN 2008D

The extension of shock breakout signals by an inflated envelope may explain the long duration of the shock breakout signal observed in SN 2008D. Even if the progenitor of SN 2008D is a WR star with $R_\star \sim \mathrm{R}_\odot$, our result show that the rise time of the shock breakout signals can be ~ 60 sec because of the long diffusion time in the inflated envelope below which the shock breakout occurs. The shock-breakout luminosity decline after the luminosity peak is found to be similar to an exponential decay for a while (Soderberg et al. 2008), which is consistent with the diffusion interpretation.

The observed high temperature of the shock breakout signals in SN 2008D ($\sim 0.1-1$ keV, e.g., Modjaz et al. 2009; Li 2008) is suggested to indicate the shock velocity above ~ 20000 km s^{-1} (e.g., Katz et al. 2010; Balberg & Loeb 2011). The longest diffusion time for $v_\mathrm{sh} = 20000$ km s^{-1} among our models is 19 sec from the solar 12 $\mathrm{M}_\odot$ model. Although it is shorter than observed, ~ 60 sec, the diffusion time is still much longer than the light-crossing time. The observed e-folding timescale in the declining phase (~ 130 sec, Soderberg et al. 2008) is also longer than the diffusion time in our models, but our models do predict the overall extension of the shock breakout signals. The shock temperature becomes ~ 0.1 keV using $v_\mathrm{sh} = 20000$ km s^{-1} and our inflated envelope density (Katz et al. 2010), which corresponds to the observational constraints (e.g., Modjaz et al. 2009) and can explain the observed thermal X-ray luminosities ($\sim 10^{43}$ erg s^{-1}) with a radius of $\sim \mathrm{R}_\odot$. More investigations are required to see whether the X-ray spectra can be explained by our model.

The later shock velocity is observed to be $0.25c$ (Soderberg et al. 2008). However, the shock can have accelerated after the shock breakout because of the steep density decline between the stellar surface and the low density wind (cf., Tolstov et al. 2013). Thus, the observed velocity may not correspond to the actual shock velocity at the shock breakout.

The estimated SN ejecta mass of SN 2008D is $3-7$ $\mathrm{M}_\odot$ (Soderberg et al. 2008; Mazzali et al. 2008; Tanaka et al. 2009; Bersten et al. 2013). Our pre-SN stellar models (Table 4.1) have $6.3-7.8$ $\mathrm{M}_\odot$. Subtracting a remnant mass of about 1.4 $\mathrm{M}_\odot$, the expected ejecta masses from our inflated stellar models are consistent with those of SN 2008D. The mass-loss rates of our models are also consistent with that estimated from radio observations (7×10^{-6} $\mathrm{M}_\odot$ yr^{-1}, Soderberg et al. 2008).

The metallicity at the location where SN 2008D appeared is estimated to be 0.5 $Z_\odot$ based on the metallicity gradient in the host galaxy (Soderberg et al. 2008). Our 0.5 $Z_\odot$ stars do not inflate enough to explain the long shock breakout rise time of ~ 60 sec. However, Galactic metallicity gradients have large dispersions (e.g., Pedicelli et al. 2009). Since our $Z_\odot$ stars have much longer diffusion times, it is possible that the progenitor metallicity of SN 2008D is around $Z_\odot$ or higher, and the progenitor had a sufficiently inflated envelope to show the long shock breakout rise time with the estimated shock velocity. Recent metallicity measurements at the location of SN 2008D support our arguments (Modjaz et al. 2011; Thöne et al. 2009).

4.4 Conclusions

We have shown that the rise times of supernova shock breakout signals can be extended because of inflated stellar envelopes. The shock breakout can occur within the low-density inflated envelopes in which the shock breakout signals are diffused and extended. The long diffusion time in the inflated envelopes makes the shock breakout rise times long. The shock breakout timescale is then dominated by the diffusion time instead of by the light-crossing time. Even if a SN progenitor has a radius on the order of the solar radius whose light-crossing time is a few seconds, the rise time of the shock breakout signals can be more than 100 seconds because of the inflated envelope. The extension of the shock breakout signals by the inflated envelope may explain the mysterious long shock breakout rise time observed in Type Ib SN 2008D, although more investigations are required to confirm this.

The actual existence of inflated stellar envelopes is still widely debated. While we find the envelope inflation in our stellar evolution models, the envelope inflation is not as prominent in other models (e.g., Ekström et al. 2012). If inflated envelopes exist, they are also pulsationally unstable (e.g., Glatzel et al. 1993) with unknown consequences. If we can confirm that SN shock breakout signals from WR SN progenitors have signatures of inflated envelopes, for example, extended shock breakout signals from SN progenitors with low mass-loss rates, it may indicate the common existence of inflated stellar envelopes in nature. The shock breakout signals can be a viable probe of unsolved problems in stellar structure as well as a touchstone of the stellar evolution theory, which predicts the final status of the massive stars.

CHAPTER 5

Outlook

“We are all in the gutter, but some of us are looking at the stars."
- Oscar Wilde, in *Lady Windermere’s Fan*

Massive stars are the major source of metals without which life on earth would not have been possible – this fact alone makes them interesting objects to study. Our understanding of stellar evolution, especially in the field of massive stars has made rapid strides over the last couple of decades, boosted by significant improvements in high-resolution spectroscopy, spectropolarimetry, asteroseismology, transient searches and of course, numerical modelling.

Although the concept of the Eddington limit is old and quite simple in its original formulation, it is only recently that we have started to understand its detailed implications and explore its observational consequences in the context of massive stars. The key result of this thesis is that massive stars (above $\sim 30\,\mathrm{M}_{\odot}$ in our Galaxy) reach the Eddington limit in their interior and develop extended inflated envelopes that have far-reaching consequences for their structure and evolution. Though envelope inflation is predicted within the framework of the standard Mixing Length Theory, not all stellar evolution codes include this effect. For example, in the models of very massive stars by Yusof et al. (2013), envelope inflation is suppressed by allowing convection to be extremely efficient in the the outer layers of stars. Having mapped out the Eddington limit and envelope inflation in the upper H-R diagram over a wide range of metallicities, we must henceforth identify and predict their observational consequences that will help us constrain the models and further our understanding of the physics of very massive stars. Envelope inflation predicts a broadening of the terminal-age main-sequence (Chap. 2, cf. Castro et al. 2014) and an extension in the rise times of shock breakout signals from Type Ib/c supernovae (Moriya et al. 2015; Sanyal et al. 2015), both of which are supported by observations. I discuss below a few key issues that needs to be addressed in the future and some of the challenges that lie ahead.

Comparison to multi-dimensional simulations: Envelope inflation is predicted for massive stars not only by the latest one-dimensional models, but also in the three-dimensional radiation hydrodynamic simulations that includes a better treatment of turbulent energy transport (Jiang et al. 2015). Although more such detailed studies are needed to explore the parameter space in the upper H-R diagram, it has already opened up possibilities for calibrating the efficiency of convective energy transport and the effect of density homogeneities (“clumps”) in the 1-D models.

Envelope instabilities: The connection between inefficient convection and envelope inflation has been pointed out several times in Chap. 2, 3. As convection becomes inefficient, the velocities of the convective blobs increase, and approach the local sound speed. Therefore, the turbulent pressure which is proportional to the Mach number, increases. These turbulent pressure fluctuations in hot luminous stars might excite high-order g-modes, which may explain the macroturbulent broadening in the spectra of stars found outside the classical instability domains (Grassitelli et al. 2015b). Therefore macroturbulent broadening as an observational signature of inflated envelopes might serve as a probe to determine the extent of inflation, thereby constraining the model of convective energy transport in the sub-surface layers of massive stars. Furthermore, the interaction between the sub-surface convective layers and the overlying radiative layers in the inflated envelopes of classical WR stars have been predicted to induce small-scale velocity fields at the surface that causes line-profile variability in their spectra (Grassitelli et al. 2016a).

The so-called strange-mode instability is predicted only for stars which show a pronounced core-halo density structure (Glatzel 1994). The strange modes are characterised by growth rates in the dynamical regime, i.e. much faster than the modes excited by the standard κ-mechanism or the ϵ-mechanism (Glatzel & Kiriakidis 1993a,b). However, non-linear stability analyses that predict amplitudes and brightness variations are scarce and outdated (Grott et al. 2005). Since the occurrence of strange-modes is dependent on envelope inflation, which in turn is connected to inefficient convective energy transport, a non-linear stability analysis of stellar models over a wide range of temperatures in the upper H-R diagram is required to facilitate a comparison with observations of strange-mode candidates (Aerts et al. 2010), thereby constraining the effect of envelope inflation in the models. There are open questions that needs to addressed, for example, whether these pulsations can drive a strong mass-loss from the star (cf. Moriya & Langer 2015), and what is the nature of coupling between convection and pulsations (cf. Sonoi & Shibahashi 2014).

Mass-loss: As we have mentioned already in the introductory chapter, wind mass-loss has a deterministic influence on the lives of massive stars starting from the main-sequence phase. Recent investigations of wind models of very massive stars have revealed that as the classical Eddington limit is approached, the mass-loss rates increase drastically (Gräfener et al. 2011; Vink et al. 2011; Bestenlehner et al. 2014). In other words, there is a ‘kink’ in the slope of the $\dot{M}$ versus Γ_e relation at the transition point between optically thin and optically thick winds, which roughly corresponds to $\Gamma_e \sim 0.7$. This feature will not only reduce the extent of redward evolution of massive very stars in the H-R diagram, but might also have severe consequences on their final fates, and therefore it is desirable that this mass-loss enhancement is included in stellar evolutionary models. Since envelope inflation results in a lowered surface temperature and a higher mass-loss rate, stellar models that include this effect will reach the critical Γ_e value (or the ‘kink’) earlier in their evolution. Furthermore, model atmosphere calculations for massive stars which include inflation might shed new light on the topic.

LBV eruptions: Although the exact mechanism of the instability responsible for the LBV Giant Eruptions has not been clearly identified yet, in this thesis we have shown that we are very close to arriving at a consistent model. In the region populated by LBVs in the H-R diagram, we find models that have a few Solar masses in their inflated envelopes such that these envelopes are very loosely bound to the non-inflated *core* of the star. A dynamical instability in the envelope therefore offers a possibility to eject several Solar masses of material in one go. This possibility will be explored in a forthcoming study.

Acknowledgements

As you might imagine, this thesis would not have been possible without the help of many amazing people that helped me during each stage of this journey. First and foremost, I would like to thank my supervisor Prof. Norbert Langer. His door was always open for any question that I might have had. When I started my PhD in stellar physics I had near-zero knowledge about stars, and today whatever I have learnt is almost exclusively because of him. I have also learnt from him the art of thinking and communicating clearly and effectively, which is something I find useful in all spheres of life. Thanks are also due to Thomas Tauris, who is one of the most amiable persons I have met, and also the second examiner of my thesis. When I first came to Bonn for an internship, I worked primarily with him on a project (about X-ray binaries) that kindled my interest in stars. Special thanks to Sutirtha for hosting me during my internship, otherwise I would have probably not ended up in Bonn for my doctoral study.

I would like to thank to all the past and present members of the stellar physics group, especially Luca, Fabian, Sutirtha, Dori, Alina, JC, Richard, Rob, Ilka, Sung-Chul, Götz, Oscar, Jonathan, Sasha, Pablo, Nicholás and Joachim, for all the memories we have shared, both inside and outside Aifa (over alcohol). I hope that we stay in touch!

I would also want to thank the members of the VLT-FLAMES Tarantula Survey consortium, especially Frank, Paco, Alex, Joachim, Jo, Chris and Götz, for the very useful annual meetings that I attended.

I am very thankful to the secretaries in the Argelander Institute - Elisabeth Kramer, Christina Stein-Schmitz and Sabine Derdau, for helping me out every time with the administrative queries that I had quite often.

I would also like to heartily thank Aritra Basu, Rimi Chatterjee, Nirupam Roy and Sutirtha Sengupta for the innumerable coffee breaks and the culinary adventures that we shared to discuss science, politics, and life in general.

Last but not the least I am thankful to my parents for encouraging me in my career choices from the very beginning. And Harita, who has been tolerating my idiosyncrasies and has been my support system for the last six years (and the beautiful years to come!).

List of publications

Refereed publications

1. **Sanyal, D.**, Langer, N. , Szécsi, D. & Yoon, S.-C & Grassitelli, L., *The metallicity dependance of envelope inflation in massive stars*, Accepted in A&A.
2. Grassitelli, L., Fossati, L., Langer, N., Simón-Diáz, S., Castro, N. & **Sanyal, D.**, *"On the metallicity dependence of turbulent pressure and macroturbulence in stellar envelopes*, 2016, Accepted in A&A.
3. Grassitelli, L., Chené, A.-N., **Sanyal, D.**, Langer, N., St-Louis, N., Bestenlehner, J. M. & Fossati, L., *Observational diagnostics of the unstable envelopes of Wolf-Rayet stars*, 2016, A&A, 590, A12.
4. Grassitelli, L., Fossati, L., Langer, N., Miglio, A., Istrate, A. G., & **Sanyal, D.**, *Relating turbulent pressure and macroturbulence across the HR diagram with a possible link to γ Dor stars*, 2015, A&A, 584, L2.
5. **Sanyal, D.**, Grassitelli, L., Langer, N. & Bestenlehner, J. M., *Massive main-sequence stars evolving at the Eddington limit*, 2015, A&A , 580, A20.
6. Tramper, F., Straal, S. M., **Sanyal D.**, Sana, H., de Koter, A., Gräfener, G., Langer, N., Vink, J. S., de Mink, S. E. & Kaper, L., *Massive stars on the verge of exploding: the properties of oxygen sequence Wolf-Rayet stars*, 2015, A&A, 581, A110.
7. Szécsi, Dorottya, Langer, Norbert, Yoon, Sung-Chul, **Sanyal, Debashis**, de Mink, Selma, Evans, Christopher J. & Dermine, Tyl, *Low-metallicity massive single stars with rotation. Evolutionary models applicable to I Zwicky 18*, 2015, A&A, 581, A15.
8. Grassitelli, L., Fossati, L.; Simón-Diáz, S., Langer, N., Castro, N. & **Sanyal, D.**, *Observational Consequences of Turbulent Pressure in the Envelopes of Massive Stars*, 2015, ApJ, 808, L31.
9. Moriya, T. J., **Sanyal D.** & Langer, N., *Extended supernova shock breakout signals from inflated stellar envelopes*, 2015, A&A, 575, L10.
10. Köhler, K., Langer, N., de Koter, A., de Mink, S. E., Crowther, P. A., Evans, C. J., Gräfener, G., Sana, H., **Sanyal D.**, Schneider, F. R. N. & Vink, J. S., *The evolution of rotating very massive stars with LMC composition*, 2015, A&A, 573, A71.

11. Tauris, T., **Sanyal, D.**, Yoon, S.-C & Langer, N., *Evolution towards and beyond accretion-induced collapse of massive white dwarfs and formation of millisecond pulsars*, 2013, A&A, 558, A39.

Non-refereed publications (first author)

1. **Sanyal, D.**, Moriya, T. J. & Langer, N. *Envelope inflation in Wolf-Rayet stars and extended supernova shock breakout signals*, to appear in the proceedings of the international Wolf-Rayet stars workshop held in Potsdam (2015), edited by W.-R. Hamann, A. Sander, and H. Todt.

Bibliography

Abbott, B. P., Abbott, R., Abbott, T. D., et al. 2016, Physical Review Letters, 116, 061102

Abel, T., Bryan, G., & Norman, M. 2002, Science, 295, 93

Aerts, C., Lefever, K., Baglin, A., et al. 2010, A&A, 513, L11

Aerts, C., Puls, J., Godart, M., & Dupret, M.-A. 2009, A&A, 508, 409

Aerts, C., Simón-Díaz, S., Groot, P., & Degroote, P. 2014, A&A, 569, A118

Alexander, D. & Ferguson, J. 1994, ApJ, 437, 879

Arnett, W., Meakin, C., Viallet, M., et al. 2015, ApJ, 809, 30

Asplund, M. 1998, A&A, 330, 641

Balberg, S. & Loeb, A. 2011, MNRAS, 414, 1715

Bersten, M., Tanaka, M., Tominaga, N., Benvenuto, O., & Nomoto, K. 2013, ApJ, 767, 143

Bestenlehner, J., Gräfener, G., Vink, J., et al. 2014, A&A, 570, A38

Böhm-Vitense, E. 1958, ZAp, 46, 108

Braun, H. 1997, PhD thesis, , Ludwig-Maximilians-Univ.~München, (1997)

Bresolin, F., Crowther, P., & Puls, J., eds. 2008, IAU Symposium, Vol. 250, Massive Stars as Cosmic Engines

Bromm, V. & Larson, R. 2004, ARA&A, 42, 79

Bromm, V., Yoshida, N., Hernquist, L., & McKee, C. 2009, Nature, 459, 49

Brott, I., de Mink, S., Cantiello, M., et al. 2011, A&A, 530, A115

Cantiello, M., Langer, N., Brott, I., et al. 2009, A&A, 499, 279

Canuto, V. & Mazzitelli, I. 1991, ApJ, 370, 295

Castro, N., Fossati, L., Langer, N., et al. 2014, A&A, 570, L13

Charbonnel, C., Meynet, G., Maeder, A., Schaller, G., & Schaerer, D. 1993, A&AS, 101, 415

Chevalier, R. & Fransson, C. 2008, ApJ, 683, L135

Chieffi, A. & Limongi, M. 2013, ApJ, 764, 21

Chiosi, C. & Maeder, A. 1986, ARA&A, 24, 329

Colgate, S. 1974, ApJ, 187, 333

Conti, P. 1975, Memoires of the Societe Royale des Sciences de Liege, 9, 193

Conti, P. 1984, in IAU Symposium, Vol. 105, Observational Tests of the Stellar Evolution Theory, ed. A. Maeder & A. Renzini, 233

Couch, S., Pooley, D., Wheeler, J., & Milosavljević, M. 2011, ApJ, 727, 104

Crowther, P., Schnurr, O., Hirschi, R., et al. 2010, MNRAS, 408, 731

Crowther, P. P. a. 2007, ARA&A, 45, 177

Davidson, K. 1987, ApJ, 317, 760

de Jager, C. 1984, A&A, 138, 246

de Koter, A., Lamers, H., & Schmutz, W. 1996, A&A, 306, 501

Dessart, L., Hillier, D., Livne, E., et al. 2011, MNRAS, 414, 2985

Doran, E., Crowther, P., de Koter, A., et al. 2013, A&A, 558, A134

Drew, J., Barlow, M., Unruh, Y., et al. 2004, MNRAS, 351, 206

Drissen, L., Moffat, A., Walborn, N., & Shara, M. 1995, AJ, 110, 2235

Eddington, A. 1926, The Internal Constitution of the Stars

Ekström, S., Georgy, C., Eggenberger, P., et al. 2012, A&A, 537, A146

El Eid, M. & Langer, N. 1986, A&A, 167, 274

Endal, A. & Sofia, S. 1976, ApJ, 210, 184

Ensman, L. & Burrows, A. 1992, ApJ, 393, 742

Érgma, É. 1971, Soviet~Ast., 15, 51

Evans, C., Taylor, W., Hénault-Brunet, V., et al. 2011, A&A, 530, A108

Figer, D. 2005, Nature, 434, 192

Fitzpatrick, E. & Garmany, C. 1990, ApJ, 363, 119

Friend, D. & Abbott, D. 1986, ApJ, 311, 701

Fuller, G., Woosley, S., & Weaver, T. 1986, ApJ, 307, 675

Gal-Yam, A., Arcavi, I., Ofek, E., et al. 2014, Nature, 509, 471

Gal-Yam, A., Mazzali, P., Ofek, E., et al. 2009, Nature, 462, 624

Gautschy, A. & Glatzel, W. 1990, MNRAS, 245, 597

Glatzel, W. 1994, MNRAS, 271, 66

Glatzel, W. & Kiriakidis, M. 1993a, MNRAS, 263, 375

Glatzel, W. & Kiriakidis, M. 1993b, MNRAS, 262, 85

Glatzel, W., Kiriakidis, M., Chernigovskij, S., & Fricke, K. J. 1999, MNRAS, 303, 116

Glatzel, W., Kiriakidis, M., & Fricke, K. 1993, MNRAS, 262, L7

Gräfener, G., Owocki, S. P., & Vink, J. S. 2012, A&A, 538, A40

Gräfener, G., Vink, J., de Koter, A., & Langer, N. 2011, A&A, 535, A56

Grassitelli, L., Chené, A.-N., Sanyal, D., et al. 2016a, A&A, 590, A12

Grassitelli, L., Fossati, L., Langer, N., et al. 2015a, A&A, 584, L2

Grassitelli, L., Fossati, L., Langer, N., et al. 2016b, accepted in A&A

Grassitelli, L., Fossati, L., Simón-Diáz, S., et al. 2015b, ApJ, 808, L31

Groh, J., Hillier, D., Damineli, A., et al. 2009, ApJ, 698, 1698

Groh, J., Meynet, G., & Ekström, S. 2013, A&A, 550, L7

Grott, M., Chernigovski, S., & Glatzel, W. 2005, MNRAS, 360, 1532

Hamann, W.-R., Koesterke, L., & Wessolowski, U. 1995, A&A, 299, 151

Heger, A., Fryer, C., Woosley, S., Langer, N., & Hartmann, D. 2003, ApJ, 591, 288

Heger, A. & Langer, N. 1996, A&A, 315, 421

Heger, A., Langer, N., & Woosley, S. 2000, ApJ, 528, 368

Heger, A. & Woosley, S. 2002, ApJ, 567, 532

Humphreys, R. & Davidson, K. 1979, ApJ, 232, 409

Humphreys, R. & Davidson, K. 1994, PASP, 106, 1025

Iglesias, C. & Rogers, F. 1996, ApJ, 464, 943

Iglesias, C., Rogers, F., & Wilson, B. 1992, ApJ, 397, 717

Ishii, M., Ueno, M., & Kato, M. 1999, PASJ, 51, 417

Jiang, Y.-F., Cantiello, M., Bildsten, L., Quataert, E., & Blaes, O. 2015, ApJ, 813, 74

Joss, P., Salpeter, E., & Ostriker, J. 1973, ApJ, 181, 429

Justham, S., Podsiadlowski, P., & Vink, J. 2014, ApJ, 796, 121

Kato, M. 1985, PASJ, 37, 311

Kato, M. 1986, Ap&SS, 119, 57

Katz, B., Budnik, R., & Waxman, E. 2010, ApJ, 716, 781

Kehrig, C., Vílchez, J., Pérez-Montero, E., et al. 2015, ApJ, 801, L28

Khan, R., Adams, S., Stanek, K., Kochanek, C., & Sonneborn, G. 2015, ApJ, 815, L18

Kippenhahn, R. & Thomas, H.-C. 1970, in IAU Colloq. 4: Stellar Rotation, ed. A. Slettebak, 20

Kippenhahn, R., Weigert, A., & Weiss, A. 1990, Stellar Structure and Evolution (Springer, Berlin)

Kippenhahn, R., Weigert, A., & Weiss, A. 2012, Stellar Structure and Evolution

Kiriakidis, M., El Eid, M., & Glatzel, W. 1992, MNRAS, 255, 1P

Kiriakidis, M., Fricke, K., & Glatzel, W. 1993, MNRAS, 264, 50

Klein, R. & Chevalier, R. 1978, ApJ, 223, L109

Köhler, K., Langer, N., de Koter, A., et al. 2015, A&A, 573, A71

Kotak, R. & Vink, J. 2006, A&A, 460, L5

Kozyreva, A., Yoon, S.-C., & Langer, N. 2014, A&A, 566, A146

Kroupa, P. 2001, MNRAS, 322, 231

Krtička, J. & Kubát, J. 2006, A&A, 446, 1039

Kudritzki, R., Pauldrach, A., Puls, J., & Abbott, D. 1989, A&A, 219, 205

Kudritzki, R.-P. & Puls, J. 2000, ARA&A, 38, 613

Kutter, G. 1970, ApJ, 160, 369

Lamers, H. & Fitzpatrick, E. 1988, ApJ, 324, 279

Lamers, H. J. G. L. M. 1997, in Astronomical Society of the Pacific Conference Series, Vol. 120, Luminous Blue Variables: Massive Stars in Transition, ed. A. Nota & H. Lamers, 76

Lamers, H. J. G. L. M., Bastiaanse, M. V., Aerts, C., & Spoon, H. W. W. 1998, A&A, 335, 605

Lamers, H. J. G. L. M. & Noordhoek, R. 1993, in Astronomical Society of the Pacific Conference Series, Vol. 35, Massive Stars: Their Lives in the Interstellar Medium, ed. J. P. Cassinelli & E. B. Churchwell, 517

Langer, N. 1991, A&A, 252, 669

Langer, N. 1997, in Astronomical Society of the Pacific Conference Series, Vol. 120, Luminous Blue Variables: Massive Stars in Transition, ed. A. Nota & H. Lamers, 83

Langer, N. 1998, A&A, 329, 551

Langer, N. 2012, ARA&A, 50, 107

Langer, N., Hamann, W.-R., Lennon, M., et al. 1994, A&A, 290, 819

Langer, N. & Kudritzki, R. 2014, A&A, 564, A52

Langer, N., Norman, C., de Koter, A., et al. 2007, A&A, 475, L19

Langer, N., Sanyal, D., Grassitelli, L., & Szésci, D. 2015, in Wolf-Rayet Stars: Proceedings of an International Workshop held in Potsdam, Germany, 1-5 June 2015. Edited by Wolf-Rainer Hamann, Andreas Sander, Helge Todt. Universitätsverlag Potsdam, 2015., p.241-244, ed. W.-R. Hamann, A. Sander, & H. Todt, 241–244

Larsson, J., Levan, A., Davies, M., & Fruchter, A. 2007, MNRAS, 376, 1285

Leitherer, C., Schmutz, W., Abbott, D., Hamann, W.-R., & Wessolowski, U. 1989, ApJ, 346, 919

Li, L.-X. 2008, MNRAS, 388, 603

Maeda, K. 2013, ApJ, 762, 14

Maeder, A. 1987, A&A, 178, 159

Maeder, A. 1989, in Astrophysics and Space Science Library, Vol. 157, IAU Colloq. 113: Physics of Luminous Blue Variables, ed. K. Davidson, A. Moffat, & H. Lamers, 15–23

Maeder, A. 1992, in Instabilities in Evolved Super- and Hypergiants, ed. C. de Jager & H. Nieuwenhuijzen, 138

Maeder, A. 2009, Physics, Formation and Evolution of Rotating Stars

Maeder, A. & Conti, P. 1994, ARA&A, 32, 227

Maeder, A., Georgy, C., Meynet, G., & Ekström, S. 2012, A&A, 539, A110

Maeder, A. & Meynet, G. 2000, A&A, 361, 159

Maeder, A. & Meynet, G. 2010, New A Rev., 54, 32

Magic, Z., Weiss, A., & Asplund, M. 2015, A&A, 573, A89

Marigo, P., Chiosi, C., & Kudritzki, R.-P. 2003, A&A, 399, 617

Massey, P., McNeill, R., Olsen, K., et al. 2007, AJ, 134, 2474

Matzner, C. & McKee, C. 1999, ApJ, 510, 379

Mazzali, P., Valenti, S., Della Valle, M., et al. 2008, Science, 321, 1185

McEvoy, C., Dufton, P., Evans, C., et al. 2015, A&A, 575, A70

Meynet, G. 1992, in Instabilities in Evolved Super- and Hypergiants, ed. C. de Jager & H. Nieuwenhuijzen, 173

Mihalas, D. 1969, ApJ, 156, L155

Modjaz, M., Kewley, L., Bloom, J., et al. 2011, ApJ, 731, L4

Modjaz, M., Li, W., Butler, N., et al. 2009, ApJ, 702, 226

Mokiem, M., de Koter, A., Vink, J., et al. 2007, A&A, 473, 603

Moriya, T. & Langer, N. 2015, A&A, 573, A18

Moriya, T. J., Sanyal, D., & Langer, N. 2015, A&A, 575, L10

Muijres, L., de Koter, A., Vink, J., et al. 2011, A&A, 526, A32

Nakar, E. & Sari, R. 2010, ApJ, 725, 904

Nieuwenhuijzen, H. & de Jager, C. 1990, A&A, 231, 134

Nomoto, K. 1984, ApJ, 277, 791

Nugis, T. & Lamers, H. 2000, A&A, 360, 227

Owocki, S., Gayley, K., & Shaviv, N. 2004, ApJ, 616, 525

Pamyatnykh, A. 1999, Acta Astron., 49, 119

Pastorello, A., Smartt, S., Mattila, S., et al. 2007, Nature, 447, 829

Paxton, B., Cantiello, M., Arras, P., et al. 2013, ArXiv e-prints, 208, 4

Pedicelli, S., Bono, G., Lemasle, B., et al. 2009, A&A, 504, 81

Petrovic, J., Langer, N., Yoon, S.-C., & Heger, A. 2005, A&A, 435, 247

Petrovic, J., Pols, O., & Langer, N. 2006, A&A, 450, 219

Poelarends, A., Herwig, F., Langer, N., & Heger, A. 2008, ApJ, 675, 614

Portegies Zwart, S. & van den Heuvel, E. 2016, MNRAS, 456, 3401

Quataert, E. & Shiode, J. 2012, MNRAS, 423, L92

Rabinak, I. & Waxman, E. 2011, ApJ, 728, 63

Rakavy, G., Shaviv, G., & Zinamon, Z. 1967, ApJ, 150, 131

Raskin, C., Scannapieco, E., Rhoads, J., & Della Valle, M. 2008, ApJ, 689, 358

Ruszkowski, M. & Begelman, M. 2003, ApJ, 586, 384

Sabín-Sanjulián, C., Simón-Díaz, S., Herrero, A., et al. 2014, A&A, 564, A39

Saio, H., Baker, N. H. N., & Gautschy, A. 1998, MNRAS, 294, 622

Sana, H., de Mink, S., de Koter, A., et al. 2012, Science, 337, 444

Sana, H., van Boeckel, T., Tramper, F., et al. 2013, MNRAS, 432, L26

Sander, A., Todt, H., Hainich, R., & Hamann, W.-R. 2014, A&A, 563, A89

Sanyal, D., Grassitelli, L., Langer, N., & Bestenlehner, J. 2015, A&A, 580, A20

Sanyal, D., Langer, N., Szécsi, D., Yoon, S.-C., & Grassitelli, L. 2016, A&A, to be submitted

Sanyal, D., Moriya, T. J., & Langer, N. 2015, in Wolf-Rayet Stars: Proceedings of an International Workshop held in Potsdam, Germany, 1-5 June 2015. Edited by Wolf-Rainer Hamann, Andreas Sander, Helge Todt. Universitätsverlag Potsdam, 2015., p.213-216, ed. W.-R. Hamann, A. Sander, & H. Todt, 213–216

Schaerer, D. 1996, A&A, 309, 129

Schaerer, D., Meynet, G., Maeder, A., & Schaller, G. 1993, A&AS, 98, 523

Schlegel, E. 1990, MNRAS, 244, 269

Schneider, F., Izzard, R., de Mink, S., et al. 2014, ApJ, 780, 117

Schnurr, O., Casoli, J., Chené, A.-N., Moffat, A., & St-Louis, N. 2008, MNRAS, 389, L38

Schnurr, O., Moffat, A., Villar-Sbaffi, A., St-Louis, N., & Morrell, N. 2009, MNRAS, 395, 823

Shaviv, N. 1998, ApJ, 494, L193

Shaviv, N. 2001, ApJ, 549, 1093

Simón-Díaz, S. 2015, in IAU Symposium, Vol. 307, New Windows on Massive Stars, ed. G. Meynet, C. Georgy, J. Groh, & P. Stee, 194–199

Smith, N. 2014, ARA&A, 52, 487

Smith, N. 2015, in Astrophysics and Space Science Library, Vol. 412, Very Massive Stars in the Local Universe, ed. J. Vink, 227

Smith, N. & Arnett, W. 2014, ApJ, 785, 82

Smith, N. & Tombleson, R. 2015, MNRAS, 447, 598

Smith, N., Vink, J. S. J., de Koter, A., & Koter, A. D. 2004, ApJ, 615, 475

Soderberg, A., Berger, E., Page, K., et al. 2008, Nature, 453, 469

Sonoi, T. & Shibahashi, H. 2014, PASJ, 66, 69

Spruit, H. 2002, A&A, 381, 923

Stothers, R. 2003, ApJ, 589, 960

Stothers, R. & Chin, C.-W. 1973, ApJ, 179, 555

Stothers, R. & Chin, C.-W. 1993, ApJ, 408, L85

Suijs, M., Langer, N., Poelarends, A.-J., et al. 2008, A&A, 481, L87

Sundqvist, J. & Owocki, S. 2013, MNRAS, 428, 1837

Suzuki, A. & Shigeyama, T. 2010, ApJ, 717, L154

Svirski, G. & Nakar, E. 2014a, ApJ, 788, L14

Svirski, G. & Nakar, E. 2014b, ApJ, 788, 113

Szécsi, D., Langer, N., Yoon, S.-C., et al. 2015, A&A, 581, A15

Tanaka, M., Tominaga, N., Nomoto, K., et al. 2009, ApJ, 692, 1131

Taylor, W., Evans, C., Sana, H., et al. 2011, A&A, 530, L10

Thöne, C. C., Michałowski, M. J., Leloudas, G., et al. 2009, ApJ, 698, 1307

Tolstov, A., Blinnikov, S., & Nadyozhin, D. 2013, MNRAS, 429, 3181

Tominaga, N., Morokuma, T., Blinnikov, S., et al. 2011, ApJS, 193, 20

Trampedach, R., Stein, R., Christensen-Dalsgaard, J., Nordlund, Å., & Asplund, M. 2014, MNRAS, 445, 4366

Tramper, F., Straal, S., Sanyal, D., et al. 2015, A&A, 581, A110

Ugliano, M., Janka, H.-T., Marek, A., & Arcones, A. 2012, ApJ, 757, 69

Ulmer, A. & Fitzpatrick, E. 1998, ApJ, 504, 200

van Marle, A., Owocki, S., & Shaviv, N. 2008, MNRAS, 389, 1353

Vink, J. & de Koter, A. 2005, A&A, 442, 587

Vink, J., de Koter, A., & Lamers, H. 2000, A&A, 362, 295

Vink, J. S., Muijres, L. E., Anthonisse, B., et al. 2011, A&A, 531, A132

Vink, J. S. J., Koter, A. D., Lamers, H. J. G. L. M., de Koter, A., & Lamers, H. J. G. L. M. 2001, A&A, 369, 574

Walborn, N. R. & Blades, J. C. 1997, ApJS, 112, 457

Weaver, T. 1976, ApJS, 32, 233

Wentzel, D. 1970, ApJ, 160, 373

Woosley, S. 1993, ApJ, 405, 273

Woosley, S., Heger, A., & Weaver, T. 2002, Reviews of Modern Physics, 74, 1015

Woosley, S. E., Blinnikov, S., & Heger, A. 2007, Nature, 450, 390

Woosley, S. E., Langer, N., Yoon, S.-C., Woosley, S. E., & Langer, N. 2010, ApJ, 725, 940

Yoon, S.-C., Dierks, A., & Langer, N. 2012a, A&A, 542, A113

Yoon, S.-C., Gräfener, G., Vink, J., Kozyreva, A., & Izzard, R. 2012b, A&A, 544, L11

Yoon, S.-C. & Langer, N. 2005, A&A, 443, 643

Yoon, S.-C., Langer, N., & Norman, C. 2006, A&A, 460, 199

Yorke, H. 1986, ARA&A, 24, 49

Yusof, N., Hirschi, R., Meynet, G., et al. 2013, MNRAS, 433, 1114

Zickgraf, F.-J., Wolf, B., Stahl, O., Leitherer, C., & Klare, G. 1985, A&A, 143, 421

Zinnecker, H. & Yorke, H. 2007, ARA&A, 45, 481